Master's thesis

NTNU
Norwegian University of Science and Technology
Faculty of Natural Sciences
Department of Materials Science and Engineering

Kjetil Houmb Kristiansen

Characterization of Extruded Aluminium Alloys from Ram Extrusion and Screw Extrusion

Master's thesis in Materials Technology
Supervisor: Hans Jørgen Roven
July 2020

NTNU
Norwegian University of
Science and Technology

Kjetil Houmb Kristiansen

Characterization of Extruded Aluminium Alloys from Ram Extrusion and Screw Extrusion

Master's thesis in Materials Technology
Supervisor: Hans Jørgen Roven
July 2020

Norwegian University of Science and Technology
Faculty of Natural Sciences
Department of Materials Science and Engineering

Preface

This master's thesis was written at NTNU, Department of Materials Science and Engineering, during the spring of 2020. The thesis is part of a research collaboration between NTNU and Hydro Aluminium.

I would like to thank my co-supervisor Adjunct Professors Oddvin Reiso for enabling ram extrusion experiments with SINTEF, and for theoretical guidance and valuable input on results. And Dr. Kristian Grøtta Skorpen for sharing in-depth insight and know-how of the screw extruder.

I would also like to thank Professor Hans Jørgen Roven for valuable discussions and fulfilling guidance.

Kjetil Houmb Kristiansen
NTNU, Trondheim
July 2020

Acknowledgements

I would like to thank the following people for assistance and advice during this study:

The engineering staff at the Department of Material Science and Engineering for making it possible to work safely in laboratories after the re-opening during the Covid-19 crisis.

Chief Engineer Pål Christian Skaret and Senior Engineer Marit Elinda Olaisen Odden for performing the many tensile test carried out for this thesis.

SINTEF Industry and Kai Zhang for performing the ram extrusion experiment.

PhD candidate Geir Langelandsvik and Co-supervisor Dr. Kristian Grøtta Skorpen for operating the screw extruder.

Abstract

In this thesis, the novel method of screw extrusion was compared to conventional ram extrusion for three 6xxx alloys. The effect of extrusion and post extrusion heat treatments were examined by optical microscopy and mechanical testing, i.e. hardness and tensile testing. Four different parallels from extrusion were examined, i.e. air cooled or water quenched profiles from both extrusion processes.

Mechanical properties and microstructures were summarized for each alloy, directly comparing the effects of the heat treatments on each cooling and extrusion method. The results from this study indicate that it is crucial to have stable extrusion temperature to ensure steady state extrusion, and thus ensuring uniform properties. It was shown that profiles from screw extrusion were less prone to recrystallization compared to ram extrusion, even after solution heat treatment. The effect of age hardening to T5 was seen to depend on quenching rate after extrusion. Heat treating to T6 after screw extrusion minimize the effects from extrusion, resulting in similar properties to ram extrusion.

Sammendrag

I denne oppgaven ble skruekstrudering sammenlignet med konvensjonell pressekstrudering for tre 6xxx legeringer. Effekten av ekstrudering og påfølgende varmebehandling ble undersøkt ved optisk mikroskopi, hardhetstesting og strekktesting. Fire forskjellige paralleller fra ekstrudering ble undersøkt, hvor profiler fra begge ekstruderingsmetodene ble luftkjølt eller vannkjølt.

Mekaniske egenskaper og mikrostrukturer ble oppsummert for direkte sammenligning av varmebehandlingenes effekt for hver avkjølings- og ekstruderingsmetode. Resultatene indikerer at det er avgjørende å ha stabil ekstruderingstemperatur for å sikre jevn ekstrudering, og dermed uniforme egenskaper gjennom profilen. Det ble vist at profiler fra skrueekstrudering var mer motstandsdyktig for rekrystallisering sammenlignet med pressekstrudering, selv etter innherding. Høy kjølehastighet etter ekstrudering så ut til å ha en god effekt på utherdingspotensialet til T5. Varmebehandling til T6 jevnet ut styrkebidraget fra ekstruderingsprosessene og ga lignende egenskaper.

Contents

Abbreviations

RT	Room temperature
SHT	Solution heat treatment, solution heat treated
SSSS	Super saturated solid solution
SE	Screw extrusion, screw extruded
RE	Ram extrusion, ram extruded
AC	Air cooled
WQ	Water quenched
ED	Extrusion direction
UTS	Ultimate tensile strength
YS	Yield strength

Chapter 1

Introduction

Alumiunium alloys in the 6xxx-series are the most extruded aluminium alloy series [1]. These aluminium extrusions offer complex cross sectional geometries in long lengths. Application areas for extruded aluminium include structural applications such as: the building industry, shipping and offshore industry, and the transportation sector for automotive and aerospace applications [2].

As of today the conventional extrusion methods for aluminium include direct and indirect hot extrusion. Screw extrusion of aluminium is a novel extrusion process patented by Norsk Hydro ASA in collaboration with NTNU [3]. This extrusion method involves continuous feeding and extrusion of granule feedstock, using less energy than industrial processes today. A study of the environmental impact have been assessed for screw extrusion and hot extrusion [4], amongst others.

Previous PhD and master theses have explored screw extrusion [5–10]. These theses have amongst others characterized material flow during screw extrusion, proposed a physical based empirical model for accumulated strain in screw extrusion and optimized electrical conductivity in screw extruded wires.

However, until now there has not been an extensive comparison of screw extrusion and ram extrusion. This thesis will compare these two extrusion processes for three 6xxx alloys. Differences in microstructures, mechanical properties and electrical conductivity will unfold and discussed.

Chapter 2

Theory

In this chapter, relevant literature will be reviewed in order to have a fundamental understanding of the processes involved in this work. Sections 2.4 and 2.5 are mostly adopted from the project work of the present author during autumn 2019 [11].

2.1 The AlMgSi system

The 6xxx alloy series designate heat treatable wrought alloys with main alloying elements of magnesium and silicon. Alloys in this series have good extrudability and intermediate strength. In this thesis, the alloys involved are 6060, 6005 and 6082.

The pseudo-binary Al$-$$Mg_2Si$ phase diagram in Figure 2.1a, shows the eutectic temperature at 595 °C, and with a maximum solid solubility limit for the equilibrium phase β-Mg_2Si of 1.85wt%. The solidus for a given solubility is given in the aluminium rich corner of the ternary Al-Mg-Si phase diagram is shown in Figure 2.1b. As the alloys used in this thesis have low alloying content, the solidus of equilibrium phase precipitates are of interest.

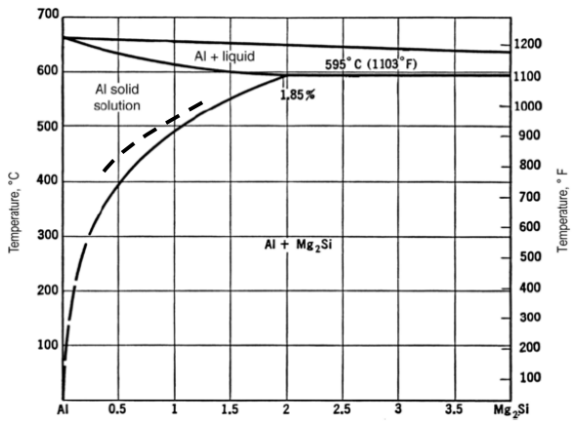

(a) Pseudo-binary Al-Mg_2Si phase diagram, from [12]. Dotted lines show the solvus for 6xxx alloys vs the classical solvus line for Al-Mg_2Si.

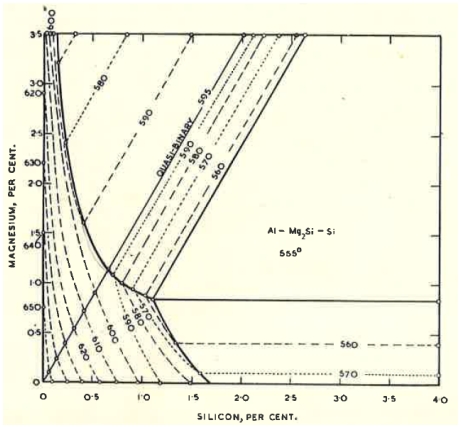

(b) Aluminium rich corner of ternary Al-Mg-Si phase diagram, showing the solidus in greater detail, from [13].

As seen from Figure 2.2 [2], these alloys have linearly increasing alloying element content with the same Mg/Si-ratio. The dominant strengthening mechanism in AlMgSi alloys is from precipitates obtained after heat treatments from super saturated solid solution (SSSS) [1]. The strength of these alloys are related to Mg and Si content and process conditions. During aging these solute atoms start clustering in the aluminium lattice, forming a high number density of needle shaped, coherent β'' precipitates and Guinier-Preston (GP) zones [14]. Mg and Si content resulting in the phase Mg_5Si_6 corresponds to the best combination of mechanical properties [15]. This Mg_5Si_6 corresponded to the composition of β'', found by Andersen et al.[16]. The general precipitation sequence of AlMgSi during aging is shown in Equation 2.1:

$$SSSS \rightarrow GPI \rightarrow \beta'' \rightarrow \beta' \rightarrow \beta Mg_2Si \tag{2.1}$$

Conditions which promote the formation of coarse equilibrium Mg_2Si particles, reduces the amount of precipitation hardening GP zones and β'' during aging. Therefore, controlling the precipitation of these Mg_2Si particles are crucial for obtaining maximum strength [17].

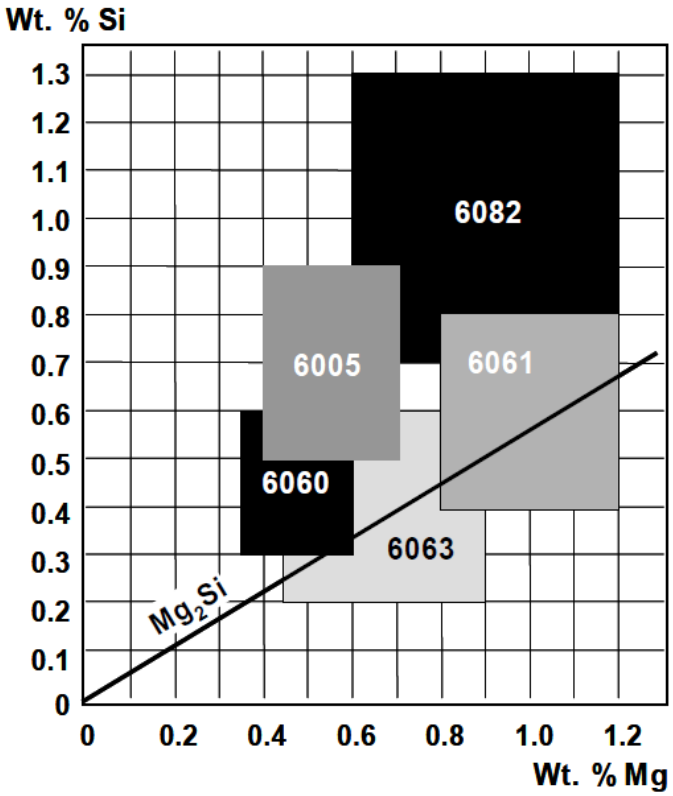

Figure 2.2: AlMgSi alloys as a function of Mg and Si content. Common AlMgSi alloys for extrusion purposes, from [2].

Typical minimum values for 6060, 6005 and 6082 as extruded rods are presented in Table 2.1. The strength for these alloys increases with Mg, Si content and as seen in Figure 2.2, these contain excess Si. Alloys with excess Si resulting in Mg:Si ratio of 5:6 promotes the formation of the strengthening β'' [18].

Table 2.1: Typical minimum property values for alloy EN AW-6060, EN AW-6005 and EN AW-6082 extruded rod [19, 20]. Alloy notation as presented in [19] . * HBW: Brinell hardness from wolfram carbide ball indenter. ** Properties from [20].

Alloy	Temper	Ultimate tensile strength, R_m MPa	Yield strength, $R_{p0.2}$ MPa	Elongation A_{50mm} %	Hardness HBW*
6060	T4	120	60	16	50
	T5	160	120	8	60
	T6	190	150	8	70
6005	T4	180	90	13	50
	T5**	305	270	12	90
	T6	270	225	8	90
6082	T4	205	110	12	70
	T5	270	230	6	90
	T6	340	315	14	95

2.2 Extrusion

Extrusion is a plastic deformation process by compression where a billet is forced to flow through a die of a smaller cross sectional area. It is widely used for manufacturing long profiles with complex cross sectional geometry. Aluminium extrusions are usually produced by hot extrusion, with billet temperatures ranging from 340 °C to 595 °C. These temperatures facilitate plastic deformation and are high enough to minimize strain hardening upon deformation [21].

2.2.1 Conventional ram extrusion

The most common method for aluminium extrusion, direct extrusion, utilizes a ram to force a billet through the die at the end of a container. In direct extrusion, the flow of metal follows the direction of the ram. The billet will slide relative to a zone of the outermost oxide layer sticking on the container surface (see Figure 2.3). Effectively causing shearing along the edge of the forward flowing aluminium. The force needed to push the billet forward will thus be influenced by the container-billet friction [21, 22].

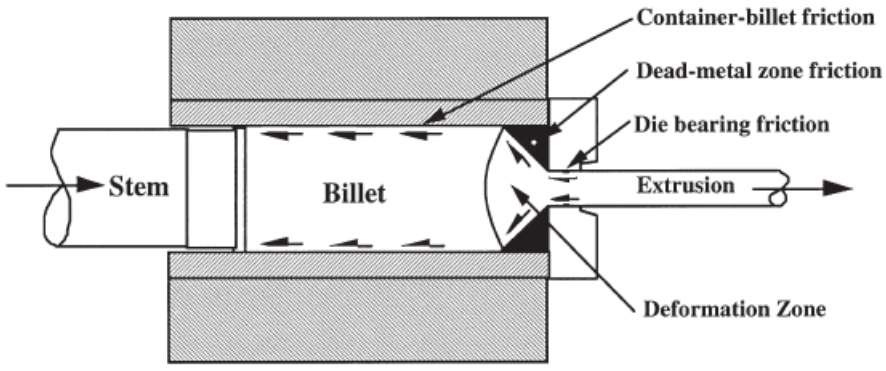

Figure 2.3: Friction components in direct extrusion. From [22].

The ram pressure approximately follows the curve in Figure 2.4 for a given ram displacement. Zone I: the billet is upset and the pressure sharply rises to maximum value accelerating the material to extrusion speed; Zone II: the pressure decreases and steady state extrusion continues. The container-billet friction decreases as the billet progresses through the container, reducing the needed ram pressure; Zone III: The minimum pressure value is reached, followed by a sharp rise during compaction of the butt [21, 22].

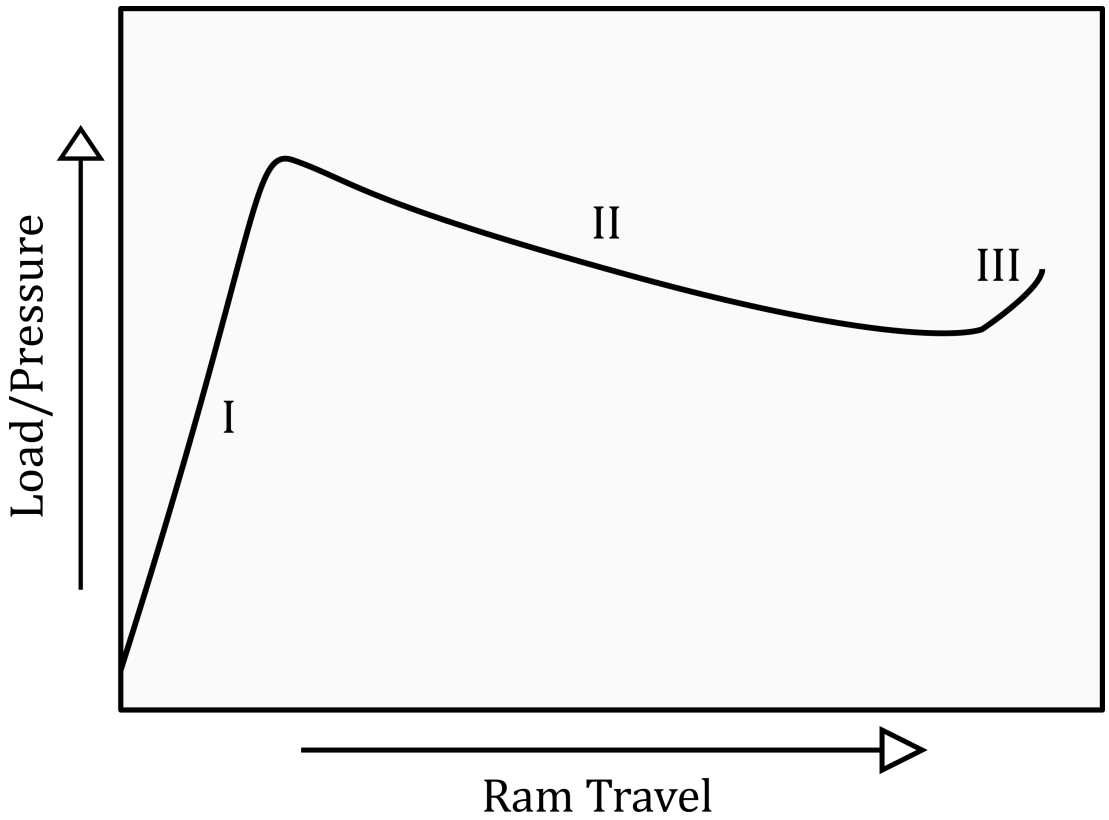

Figure 2.4: Load/pressure variations for direct extrusion along the ram travel. During I upsetting the billet, sharp rise in pressure; II steady state extrusion; III compaction of dead metal zone. Modified sketch from [22].

Extrusion speed

The relationship between the ram speed, V_R, and extrusion speed, V_E, for any extrusion die can be calculated following the reduction of cross sectional area. The extrusion V_E and ram speed V_R can be found from Equation 2.2 [21]:

$$V_E = V_R \frac{A_C}{A_E} = V_R R_e \tag{2.2}$$

, where the extrusion ratio, R_e, is defined by the cross section area of the container A_C, and A_E is the cross section area of the extrudate.

Strain contribution in conventional ram extrusion

To understand the properties in extruded aluminium, it is necessary to define the strain (deformation) as this affects the metal flow during extrusion. The effective

strain is defined by:

$$d\bar{\varepsilon} = \frac{dl}{l_0} \qquad \bar{\varepsilon} = \int_{l_0}^{l} \frac{dl}{l} = ln\frac{l}{l_0} \tag{2.3}$$

where l_0 is the initial billet length, and l is the final length. In ram extrusion, the strain is given by the extrusion ratio:

$$\bar{\varepsilon} = ln\frac{l}{l_0} = ln\frac{A_0}{A} = ln\frac{D_C}{D_E} \tag{2.4}$$

where A_0 is the initial billet cross sectional area, A is the final extrudate cross sectional area, D_C is the inner diameter of the container, and D_E is the final diameter of the extrudate. From this the effective strain for extrusion is defined as [22]:

$$\bar{\varepsilon} = 2ln\frac{D_C}{D_E} = 2ln\sqrt{R_e} \tag{2.5}$$

2.2.2 Screw extrusion

Screw extrusion of aluminium is a novel, solid state extrusion process developed by researchers from NTNU and Norsk Hydro ASA [3]. This continuous extrusion process utilizes an Archimedes screw to extrude profiles from granule feedstock in one step.

The screw extrusion process starts with feeding cleaned feedstock into the feeding inlet, positioned at the back of the screw extrusion module. Feedstock material is pushed forward through the screw housing and extrusion chamber, generating pressure, by the engine-driven screw. The highly viscous material produces pressure by friction as it sticks to the liner and screw surfaces [3].

The different stages of material flow through the screw extruder follows the six stages illustrated in Figure 2.5 [6]. These stages are explained below:

1. Sliding - in the first transport stage, fed aluminium granules slides forward relative to the container and screw surfaces.
2. Merging - the second transport stage continuously moves granules forward to interact with semi-consolidated aluminium.
3. Central channel flow - Granules are partially consolidated and pushed further in the screw channel. The mass is mainly flowing through the centre of the screw channel. From this point sticking friction prevails.
4. Forward flow - This region involves the screw flights smearing the fully consolidated aluminium layer by layer onto pre-existing aluminium, thus pushing it forward to the extrusion chamber.
5. Backflow - Same material flows backward to the screw channel, merging with the screw flow.

6. Extrusion - Layers are displaced forward by new layers deposited onto the "billet" in the extrusion chamber as it is forced through the extrusion die. Here, extrusion of aluminium occurs. Strain contributions at this stage is estimated as direct extrusion, i.e. using the extrusion ratio [8].

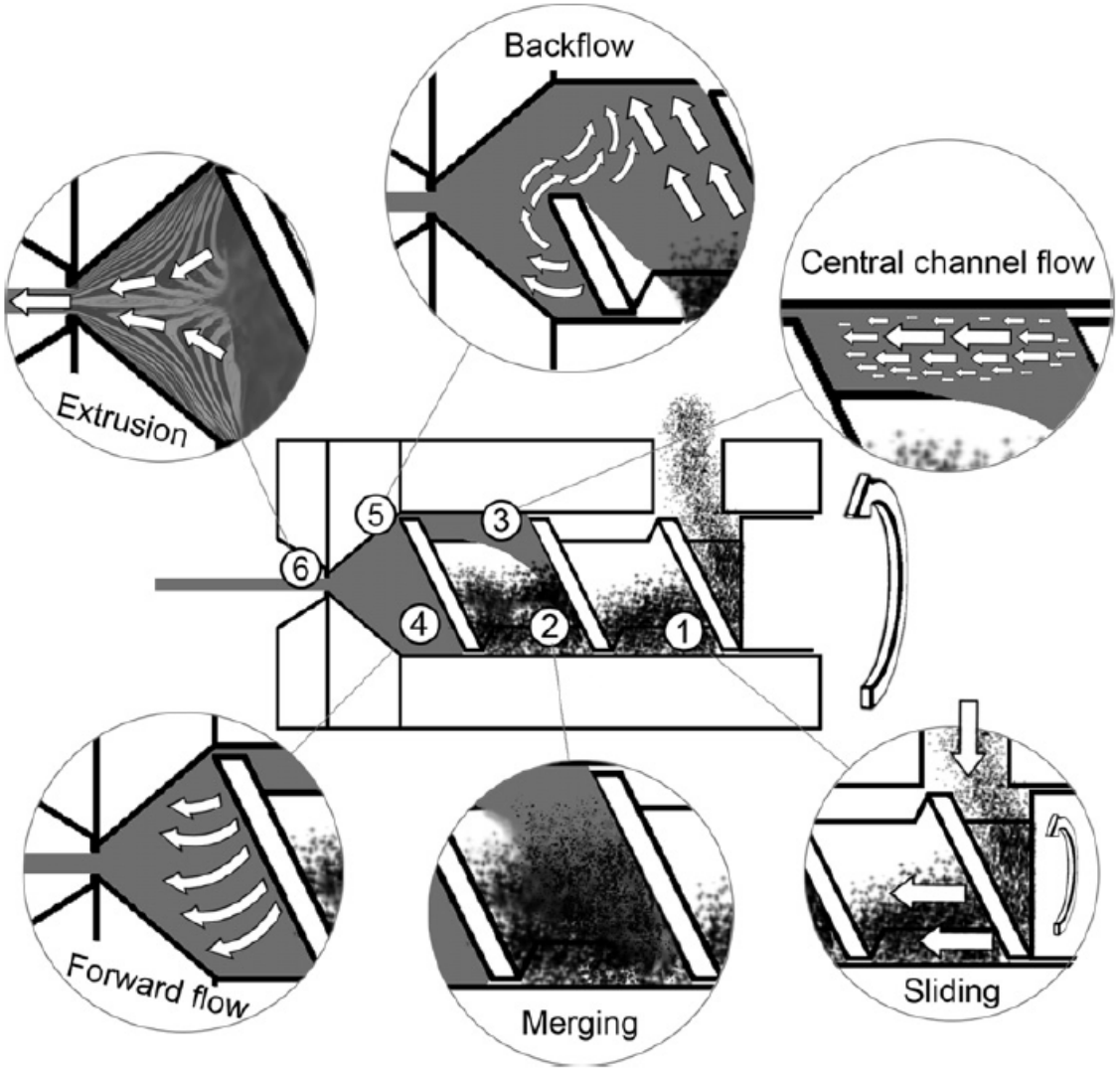

Figure 2.5: Illustration of material flow through 6 different stages in the screw extruder, from [6].

2.2.3 Strain contributions in screw extrusion

Recent works by Skorpen et. al. [8] have studied the accumulated strain during a screw extrusion operation. The total strain experienced came from the four last stages of material flow in the screw extruder.

The extrusion stage depends purely on the reduction of area, as with conventional ram extrusion. Although there's been observed a slight rotation of the extruded material, this was assumed to represent a negligible strain.

In the extrusion chamber region, a fully dense bulk material is moved forward by continuously arriving material from the screw channel. As the extrusion chamber has

a conical shape, the material experiences a strain contribution from the reduction of area. Another strain contribution comes from the rotation of material inside the extrusion chamber. The formed "billet" experiences decreasing rotational speed down the conical chamber, closer to the extrusion die, resulting in torsional strain similar to that of high pressure torsion (HPT).

The screw tip continuously smear thin slices of material onto the solid metal plug in the extrusion chamber, i.e. continuously depositing new layers of metal onto the "billet". This smearing corresponds to shear strains similar to that of machining.

The compacted material in the screw channel is forced forward by large stress components due to screw movement and high viscosity shear strains along the screw channel in a helical pattern. Sticking friction is assumed to be pinning the material displacement through the screw channel. As a result of this, the compacted material will experience repeated shear deformation due to the rotational movement.

The total strain experienced by the extruded material will be the sum of strains experience from the compacted stage and through to the reduction at the die.

Applying varying screw rotation and feeding rates affects the total effective strain by a substantial amount. Increasing the screw rotation and decreasing feeding rate results in an increased total strain. The effect of varying the screw rotation and feeding rate was systematically seen in the extrusion chamber and screw channel. In these two stages an increase in strain can be achieved with increased rotational movement. Optimizing the feeding rate and screw rotation, total equivalent strains of up to 18-20 can be achieved. However, this starving condition leads to low productivity. Total equivalent strains of 10-15 can be achieved with varying feeding rates and screw rotations of 8-10RPM [8].

2.2.4 Degreasing of granules

Degreasing of aluminium granules prior to screw extrusion is of outmost importance for avoiding an introduction of undesirable impurities to the extruded product. Such impurities may originate from lubricants and other environments. Degreasing of granules may be performed in chemical solutions, e.g. acetone, or by thermal treatment. Cui [23] showed that degreasing aluminium scrap in acetone prior to thermal treatment resulted in a stable relative mass during heating. Acetone cleaning effectively eliminated potential residue, prior to the thermal treatment. Cui [23] also showed the release of various evolved gases during thermal treatment. A clear peak of CO_2 released at 365 °C was shown for acetone scrap. Further, Cui showed that the temperature leading to severe aluminium oxidation was 428 °C.

2.2.5 Effects of chemical composition on extrusion

The material properties influence the effectiveness of extrusion. Alloying elements is a contributing factor for flow stress, and thus extrusion pressure and speed. In the 6xxx alloy series, the extrudability are strongly affected by the Mg and Si contents. Reiso [2] showed that the increase of Si by 0.01wt% reduced the extrudability by 1-2%. Similarly, increasing the Mg content up to 0.55wt% have the same significant effect. These alloying contents determine both deformation resistance and

the solidus temperature. While the solidus temperature is more sensitive to the Si content, the Mg content affects the deformation resistance and thus flow stress and heat generation. Maximum extrusion speed before tearing at the surface is thus lowered with a lowered solidus temperature and increased heat generation.

2.3 Heat treatment

Heat treatable aluminium alloys typically have a complex thermal history (see Figure 2.6). Starting by DC-casting, followed by homogenization and extrusion, then artificially aged. A separate solution heat treatment can be done in between extrusion and artificial aging. This step is performed when the finished product have a desired maximum strength as given noted by the thermal state T6. The relevant thermal states for this thesis is given Table 2.2.

Table 2.2: Standard temper designations for aluminium alloys [24]. Relevant tempers for this thesis are listed.

Temper	Description
T1	Elevated-temperature shaping process, cooled, and naturally aged to a stable condition
T4	Solution heat treated (SHT) and naturally aged to a stable condition
T5	Extruded and artificial aged to peak hardness/strength
T6	SHT and artificial aged to peak hardness

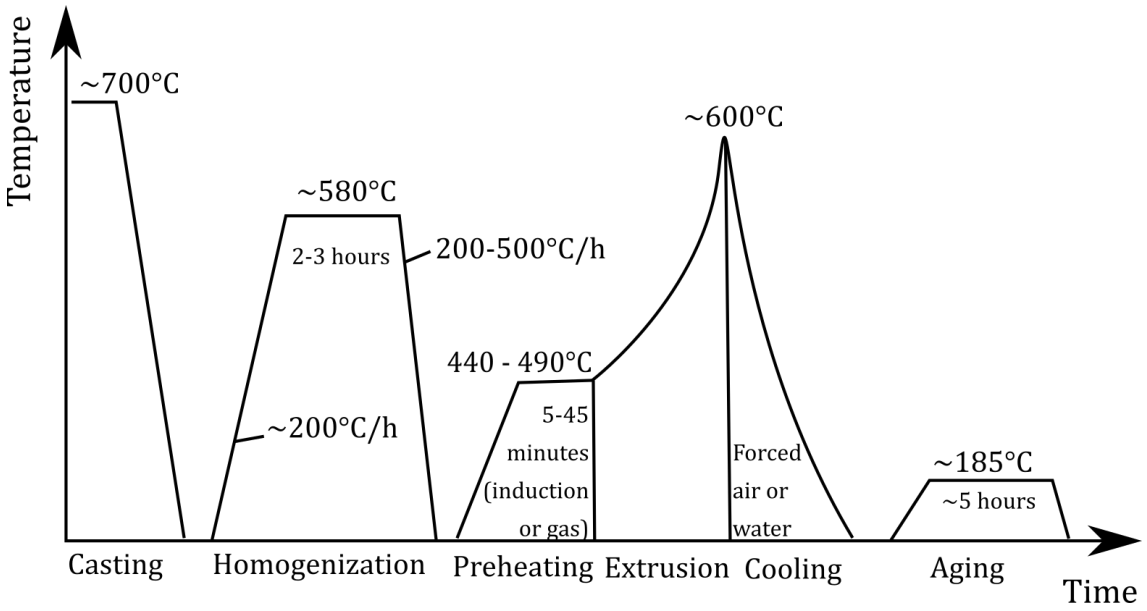

Figure 2.6: Sketch of the thermomechanical history for AlMgSi alloys. Sketch modified from [2]. This temperature time profile does not include solution heat treatment, after extrusion.

2.3.1 Homogenization

The process of homogenization is applied to as cast AlMgSi billets to improve extrudability. Homogenization involves dissolving and replacing interdendritic cast eutectic structures from β-AlFeSi plates with round α-Al(Fe,Mn)Si particles [25]. These α-particles improves the extrudability and surface quality of the extruded material [26]. Homogenization also precipitate dispersoids which take part in controlling grain size during extrusion. While high homogenization temperatures is beneficial in dissolving the eutectic structures, it has a detrimental effect on the distribution and number density of dispersoids and thus the controlling of grain size [27].

2.3.2 The principles of age hardening

In order to achieve maximum mechanical properties of AlMgSi alloys it is necessary to ensure a high solute content prior to aging [17]. The highest aging potential can be ensured by either a separate solution heat treatment, or avoiding formation of (Mg,Si) precipitates in as extruded profiles [17]. To achieve temper T6 a heat treatment procedure including the following processes is needed: solution heat treatment, rapid cooling and age hardening [28, 29]. Similarly, for achieving T5 quench sensitivity and age hardening is needed. For T1, quench sensitivity is the most important factor.

Solution heat treatment

The purpose of solution heat treatment (SHT) in AlMgSi alloys is to dissolve Mg and Si particles for further maximizing the age hardening potential during aging. This process is performed at an elevated temperature and held for a sufficient amount of time for the constituent elements to go into solid solution.

Proceeding the holding time, the material is quenched to retain the constituent elements in the meta stable SSSS within the aluminium matrix. For AlMgSi alloys the extrusion process may achieve SHT temperatures [28].

Quench sensitivity

Age hardening response for heat treatable alloys can be affected by the cooling rate from an elevated temperature process. For optimization of the mechanical properties, precipitation during cooling must be completely suppressed. Amongst the chosen alloys for this thesis, 6082 is most quench sensitive. In other words, 6082 is most susceptible for precipitating coarse β-Mg_2Si when the quench rate is not sufficiently high. Shang et. al. [30] found the highest transformation rate from SSSS to β'' and β' occured at the critical temperature of 360 °C. Further, Shang et. al. showed that the minimum quench rate of 15 °C s^{-1} in the intermediate temperature range of 250-440 °C is needed to achieve optimum mechanical properties. With quench rates above 15 °C s^{-1}, the obtainable hardness is over 95 % of maximum property [30]. The highest rate of precipitation happens at the tip of the 'C nose' in the TTT curve (see Figure 2.7). The high driving force for phase transformation and high diffusion rate of solute atoms leads to the formation of Mg_2Si precipitates.

The precipitation of both β' and β result in low concentrations of solute elements, restricting the volume fraction of precipitated β'' in the subsequent age hardening process.

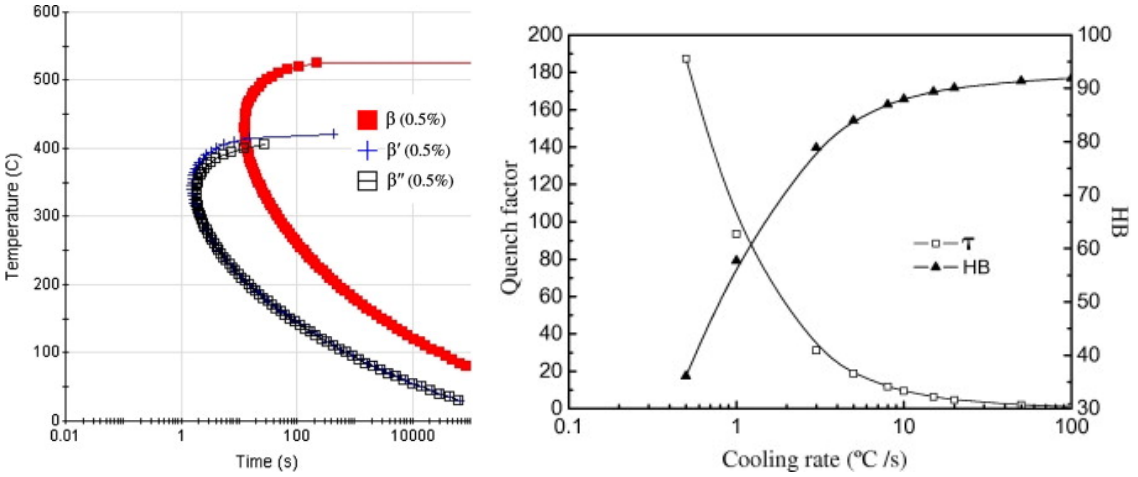

(a) TTT curves for 6082 precipitates. β'' and β' precipitates have the C nose temperature of 360 °C, while the C nose temperature of β phase is higher.

(b) Effect of average cooling rate on predicted hardness (HB) and quench factor (τ) on 6082.

Figure 2.7: From [30].

Age hardening

The process of aging, or age hardening, can be performed by either natural aging or artificial aging. Both processes decomposes the age hardening elements in SSSS to form finely dispersed precipitates. The geometry, size and volume fractions of these precipitates determine the hardening response and thus the mechanical properties of the material [14, 28, 29].

Natural aging takes place in room temperature and can be measured by change in mechanical properties over time. This natural aging effect can be suppressed by cooling the material down to a low temperature below −10 °C [28]. Artificial aging of Al-Mg-Si is performed at an elevated temperature, normally in the range 150-200 °C [14]. The degree of age hardening depends on temperature and holding time.

2.4 Recovery, recrystallization & grain growth

Plastic deformation have several effects on the resulting microstructure and properties, i.e. change of grain shape, strain hardening, and increase in dislocation density. During deformation some of the inflicted energy is stored in the metal as strain energy. Stress- and strain-fields represent stored energy in zones of tensile, compressive and shear forces on the newly created dislocations. These zones may be restored by appropriate heat treatment through two processes: recovery and recrystallization. Grain growth may follow if the metal is present in an elevated temperature for too long.

Stored internal energy is relieved through dislocation movement during recovery, by increased atomic diffusion at an elevated temperature or over time. The number of dislocations will be reduced some by annihilation and rearrangement of dislocations, producing lower overall strain energies. Point defects and point defect clusters are annealed out [31].

After the recovery, the energy stored from strain fields will still be relatively high in the grains from deformation (i.e. ram or screw extrusion). In recrystallization however, strain free grains will form and grow from small nuclei, consuming the parent grains, due to the mobility of high-angle boundaries. The new equiaxed grains will have low dislocation densities, and large change of texture. The degree of recrystallization depends on both time and temperature [31]. In 6xxx alloys, Mn and Cr form dispersoids which inhibit recrystallization. The spatial distribution and number density of these dispersoids will influence the final grain sizes.

If the strain free grains are left further at an elevated temperature, the recrystallized grains will grow. The driving force for grain growth is the reduction of total energy related to grain boundary (GB). This phenomenon occurs through migration of GBs. The growth of grains is at the expense of smaller grains that shrink [31, 32].

2.5 Strengthening mechanisms

The absence of strengthening defects in pure aluminium, e.g. solute atoms, precipitates, GBs and other dislocations, corresponds to little resistance for dislocation movement. The number of dislocations in motion corresponds to the plastic deformation. By hindering the ability of dislocations to move in a material translate to hardening and strengthening of said material. Precipitation strengthening is the dominant strengthening mechanism in AlMgSi alloys [14, 33].

2.5.1 Precipitation hardening

The strength obtained from age hardening is the result of the interaction between dislocations and precipitates. Precipitation strengthening can occur either through shearable or non-shearable precipitates, i.e. weak or strong precipitates, respectively. These precipitates precipitate during aging hardening (natural or artificial). For an underaged condition coherent precipitates will be the dominant strengthening factor until an approximate peak aged condition is reached. After this stage, the material will enter a stage where breakdown of coherency will occur in the overaged condition. In other words, small shearable precipitates will be precipitated from SSSS until a peak aged condition is established. The stress will increase for the material with small shearable precipitates increasing in size and with more nucleation sites appearing. Large, non-shearable precipitates will appear at an overaged condition, where there is no solid solution left. Here the stress will decrease by coarsening; larger and fewer grains [34].

Lattice defects introduced during plastic deformation facilitates diffusion, and acts as nucleation sites for precipitation. A desired amount of defect concentration can be obtained by deformation, thus, influencing the distribution, size and quantity of precipitates. By optimizing the defect concentration with respect to recrystallized

grain, one can improve creep strength, and fatigue strength and toughness.

2.5.2 Grain boundary strengthening

The average grain size in polycrystalline metals influences the mechanical properties. Dislocation movement or slip must take place across the grain boundary between adjacent grains. This boundary however, acts as a barrier for dislocation movement. For high-angle boundaries, dislocations pile up at grain boundaries introducing stress concentrations at this intersection. Dislocation pile up like this generates new dislocations in the adjacent grains. Thus, large grain size will have increased number of dislocations in the pile up. Materials with refined grains will be harder and stronger due to the larger grain boundary area per dislocation. This refinement of grains can be related to the yield strength σ_y with the Hall-Petch equation 2.6 below:

$$\sigma_y = \sigma_0 + k_y d^{-}1/2 \tag{2.6}$$

where d is the average grain diameter, σ_0 and k_d are material constants [32]. It should be noted that the Hall-Petch relationship is not valid for polycrystalline metals with either very coarse or very refined grains. For small-angle boundaries however, the modest misalignment of crystallographic direction is not effective as to hindering dislocation movement across the GBs.

Chapter 3

Experimental procedures

This chapter covers the various materials and processes employed in the present work. A flowchart summarizing the materials thermal and processing history, and where the material were characterized are presented in Figure 3.1. 'Characterization' encompasses the use of optical microscopes (OM), hardness testing and electrical conductivity measurements.

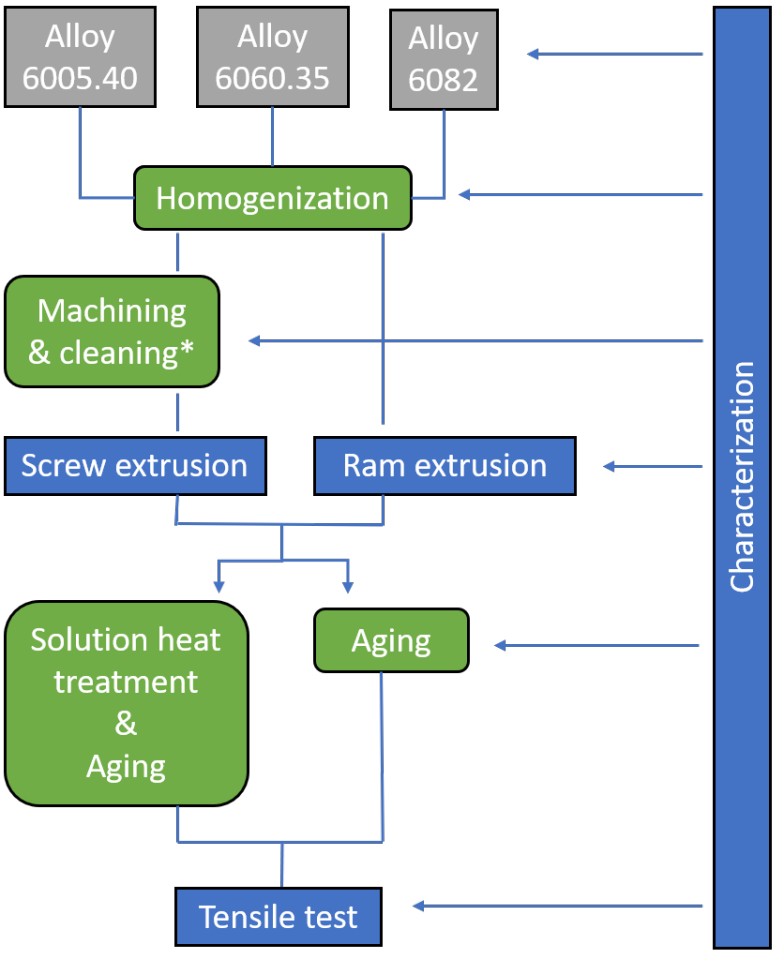

Figure 3.1: Work flow sheet illustrating the type and sequence of investigations. Characterization involves the use of OM, hardness testing and electrical conductivity measurements. *) Acetone and thermal cleaning at 350 °C for 4h.

3.1 Base material

All three materials used in this thesis belong in the 6xxx series. These are 6060.35, 6005.40 and 6082, all DC-casted and homogenized at Hydro Aluminium AS Sundalsøra (see Figure 3.2). Chemical composition of these alloys are given in Table A.1 (Appendix A), analysed by Hydro Sunndalsøra.

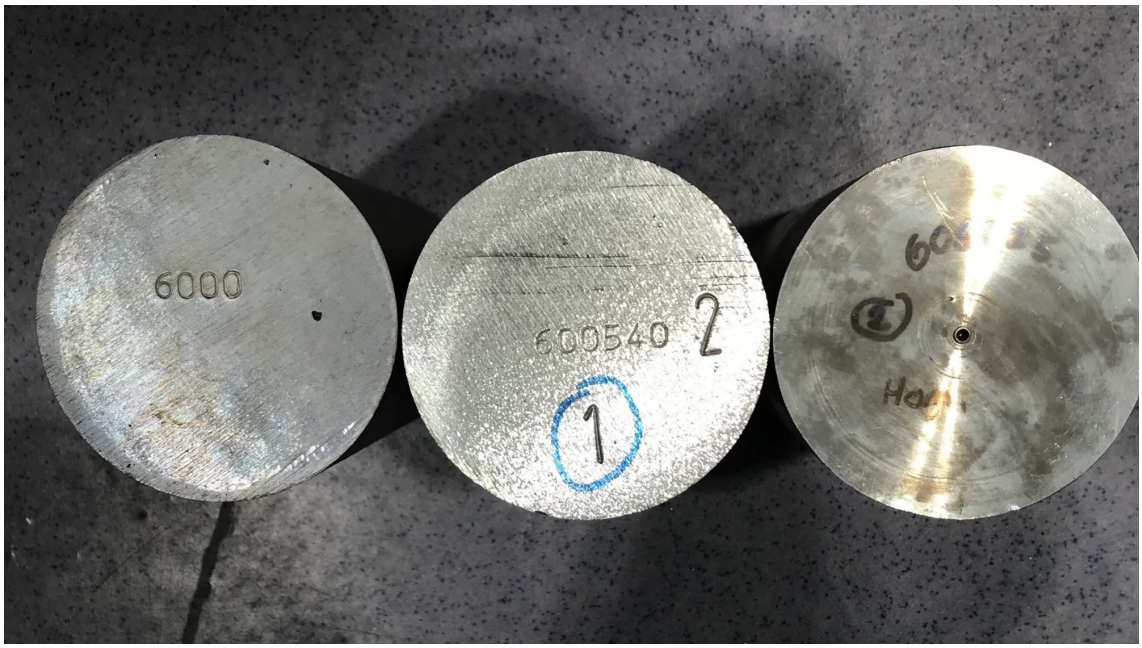

Figure 3.2: Billets in the 6xxx series. The billet to the left labelled 6000 is the 6082 billet. The middle and right billet is 6005.40 and 6060.35, respectively.

The homogenization followed an industrial standard procedure for homogenization. The homogenization procedure follows Table 3.1. All alloys were homogenized by Hydro Sunndalsøra prior to receiving the material.

Table 3.1: Homogenization of billets. Homogenization procedure performed by Hydro Sunndalsøra on all three alloys: 6060.35, 6005.40 and 6082. RT: room temperature.

Heating rate:	RT - 575 °C	200 °C h^{-1}
Homogenizing:	575 °C	2 h15 min
Cooling rate:	575 °C - RT	400 °C h^{-1}

3.2 Machining & Cleaning

Homogenized material were machined into granules by a NTNU workshop and further shredded with a Getecha RS1600 granulator machine. The granules were shredded two times to the approximate length of 5 to 20 mm. However, due to the different initial geometry and size of the granules, it can be seen from Figure 3.3 that 6005.40 have longer granules and a larger size distribution compared to the more square shaped 6082, and 6060.35.

Figure 3.3: Granules of each alloy after shredding.

Thereafter, the granules were degreased with acetone for 30 min to dissolve grease and other contaminants. This was performed in a 25 L polypropylene (PP) waste container. The granules and acetone were further screened with a 5 mm mesh sieve, allowing the acetone to drain off. The drained acetone were collected in a 10 L PP bucket for further degreasing. Drained granules were placed on an Al-foil covered tray for drying. All equipment (see Figure 3.4) were rinsed with water to remove any granule remnants prior to each degreasing procedure.

First step of the proceeding thermal treatment was drying the granules for 24 h at approximately 125 °C to evaporate most of the residual acetone.

Based on the work by Cui [23], the granules were then thermally degreased in an air circulation furnace at 350 °C for 4 h to burn of residual acetone and organic matter. To ensure evaporation of the residual acetone, the granules were flipped and stirred with 1 h intervals.

Figure 3.4: Acetone degreasing equipment. 1) - PP waste container for degreasing granules with acetone; 2) - 5 mm mesh sieve for screening acetone out of the granules; 3) - 10 L PP bucket for collecting screened acetone; 4) - Al-foil covered tray for acetone degreased granules.

3.3 Extrusion

The materials were screw and ram extruded from granules and billets, respectively. To ensure comparable results, both processes were performed with as many equal parameters as possible. Hence, both processes used a die orifice of 10 mm and both water quenching and air cooling were performed after extrusion. These extrusion processes will be described in detail below.

From this point in the thesis, the extruded material will be annotated as a function of process, alloy, and cooling method, e.g. RE6082AC, SE6060.35WQ.

3.3.1 Screw extrusion

Screw extrusion was performed by feeding granules into the screw channel, setting the screw rotation to a given speed, and heating the tooling and plug by induction. The temperatures were controlled and maintained by slight adjustments to the induction and air in the front and back of the screw. Six thermocouples were used to

get accurate temperature control in the screw channel, extrusion chamber and die orifice. The screw extrusion set up can be seen in Figure 3.5.

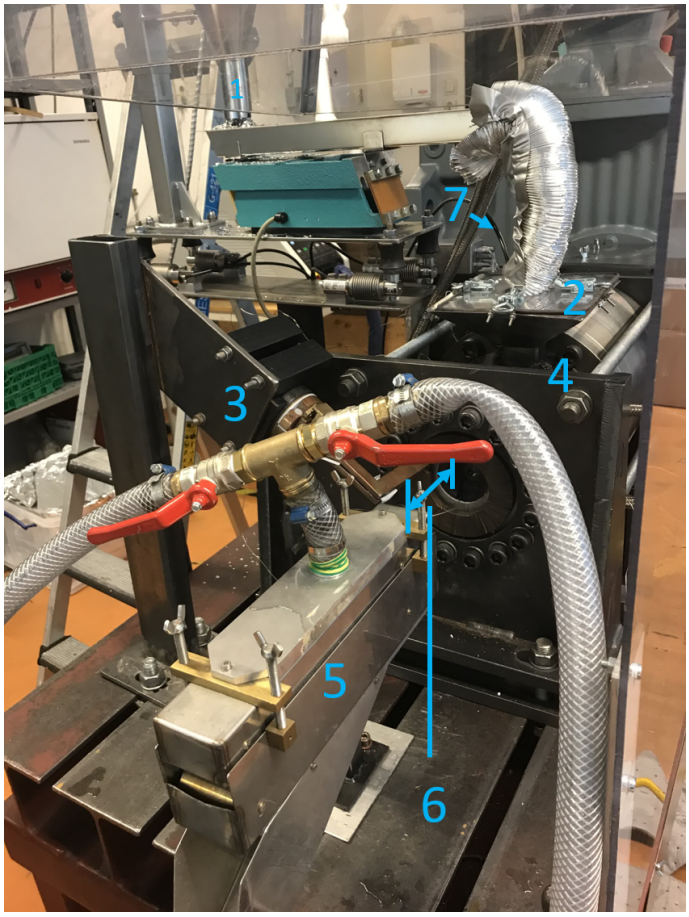

Figure 3.5: Assembled screw extruder ready prior to an experiment. 1 - feeder funnel leading down to the vibrating feeder. 2 - granule catcher into the screw extruder feeding hole. 3 - induction coil. 4 - the screw extruder. 5 - water quenching system. 6 - 30cm distance from die orifice to the water quenching starts. 7 - gas tube mounted on and flushing down nr. 2.

Each alloy was flushed with an inert or semi-inert shield gas during feeding to avoid oxidation of the granules. Shield gas, liner and screw rotation of each alloy are presented in Table 3.2. Aiming point for the extrusion temperature was 540 °C. The extrusion experiments were logged (see Appendix B) with respect to the relevant parameters.

3.3.2 Ram extrusion

The ram extrusion were performed on the SINTEF extrusion press for Ø95mm billets. The billets were induction heated to 500 °C prior to being put into the Ø100mm extrusion chamber. The material were steady state extruded with most of the extrudate coiled and water quenched, while the last extrudate length were air cooled (approximately 2.5 m). The extrusion experiments were logged (see Appendix C) with respect to the relevant parameters. Figure 3.6 shows a sketch of the ram extrusion setup.

Table 3.2: Overview of screw extrusion parameters for each alloy. *60% of max. flow, where 2NL/min is max. NL/min: normal litre per minute, at 0 °C and 1 atmosphere.

Alloy	Diameter [mm]	Liner	Atmosphere	Gas-flow	RPM
6082	9.92	Old	Argon	N/A	6-9
6060.35	9.92	Old	CO_2	60% of max.*	6-10
6005.40	9.92	New	CO_2	60% of max.*	10

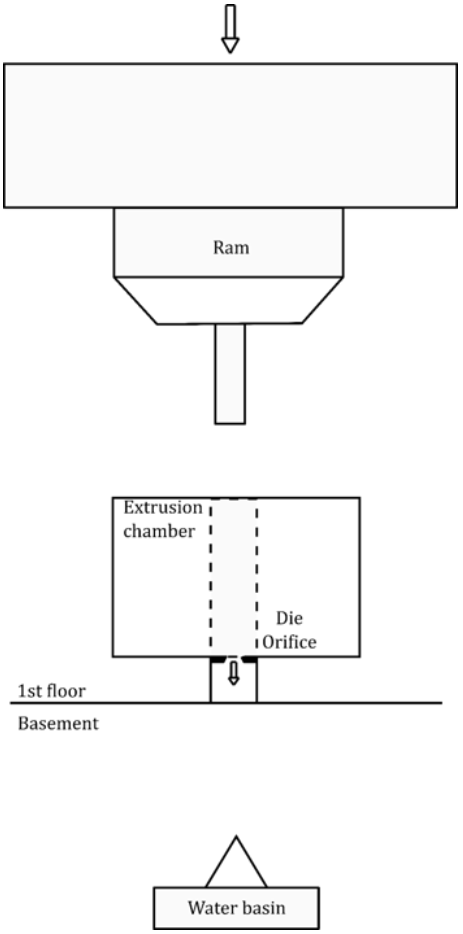

Figure 3.6: Sketch of the ram extruder with the ram stem pushing down in the Ø100mm extrusion chamber, through the die orifice of Ø10mm. The extruded profiles went down through a hole in the floor and coiled up in a water basin in the basement. The last approximate 2.5 m hung from the die orifice, before air cooling on the floor.

3.4 Solution heat treatment & aging

To find the temper T5 and T6 for all the conditions, aging curves were made from as extruded samples and samples from a separate solution heat treatment step.

All conditions were solution heat treated at 550 °C for 10 min, holding from 545 °C. The solution heat treatment procedure was performed in air circulation furnace

Nabertherm N 30/85 HA. All samples were water quenched subsequent to the solution heat treatment.

Extruded samples and SHT samples were age-hardened in Nabertherm N15/65HA air circulation furnace at 175 °C. Aging intervals ranged from 1 h to 3 d. Tensile specimens were aged to maximum hardness, found from aging curves.

3.5 Characterization of microstructure & grain structure

3.5.1 Sample preparation

All samples were ground and polished prior to microscopy examination. Grinding and polishing were performed with the Struers Tegramin-5 and TegraForce-5. The procedure follows the steps introduced in Table 3.3. Samples prepared for hardness measurements were polished until the third step.

Table 3.3: Procedure for polishing Al alloys.

Process	Surface	Lubricant/ Suspension	Velocity (RPM)	Cleaning
Grinding	MD-Molto 220	Water	300	Water, soap, ethanol, drying
Grinding	MD-Largo	DiaPro Allegro/ Largo 9 µm	150	Water, soap, ethanol, drying
Polishing	MD-Mol	DiaPro Mol R/ 3 µm	150	Ethanol, drying
Polishing	MD-Nap	DiaPro Nap R/ 1 µm	150	Ethanol, drying
Polishing	MD-Chem	OP-U NonDry	150	Ethanol, drying

Polished samples were anodized in 5 % HBF_4 for 90 seconds with an applied voltage of 20 V to reveal grain structure in cross-polarized light. The samples were promptly rinsed in water and ethanol, and dried after anodizing.

3.5.2 Microscopy examination

All samples were examined in Zeiss Axio optical microscope (OM). Polished samples were imaged in bright field for highlighting particle formation. Grain structure were analysed on anodized samples with cross-polarized light and a sub λ-plate with varying tilt in the column.

3.6 Characterization of mechanical properties

3.6.1 Hardness testing

Hardness was investigated throughout its processing history, i.e as received, as extruded, solution heat treated and artificially aged samples. Hardness tests were performed with the automatic Zwick Roell hardness test machine and manual Innovatest hardness test machine, using 1 kilogram force, and indentation dwell time of 10 seconds.

3.6.2 Tensile testing

The mechanical behaviour of the extruded profiles were found through uniaxial tensile testing. Each alloy was tested in temper T1, T5 and T6. Up to four tensile specimen were tested for each thermal state. To avoid undesirable precipitation, temper T5 and T6 were heat treated prior to machining by the NTNU mechanical workshop, while temper T1 specimens were freezed until machining. Dimensions of the tensile specimen are illustrated in Figure 3.7.

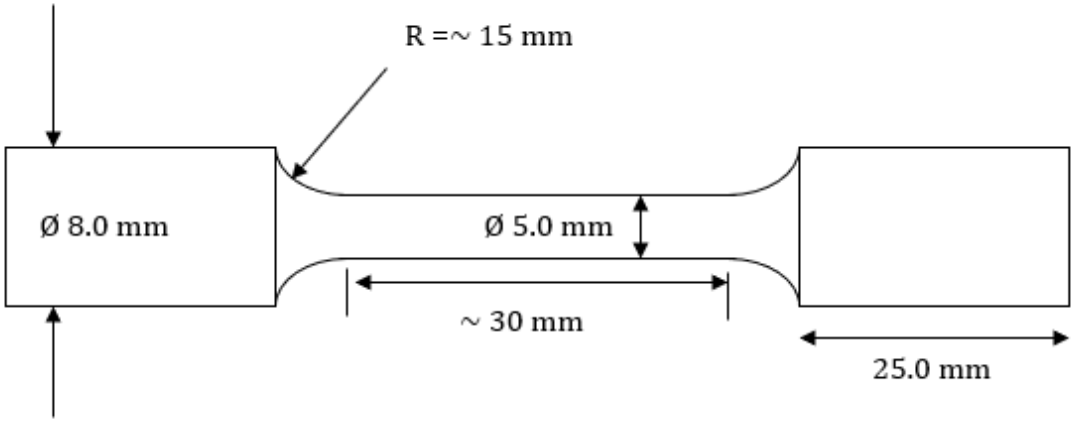

Figure 3.7: Tensile specimen dimensions.

Tensile testing took place approximately 2 weeks after machining ($\sim$ 4 weeks after samples were taken out of freezer). Certain tensile specimens were bent out straight by the workshop due to the coiling subsequent to ram and screw extrusion of the alloys. The tests were performed using a MTS 810 tensile machine. The machine was assembled with a 25 mm laser extensometer for measuring the engineering strain. Specimen diameter was noted for software calculations.

3.7 Conductivity measurements

The electrical conductivity was measured with the eddy current instrument SIGMATEST 2.069. The probe were calibrated with two standard reference materials. Conductivity measurements were performed with a frequency of 960 kHz to get reliable results with thin samples. Samples were measured while in ambient temperature to ensure reliable and accurate readings. Sample thickness was minimum 5 mm.

Chapter 4

Results

In this chapter, a summary of the measured properties and microstructure will be given for each alloy. First, a presentation of the received material prior to extrusion will be given. Second, a presentation the extruded profiles for each alloy will be given.

4.1 As received material

This section covers the microstructure, hardness and electrical conductivity of the homogenized billet materials, and thermally cleaned and shredded granules.

4.1.1 Mechanical properties & electrical conductivity

The initial hardness and electrical conductivity of the homogenized billet materials is shown in Table 4.1. 6005.40 hade the lowest hardness, and as expected 6082 has the highest hardness value. The electrical conductivity is increasing with decreasing alloying elements and is thus highest for 6060.35 with $29.9\,\mathrm{MS\,m^{-1}}$.

Table 4.1: Hardness and electrical conductivity of homogenized billet material.

Alloy	Hardness, HV1	Conductivity, MS/m
6060.35	53 ± 2	29.9 ± 0.2
6005.40	43 ± 1	29.2 ± 0.04
6082	61 ± 1	27.7 ± 0.1

4.1.2 Microstructure of billet material

Representative micrographs of the polished and anodized microstructure of homogenized billet materials are presented in Figure 4.1-4.3. The dispersoid containing 6082 exhibited particles homogeneously distributed at grain boundaries with a higher number density than 6005.40 and 6060.35. 6082 showed as expected a smaller average grain size, compared to 6060.35. The grain size of the three alloys are shown in Table 4.2. Determination of grain size was performed with the mean linear interception method.

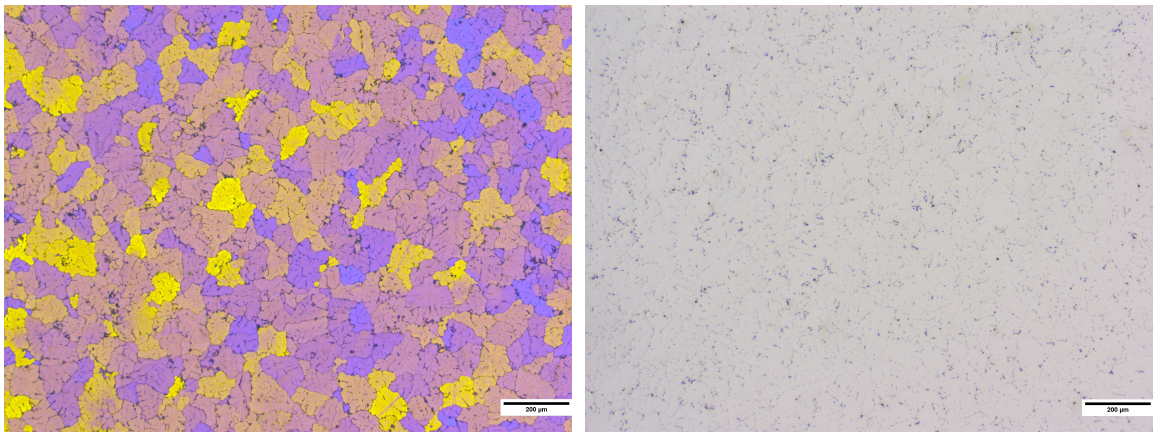

(a) (b)

Figure 4.1: Grain (a) and particle (b) structure in the cross sectional view of homogenized 6082.

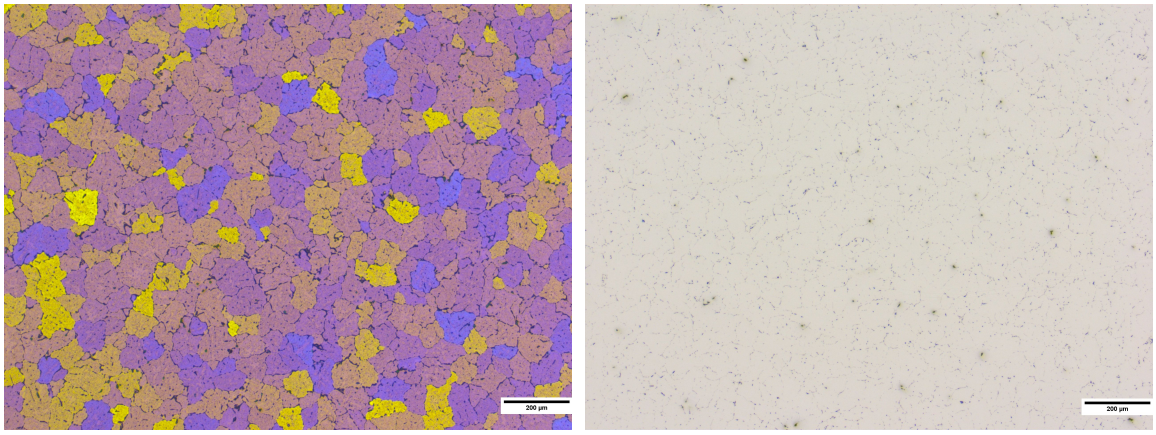

(a) (b)

Figure 4.2: Grain (a) and particle (b) structure in the cross sectional view of homogenized 6005.40.

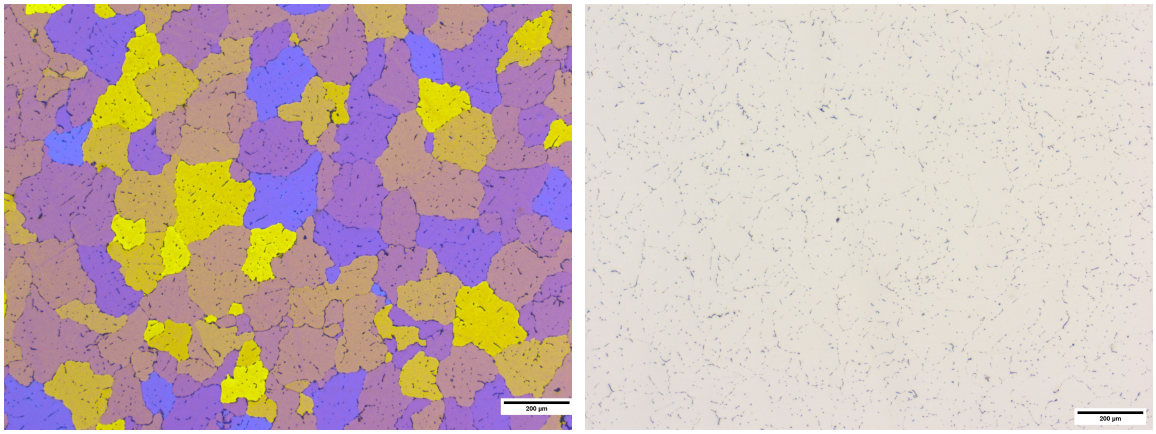

(a) (b)

Figure 4.3: Grain (a) and particle (b) structure in the cross sectional view of homogenized 6060.35.

Table 4.2: Average grain size in homogenized material determined from linear intercept method. Method devised in ASTM Standard E112, and performed in ImageJ [35, 36].

Alloy	6082	6005.40	6060.35
Mean Intercept length	60.5 µm	56.6 µm	100.8 µm

4.1.3 Microstructure of shredded material

As seen in Figure 4.4 the grain structure in 6082 granules exhibited a deformation structure of its initial homogenized structure, showing deformation bands, as result of the machining. The particle structure showed an alignment of particles in certain areas, possibly along the deformation bands. A similar pattern is shown across the 6060.35 granule in Figure 4.6 , but was not as apparent in 6005.40, Figure 4.5. The anodized grain structure of 6005.40 and 6060.35 showed recrystallized structure. The grain size of these recrystallized and deformed structures are listed in Table 4.3.

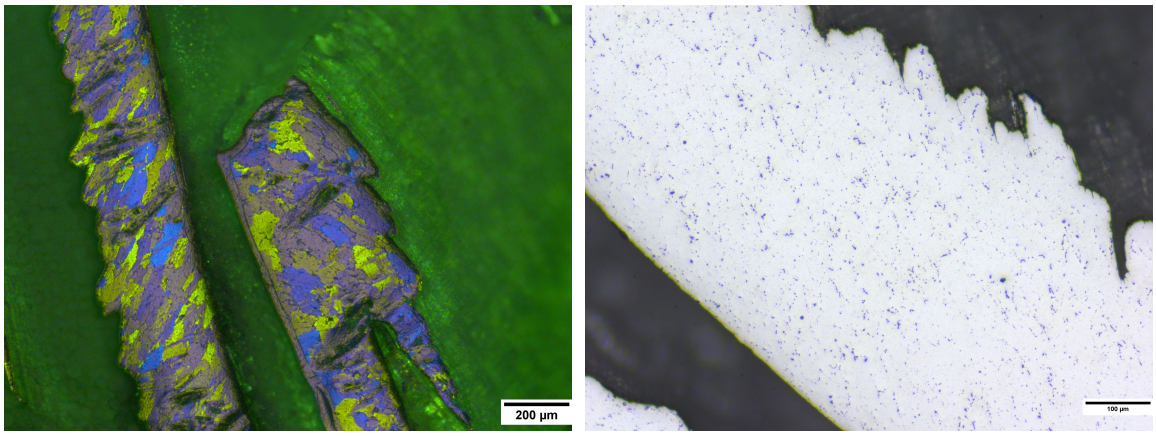

(a) (b)

Figure 4.4: Grain (a) and particle (b) structure of shredded 6082 material after thermal cleaning.

Table 4.3: Average grain size in shredded and thermally cleaned material determined from the linear intercept method. Method devised in ASTM Standard E112, and performed in ImageJ [35, 36].

Alloy	6082	6005.40	6060.35
Mean Intercept length	52 µm	23 µm	24 µm

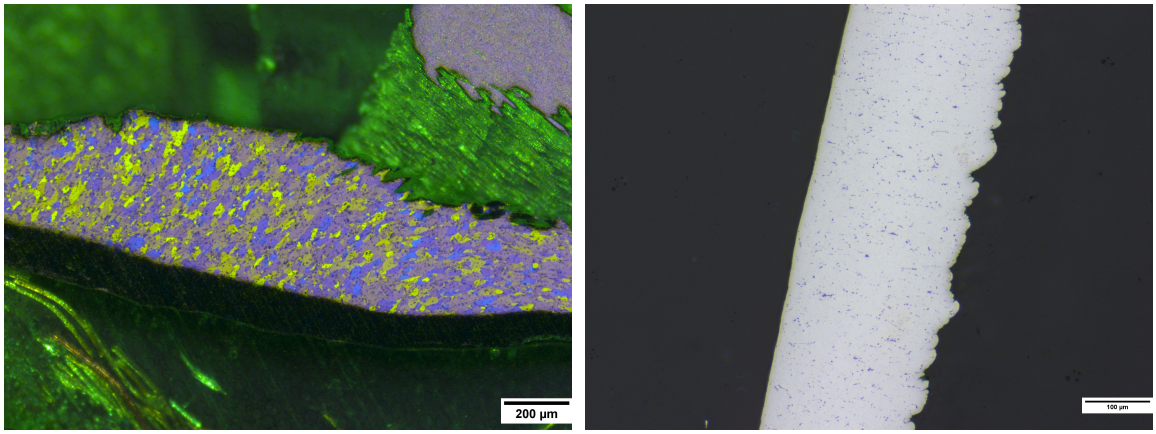

(a) (b)

Figure 4.5: Grain (a) and particle (b) structure of shredded 6005.40 material after thermal cleaning.

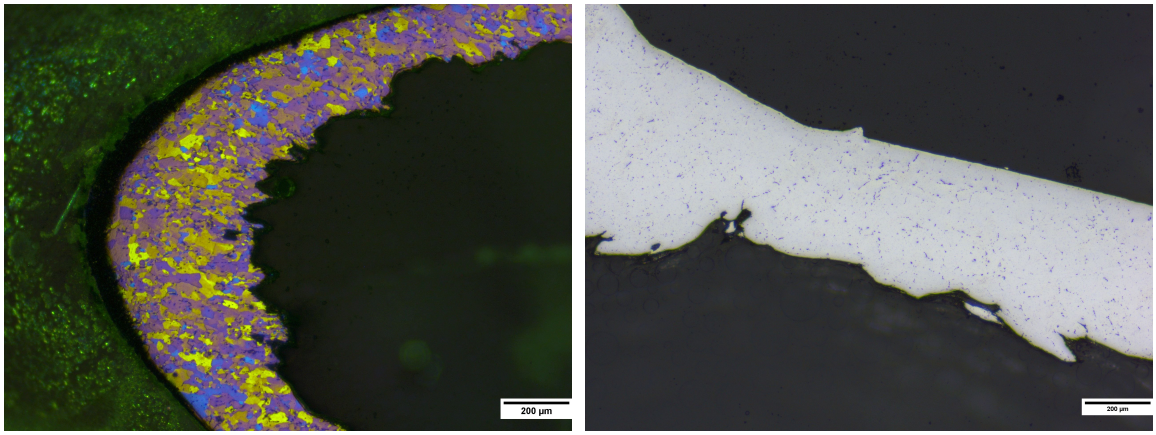

(a) (b)

Figure 4.6: Grain (a) and particle (b) structure of shredded 6060.35 material after thermal cleaning.

4.2 Extruded 6082 profiles

In Figure 4.7, a section of the surface quality on screw extruded 6082 can be seen. This alloy were extruded without any presence of tearing or blisters. Though, as seen in the aforementioned figure, a spiraling pattern is appearing on the surface of the air cooled length. Each spiral represent one screw rotation in the screw extruder, indicating a slow extrusion speed for this section.

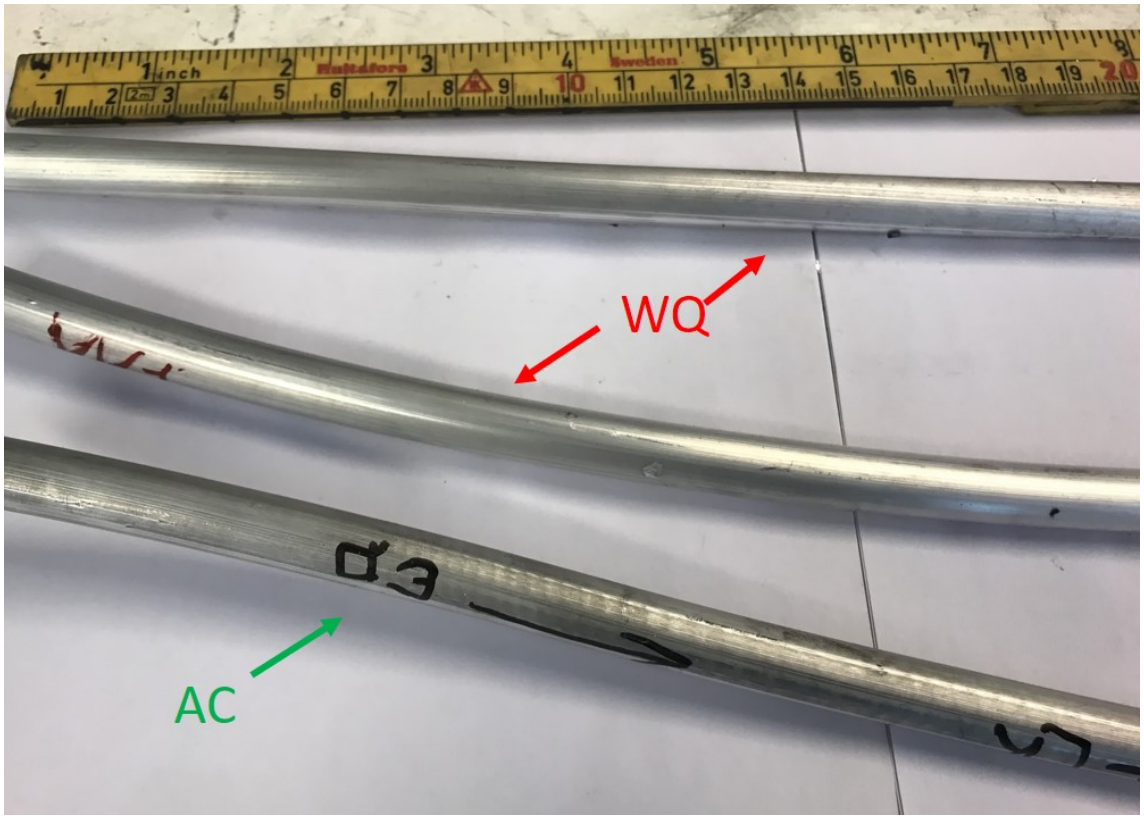

Figure 4.7: A section of the screw extruded 6082 profiles. The two on the top are water quenched (WQ) and the bottom profile is air cooled (AC).

An estimate of the extrusion speed were calculated for the screw extruded profiles, see Table 4.4. The extrusion speed is based on the feeding rate over a time interval, assuming steady-state extrusion.

The extrusion speed were split into air cooled sections and the last water quenched section. AC1 represents the extrusion speed for the first length after breakthrough at 6 RPM. AC2 and AC3 each represents a sudden peak of torque with a screw rotation of 8 RPM. The missing time interval between 40 and 57 min into the experiment is a result of a plug build-up in the screw channels. Generally the extrusion advanced in pushing motion, giving high extrusion speeds for a certain length, before stopping. This resulted in slow extrusion speeds of 0.031-0.063 m/min and 0.079 for air cooled and water quenched lengths, respectively. In comparison, the ram extrusion had an extrusion speed 581-1180 and 463 times faster than the screw extrusion from AC and WQ, respectively.

Table 4.4: Average extrusion speed for screw extruded 6082 profiles. Calculated from input mass difference at the given time intervals. 1 m corresponds to 212g of input material with a Ø10mm die orifice. Last column is the extrusion speed during the ram extrusion for comparison, from experiment nr. 13 in Appendix C.

	AC1	AC2	AC3	WQ	RE
Time interval [m/min]	24-40	57-79	79-85	85-110	N/A
Δ Mass [g]	100	190	80	420	N/A
Speed [m/min]	0.031	0.041	0.063	0.079	36.6

4.2.1 Mechanical properties & electrical conductivity

The hardness evolution (Figure 4.8) of the extruded profiles were determined for as extruded and solution heat treated samples. For the as extruded samples it can clearly be seen that the water quenched samples give higher hardness and accompanying lower electrical conductivity (Figure 4.9). This shows the quench sensitivity of 6082, and the effect of retarding precipitation during extrusion. The lower hardness of SE6082WQ compared with RE6082WQ was a result of the slower extrusion speed and thus slower water quenching during extrusion. Temper T5 was seen to be achieved earlier for higher hardness values. Temper T1 values representing the properties as extruded, without artificial aging, was shown at point 0.1 on the log time-axis.

Similarly for the SHT samples in Figure 4.10 and 4.11, the samples with highest hardness have the lowest conductivity. For SHT and aged samples, RE6082AC reaches temper T6 with approximately 13HV higher than RE6082WQ, and a bigger difference to the screw extruded samples. SHT SE6082 reaches temper T6 approximately at the same hardness conductivity after aging for 7h. Temper T4 values representing the properties as solution heat treated, without artificial aging, are shown at point 0.1 on the log time-axis.

To check if the differences in hardness at temper T1, T5 and T6 translates to the strength, nominal stress-strain curves are shown in Figure 4.12-4.15. As seen in these figures, some of the fracture strains appeared outside of the extensometer giving invalid results. The fractures strains (Figure 4.19) for these samples were therefore calculated from the actuator movement, assuming all samples had a length of 30 mm between the shoulders as per the dimensional drawing in Figure 3.7, Chapter 3.6.2.

SE6082WQ can be seen to have a tendency of temper T1 tensile tests being stronger than for temper T5. Both tempers have a considerable work hardening effect.

The main findings from the tensile tests, such as ultimate tensile strength (UTS), yield strength (YS), uniform elongation and elongation at fracture (EL), were collected from each stress-strain curve and presented in Figure 4.16-4.19.

All properties at temper T1 and T5 appear to be quite scattered. In these tempers, SE6082AC have lowest strength and highest ductility. However, for temper T6 these four properties seem to converge with RE6082AC having slightly higher strength and lower elongation. Overall, water quenched tensile specimen ductility properties changes the least from T1 to T5 and T6.

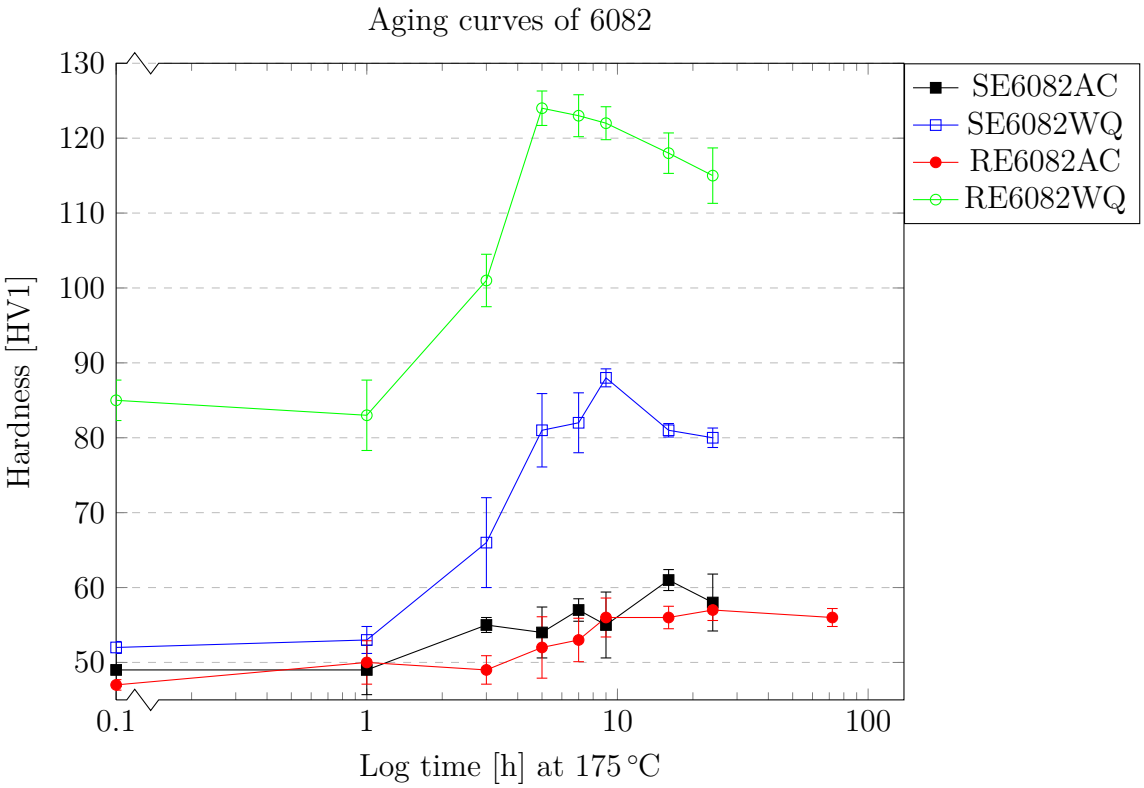

Figure 4.8: Hardness evolution with aging time at 175 °C for 6082 from ram and screw extruded profiles, both air cooled and water quenched.

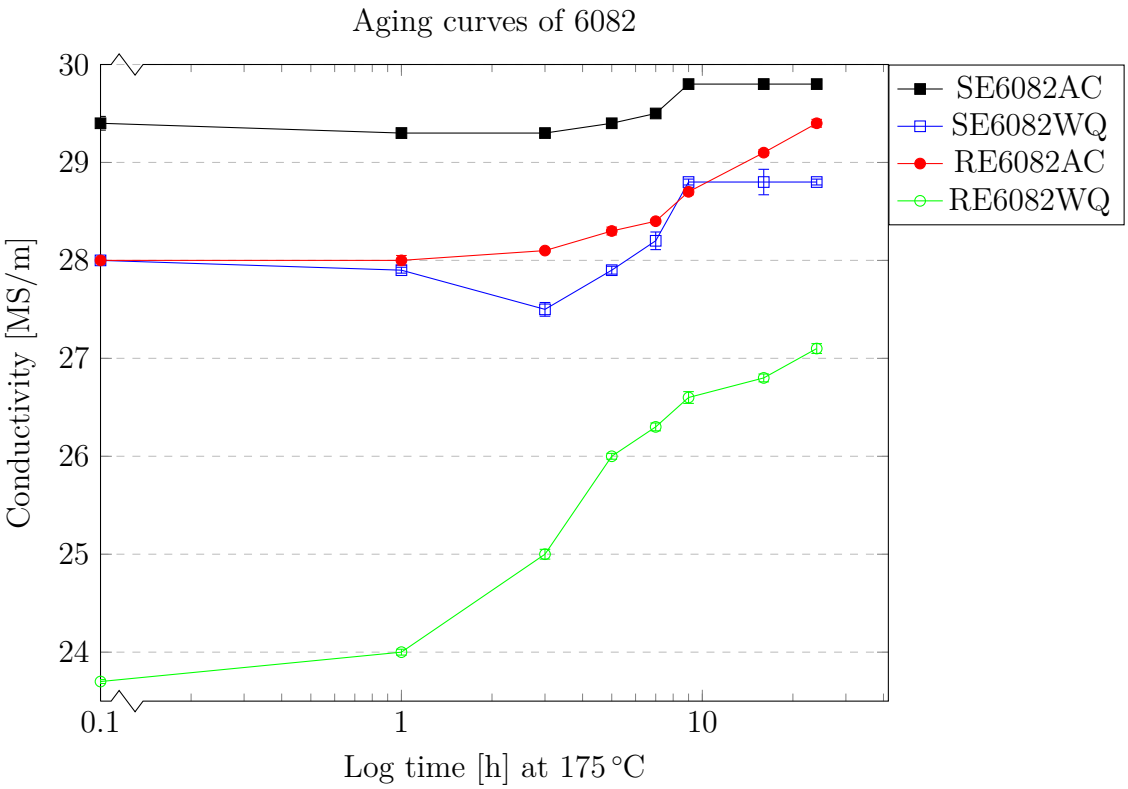

Figure 4.9: Electrical conductivity evolution with aging time at 175 °C for 6082 from ram and screw extruded profiles, both air cooled and water quenched.

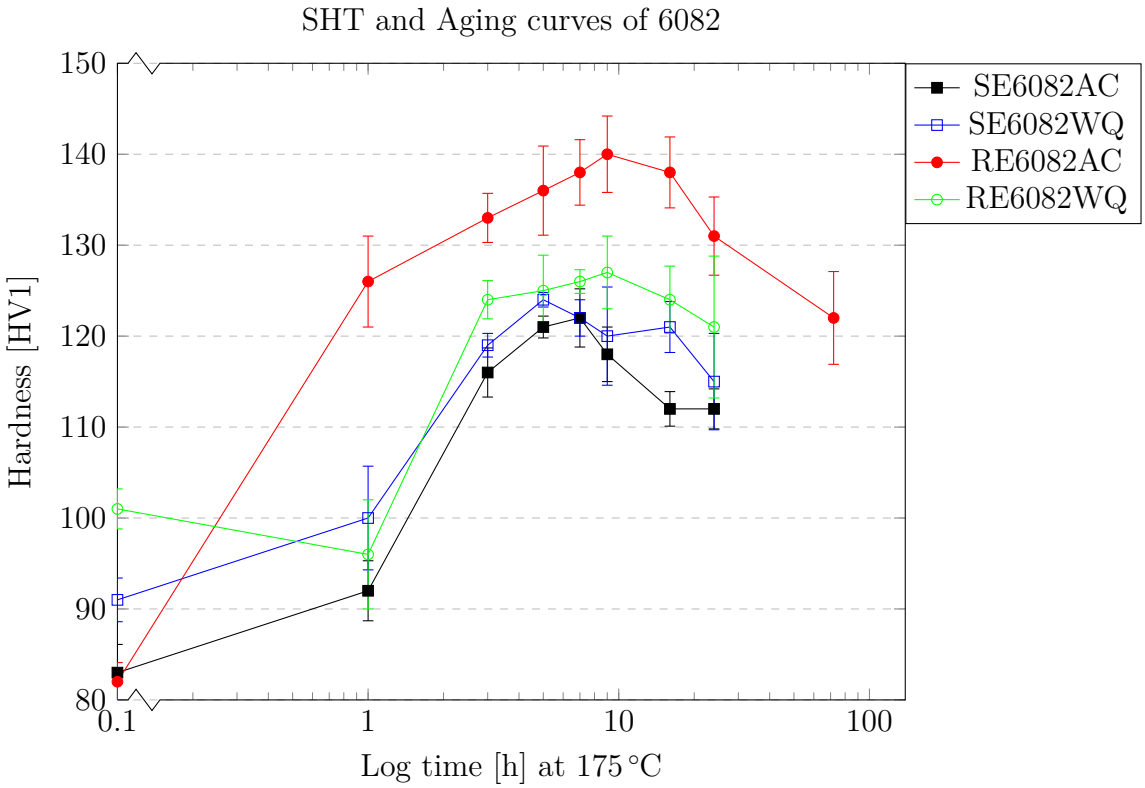

Figure 4.10: Hardness evolution with aging time at 175 °C in SHT 6082 for ram and screw extruded profiles, both air cooled and water quenched.

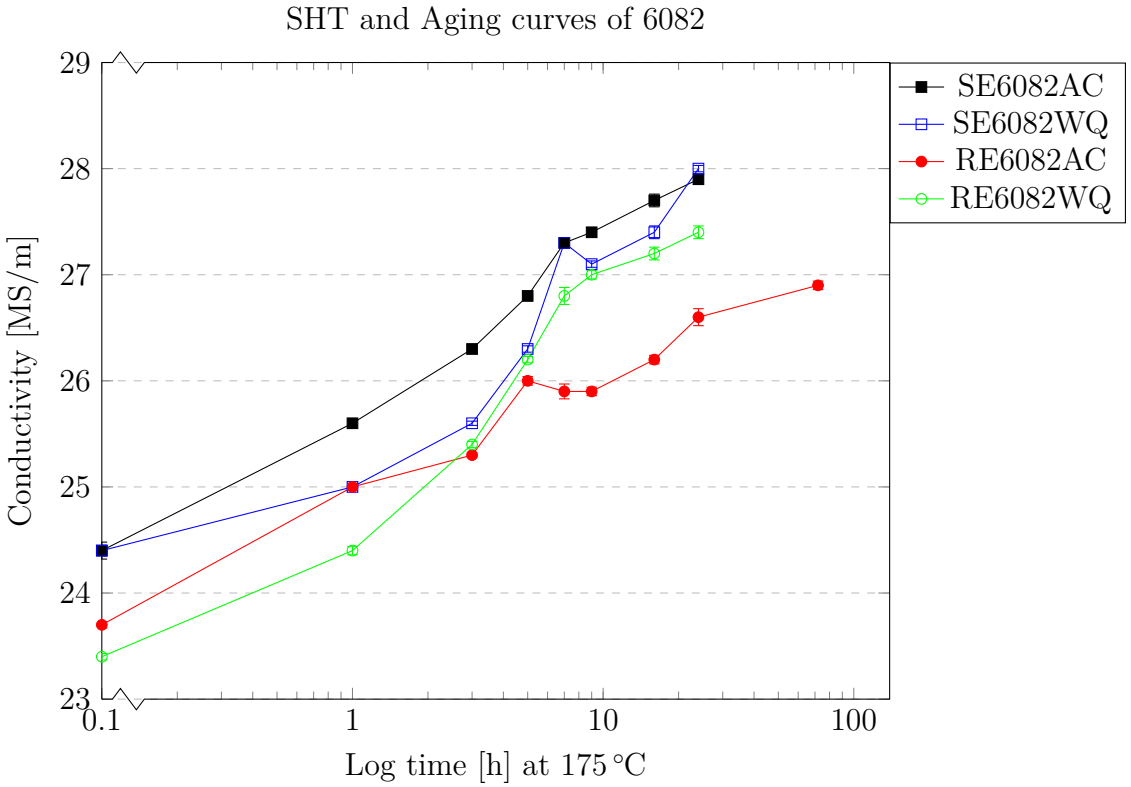

Figure 4.11: Electrical conductivity evolution with aging time at 175 °C in SHT 6082 for ram and screw extruded profiles, both air cooled and water quenched.

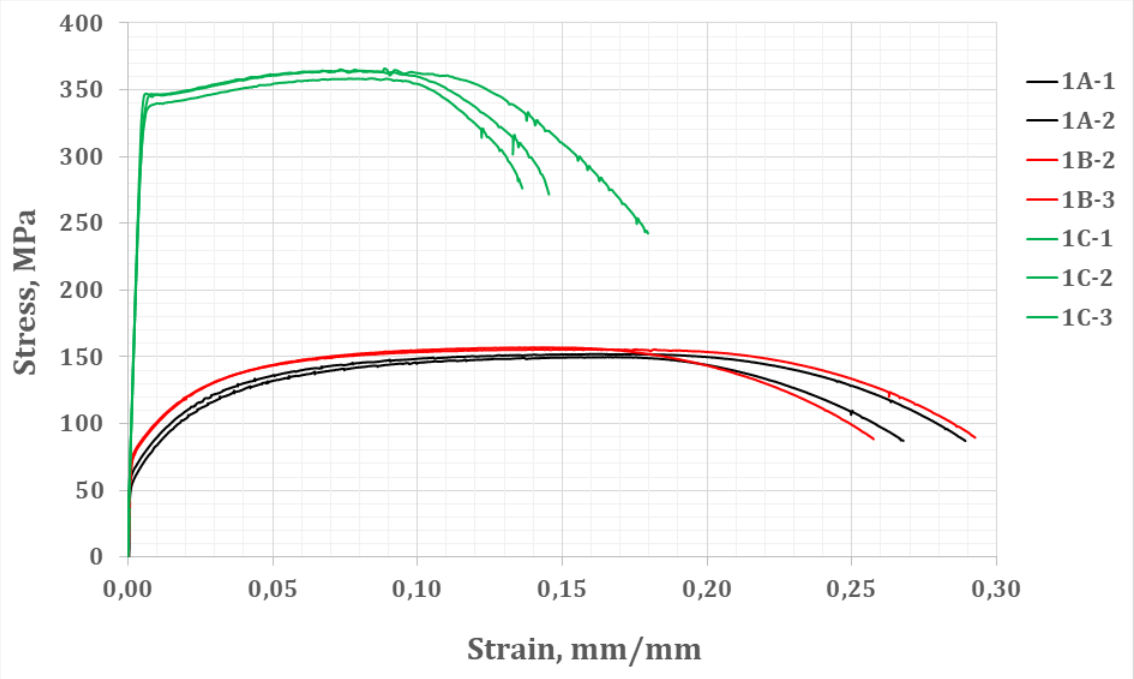

Figure 4.12: Stress-strain curve for SE6082AC. Black lines (lower) represent the as extruded profiles, temper T1. Red lines (upper) represent aged to maximum strength, temper T5. Green lines represent the solution heat treated and aged to maximum strength.

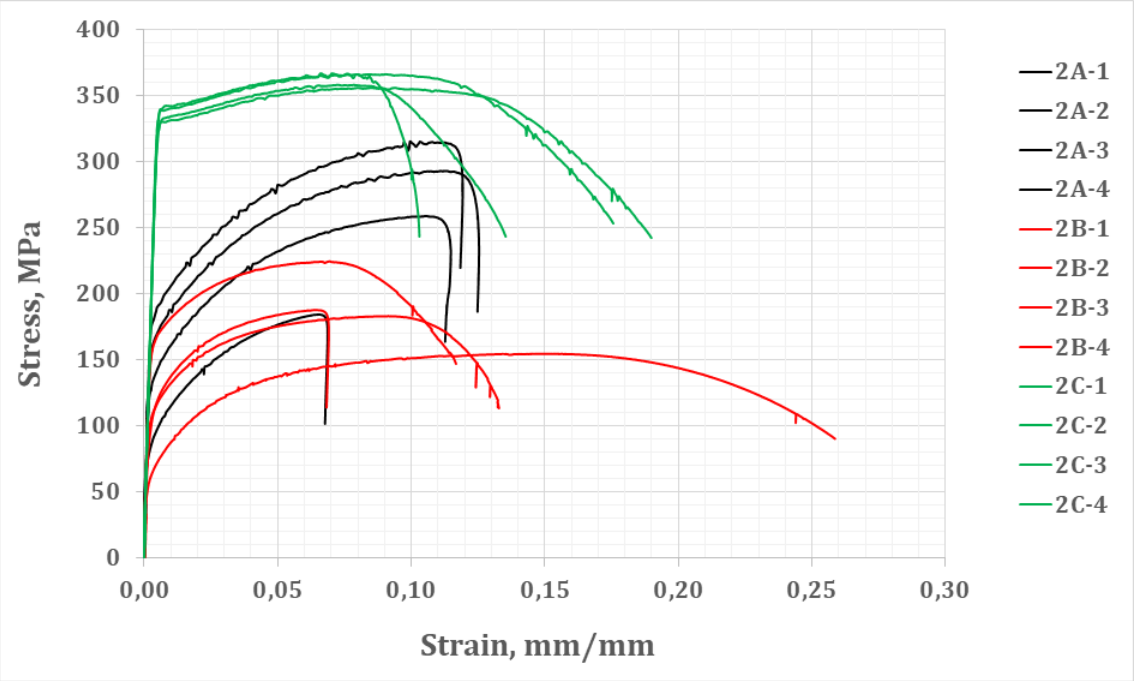

Figure 4.13: Stress-strain curve for SE6082WQ. Black lines represent the as extruded profiles, temper T1. Red lines represent aged to maximum strength, temper T5. Green lines represent the solution heat treated and aged to maximum strength.

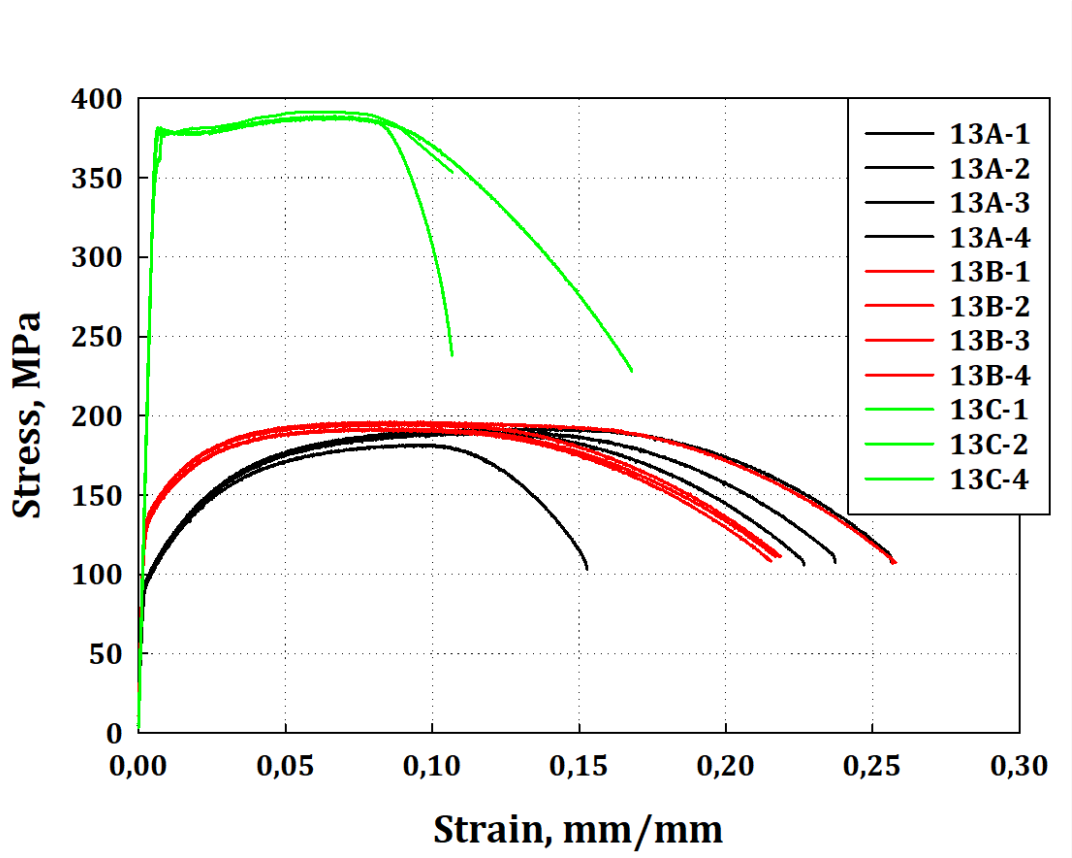

Figure 4.14: Stress-strain curve for RE6082AC. Black lines represent the as extruded profiles, temper T1. Red lines represent aged to maximum strength, temper T5. Green lines represent the solution heat treated and aged to maximum strength.

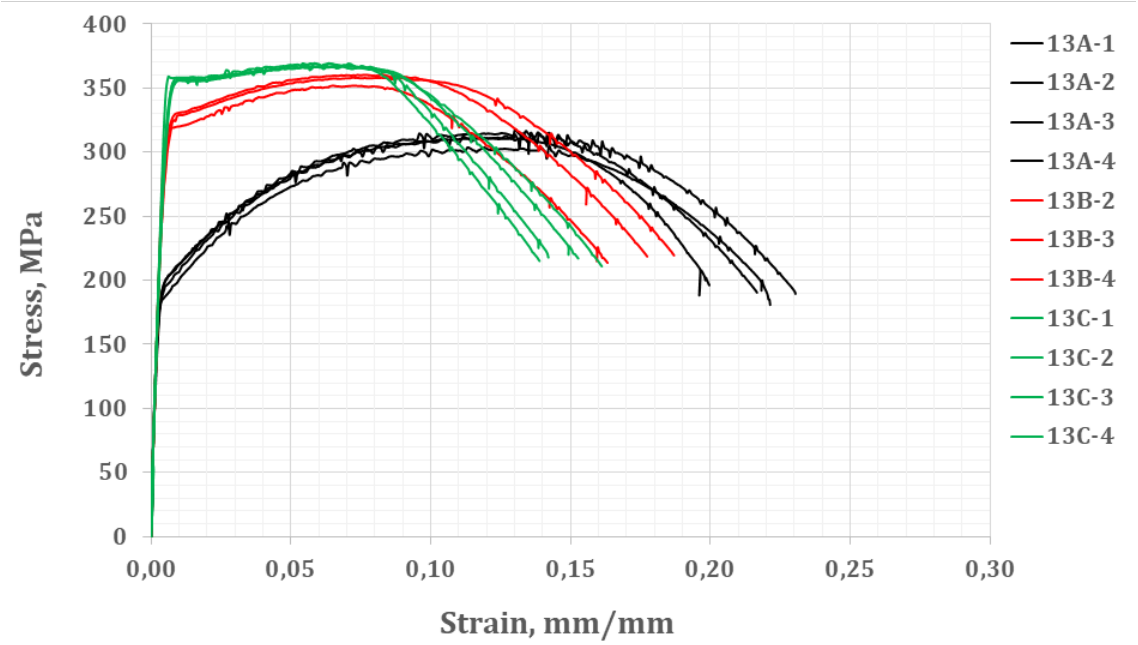

Figure 4.15: Stress-strain curve for RE6082WQ. Black lines represent the as extruded profiles, temper T1. Red lines represent aged to maximum strength, temper T5. Green lines represent the solution heat treated and aged to maximum strength.

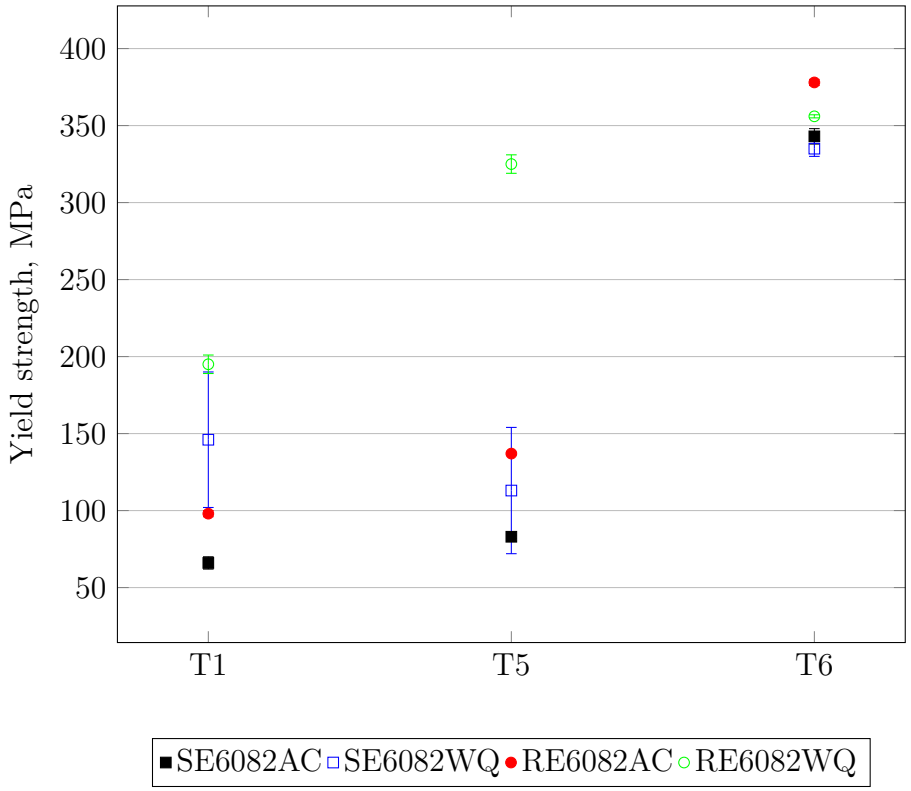

Figure 4.16: Plot of yield strength (σ_y) versus thermal states for 6082 from ram and screw extruded profiles, both air cooled and water quenched.

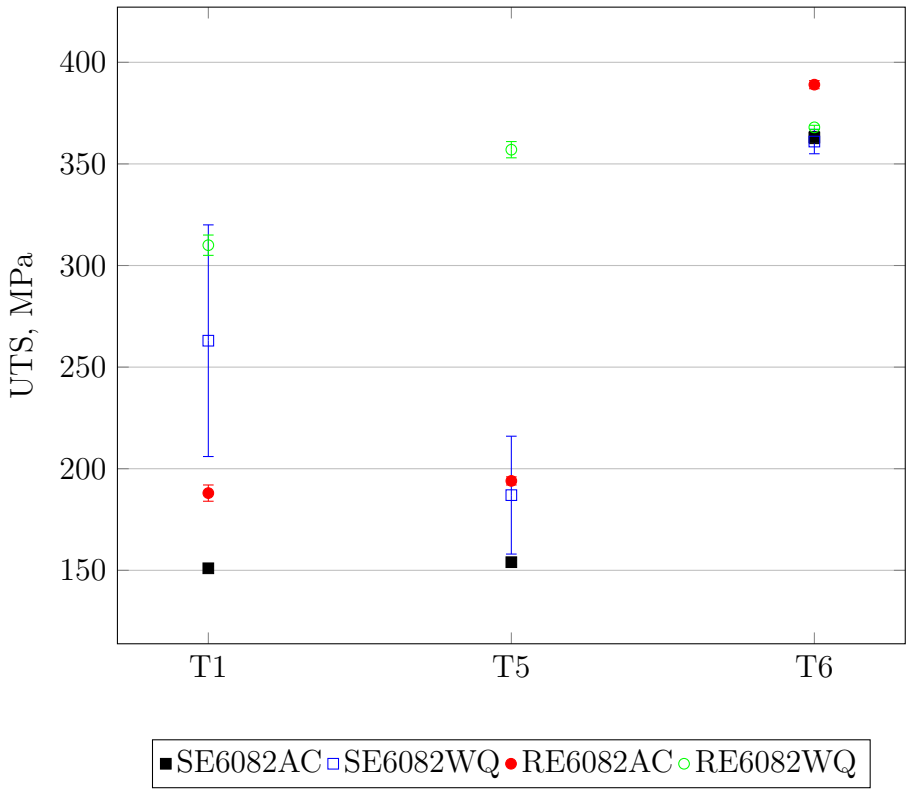

Figure 4.17: Plot of tensile strength (UTS) versus thermal states for 6082 from ram and screw extruded profiles, both air cooled and water quenched.

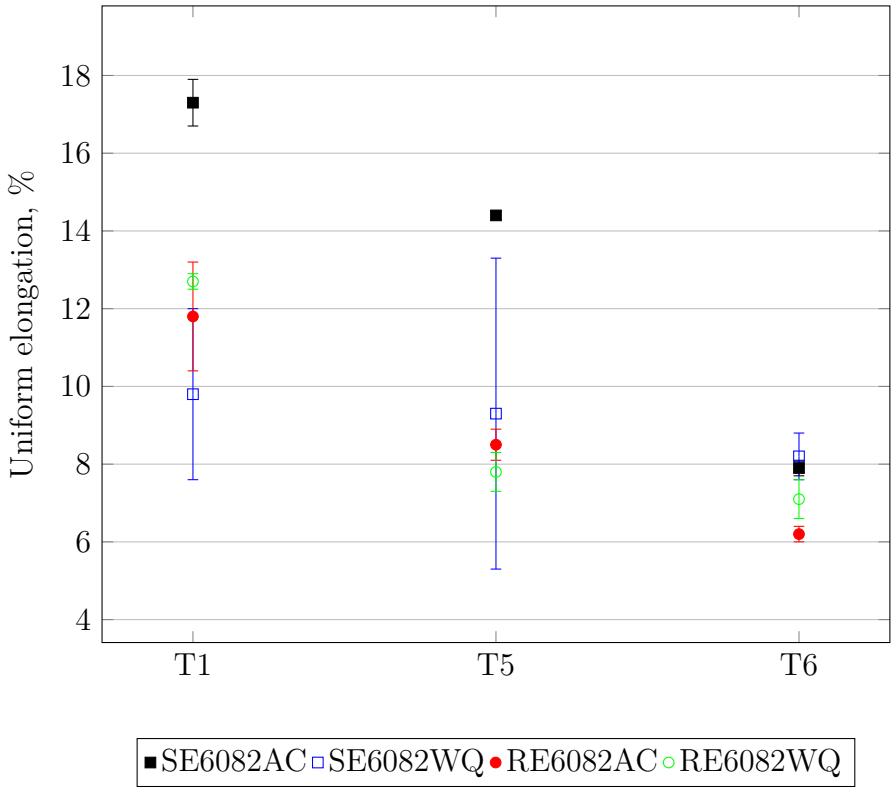

Figure 4.18: Uniform elongation versus thermal states for 6082 from ram and screw extruded profiles, both air cooled and water quenched.

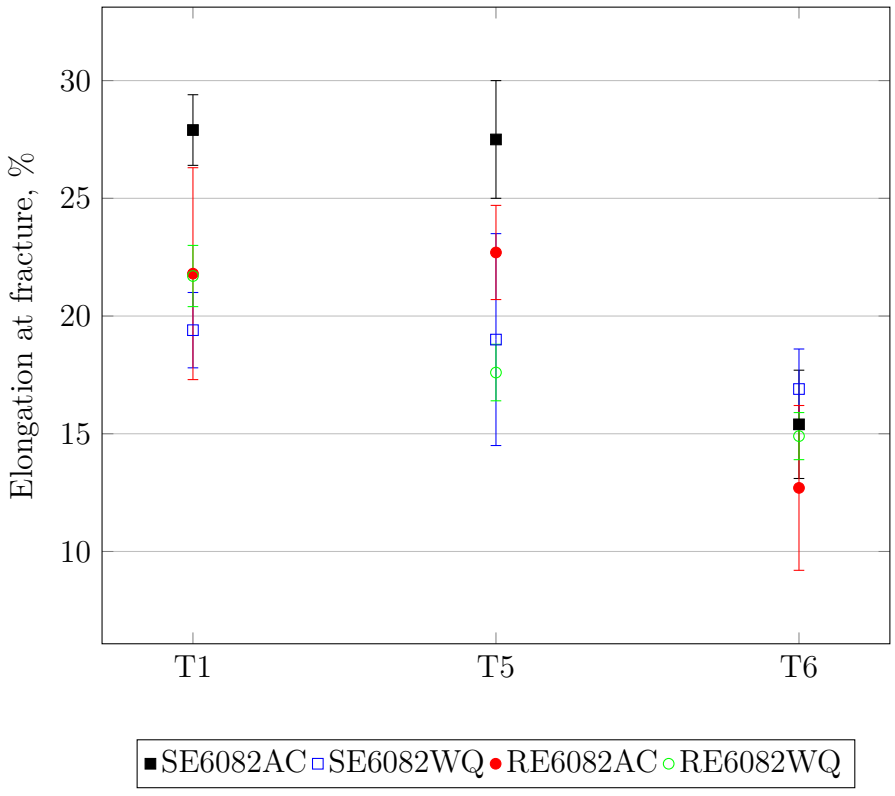

Figure 4.19: Elongation at fracture versus thermal states for 6082 from ram and screw extruded profiles, both air cooled and water quenched.

4.2.2 As extruded microstructure

A fibre structure can be seen in the longitudinal section for all as-extruded 6082 profiles (see Figure 4.20). Ram extruded samples show a zone of recrystallized grains towards the surface. The recrystallized zones were ∼750 µm and 300 µm thick for RE6082AC and RE6082WQ, respectively. Possible cracks appeared near the surface of SE6082AC. It should be noted that each panorama micrograph of the longitudinal section consists of 3-5 micrographs. Thus, the 500 µm scale bar on each micrograph might not be 1:1 ratio in comparison to each other.

In Figure 4.21, the grain structure in the cross section can be seen. As in the longitudinal section there were recrystallized grains with same thickness as previously stated. In SE6082AC and SE6082WQ stripes of possible particles, oxides or cracks start to appear at 550-600 µm from the surface.

In the micrographs of polished microstructure in Figure 4.22, particles appear randomly in the Al-matrix of the screw extruded samples. The ram extruded samples showed particle formation in lines along the extrusion direction (ED).

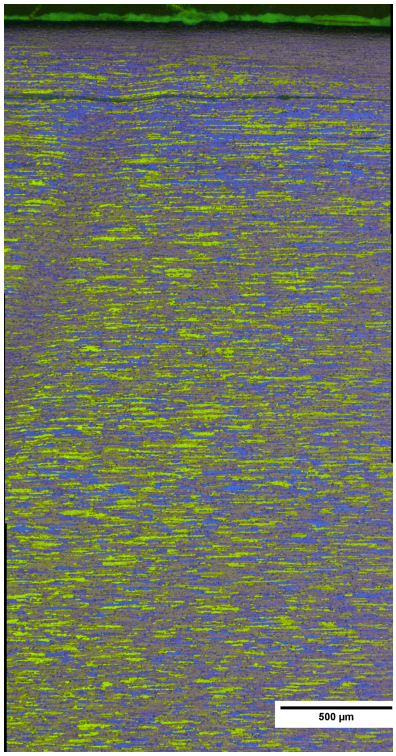

(a) Air cooled

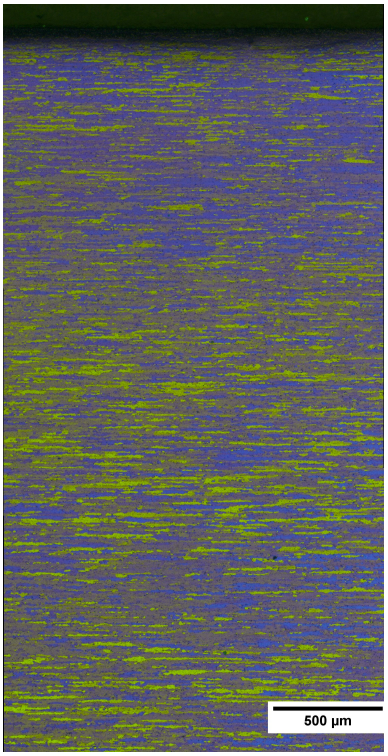

(b) Water quenched

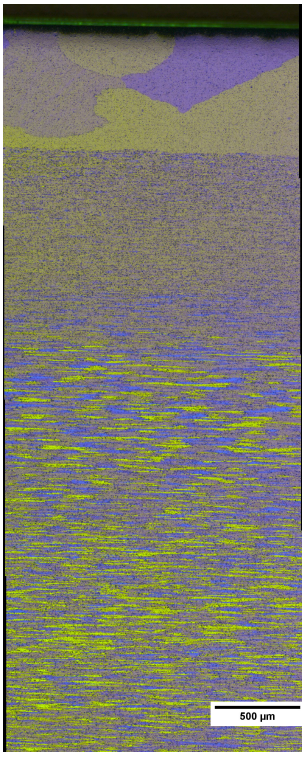

(c) Air cooled

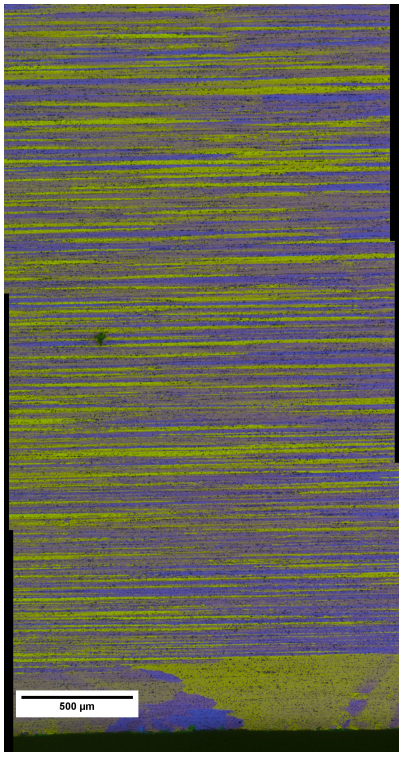

(d) Water quenched

Figure 4.20: Grain structure in the longitudinal section of screw (a and b) and ram (c and d) extruded 6082. ED is to the left.

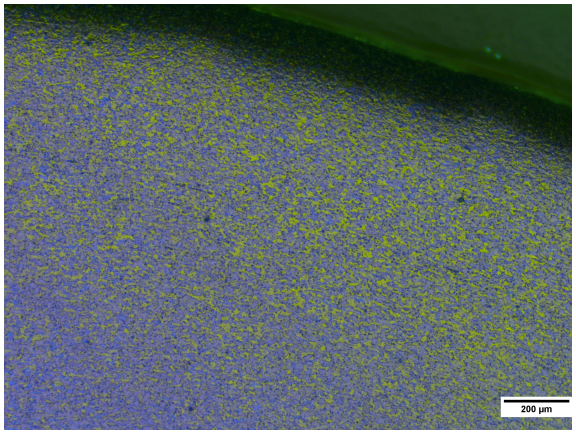

(a) Air cooled

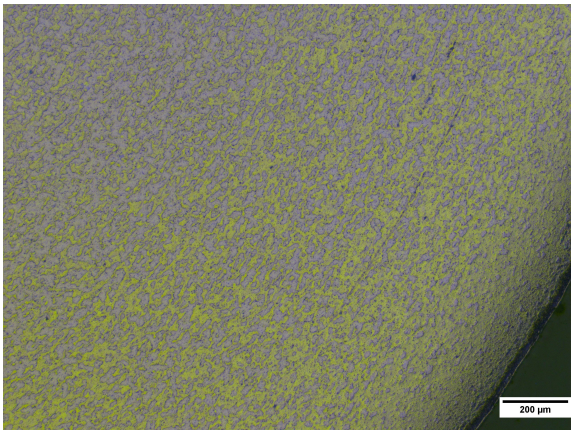

(b) Water quenched

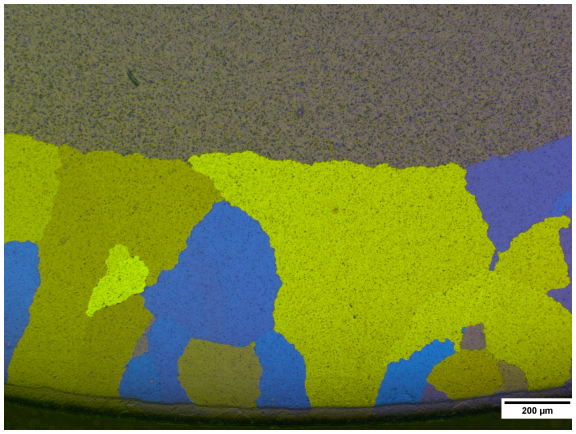

(c) Air cooled

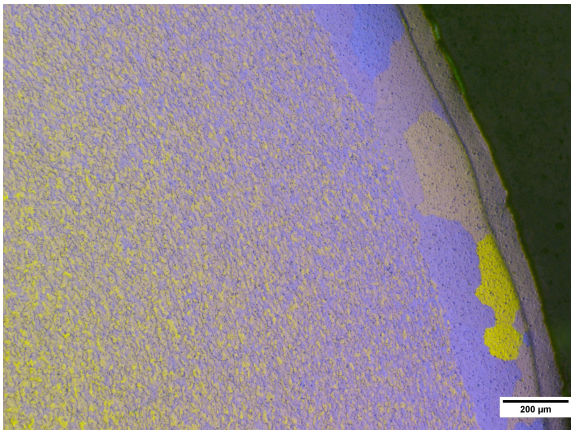

(d) Water quenched

Figure 4.21: Grain structure in the cross section towards the surface of screw (a and b) and ram (c and d) extruded 6082. ED is out of the micrograph.

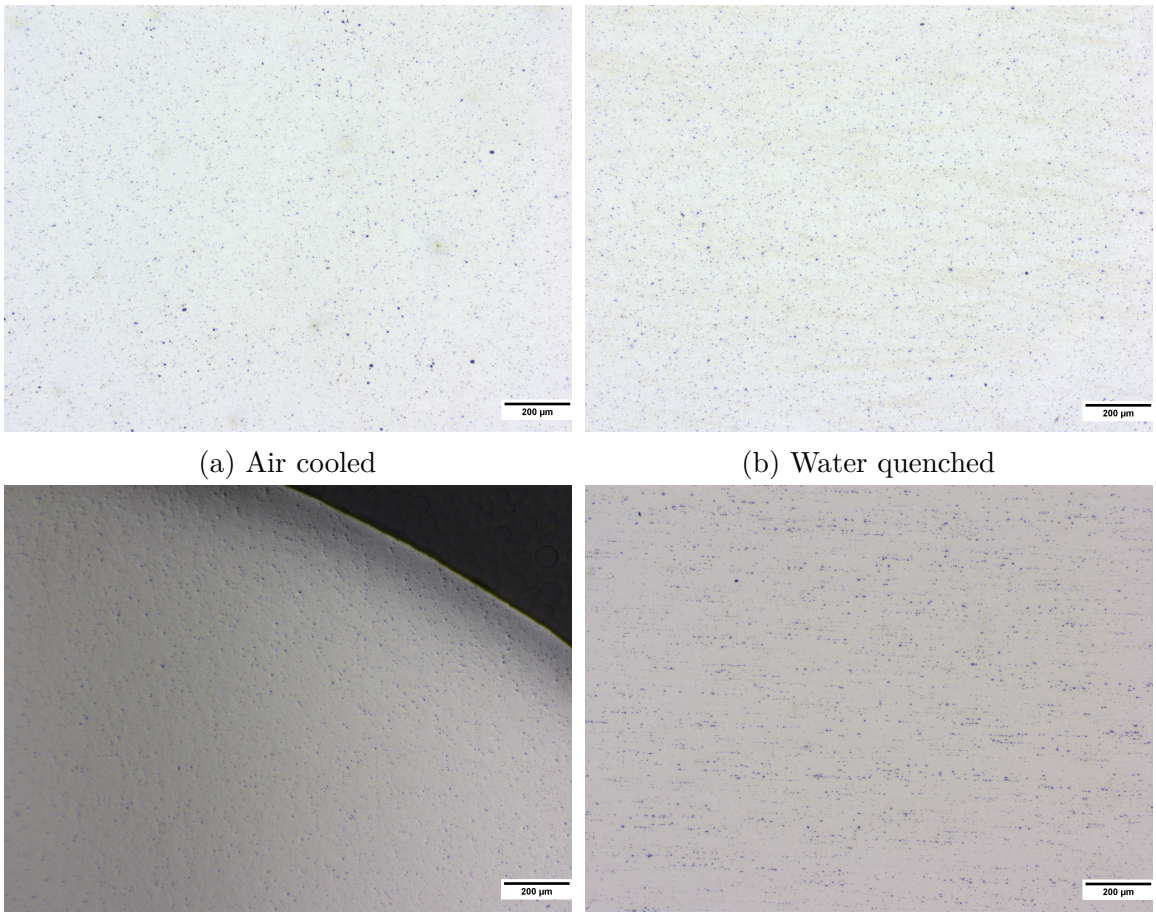

(a) Air cooled (b) Water quenched

(c) Air cooled (d) Water quenched

Figure 4.22: Particle structure in the longitudinal section of screw (a and b) and ram (c and d) extruded 6082. ED is to the left. (c) RE6082AC is seen in the cross section, with ED out of the micrograph.

4.2.3 Solution heat treated microstructure

A fibre structure were still present in screw extruded 6082 profiles (see Figure 4.23). At the surface of SE6082AC, small blisters start appearing. RE6082AC are completely recrystallized through its longitudinal section. Grain growth has occured in the center of the sample. In RE6082WQ the recrystallized zone has grown to 1.35 mm, approximately 1.05 mm thicker than in as-extruded state. Note that each panorama consists of 3 or 4 micrographs, thus the scale bar might not be 1:1 ratio compared to each other.

As seen in the cross section in Figure 4.24, a local appearance of recrystallized grains have appeared at the surface and at random areas within the SE6082AC profile. Additional micrographs of this random recrystallization can be found in Appendix D. Poor contrast differences might suggest low misorientation angles between the fibre grains. Otherwise, these cross sections supports the findings from the panorama micrographs.

The particle structure of SHT SE6082AC sample in Figure 4.25 show distinct stripes along the ED. These stripes are alignments particles and oxides due to the flow through the screw extruder. SE6082WQ show appearances of cracks near the surface. Both ram extruded samples still show the particle formation aligned in the ED.

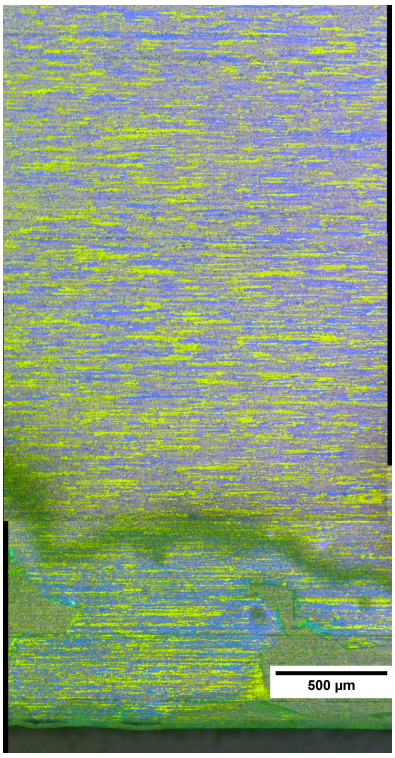

(a) Air cooled.

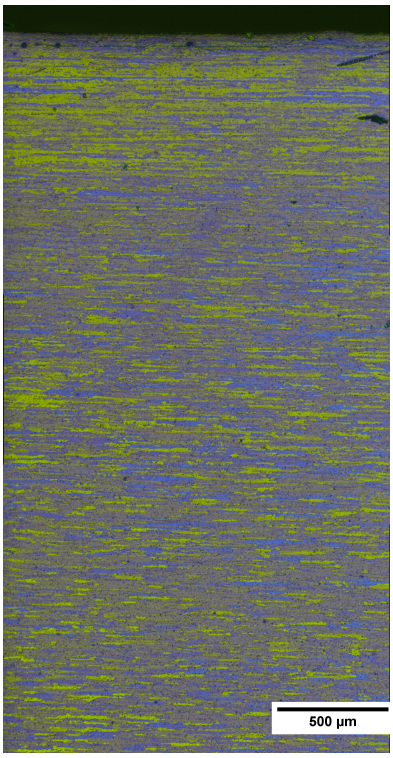

(b) Water quenched.

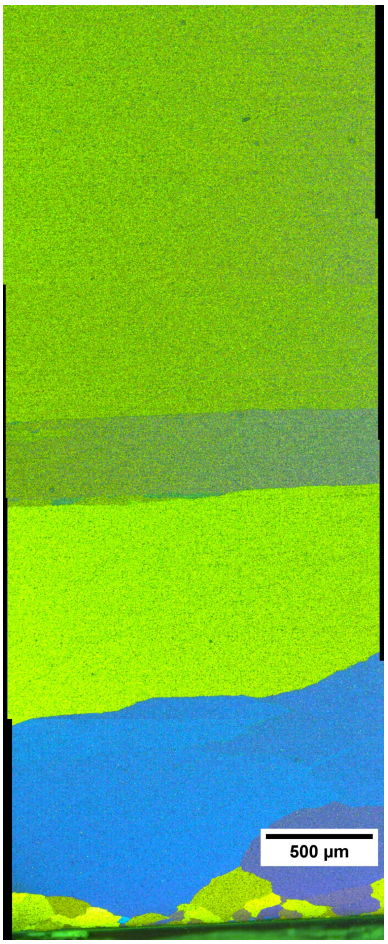

(c) Air cooled.

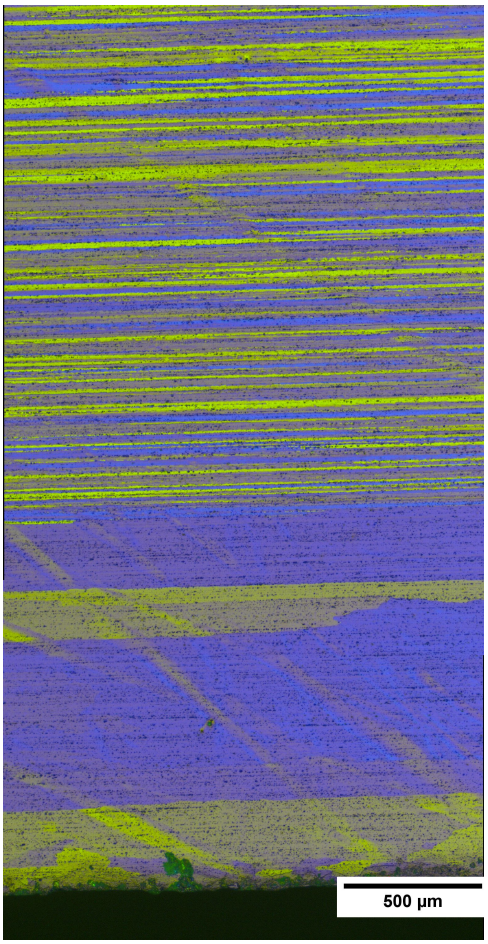

(d) Water quenched.

Figure 4.23: Grain structure in the longitudinal section of SHT 6082 from screw (a and b) and ram (c and d) extrusion. ED is to the left.

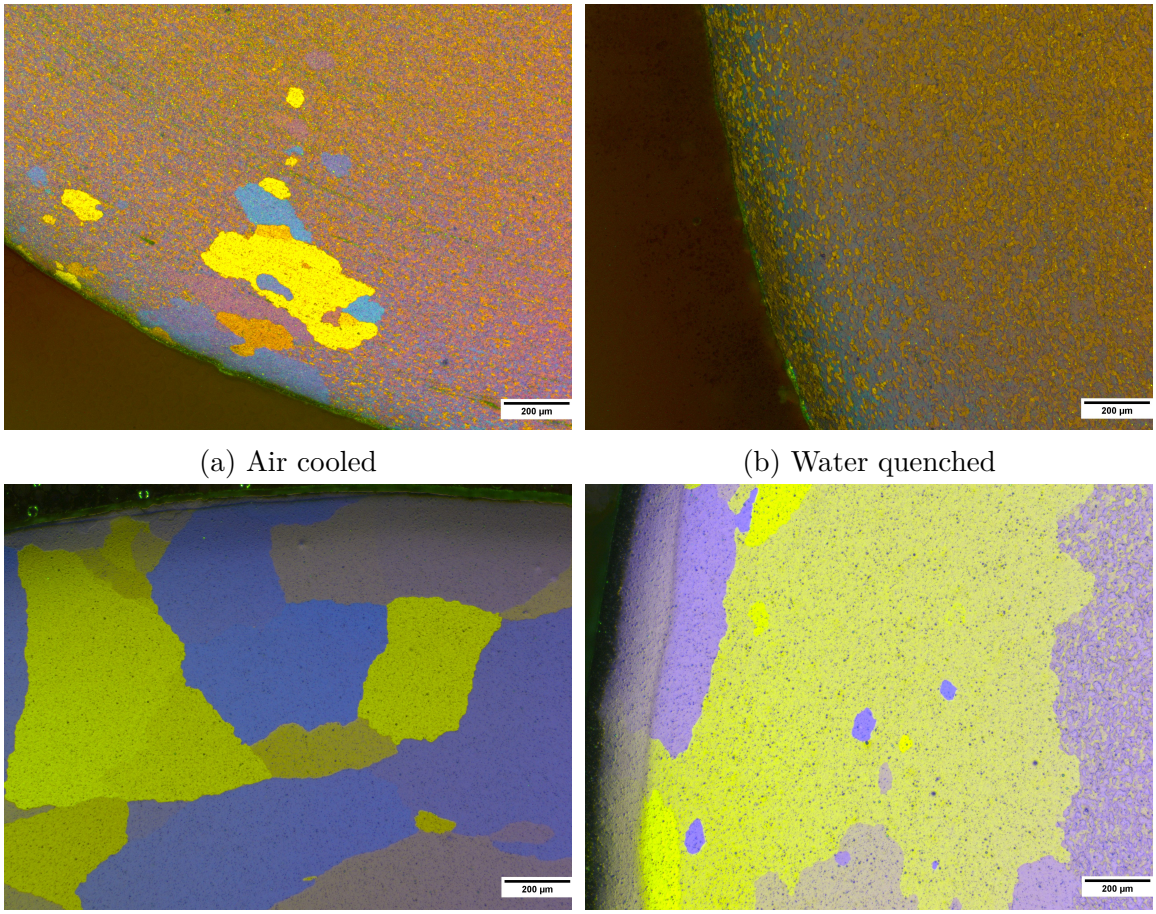

(a) Air cooled

(b) Water quenched

(c) Air cooled

(d) Water quenched

Figure 4.24: Grain structure in the cross section towards the surface of SHT 6082 from screw (a and b) and ram (c and d) extrusion. ED is out of the micrograph.

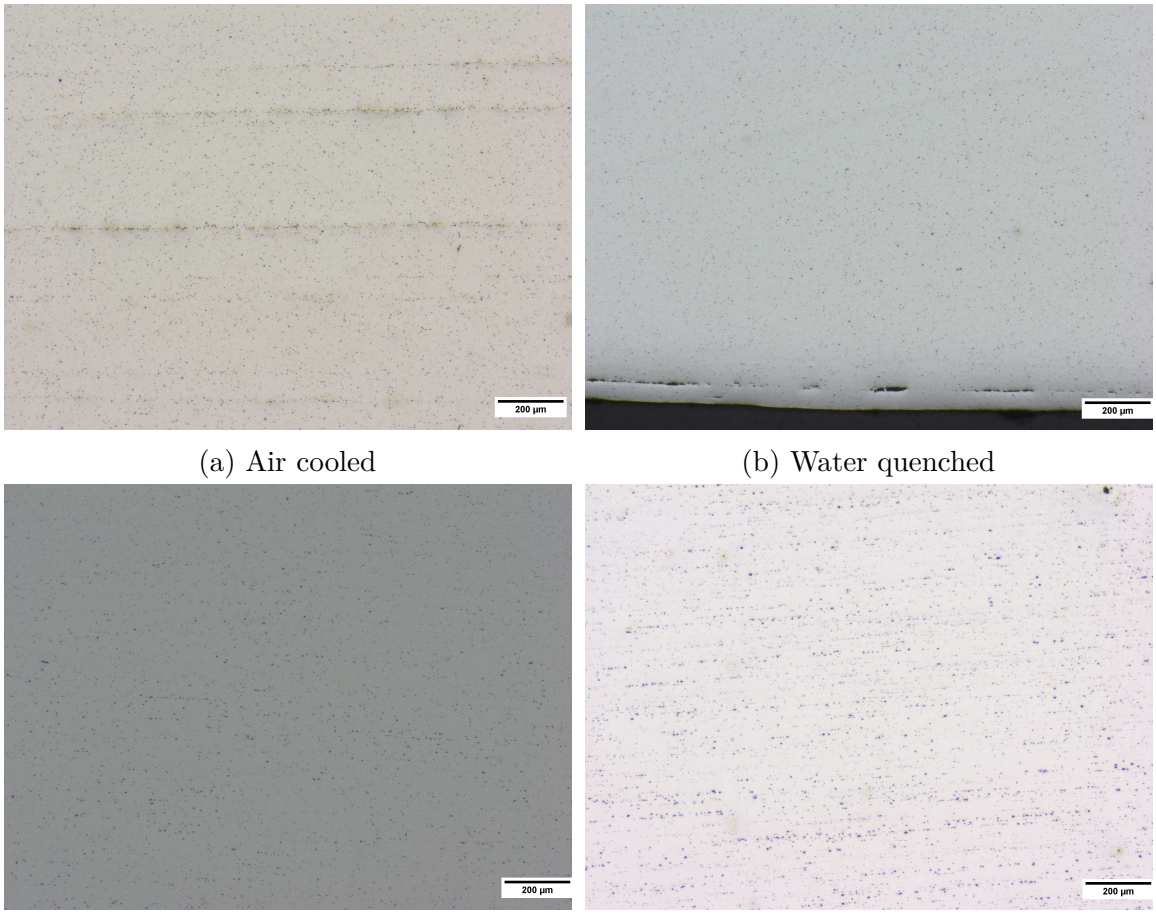

(a) Air cooled

(b) Water quenched

(c) Air cooled

(d) Water quenched

Figure 4.25: Particle structure in the longitudinal section of SHT 6082 from screw (a and b) and ram (c and d) extrusion. ED is left.

4.3 Extruded 6005.40 profiles

In Figure 4.26, the surface quality can be seen for screw extruded profiles. The surface of WQ profiles were smooth as for the ram extruded profiles. The surface of the air cooled on the other hand, had tearing on one side of the surface. Blister also appeared on ∼1m of the surface of SE6005.40AC.

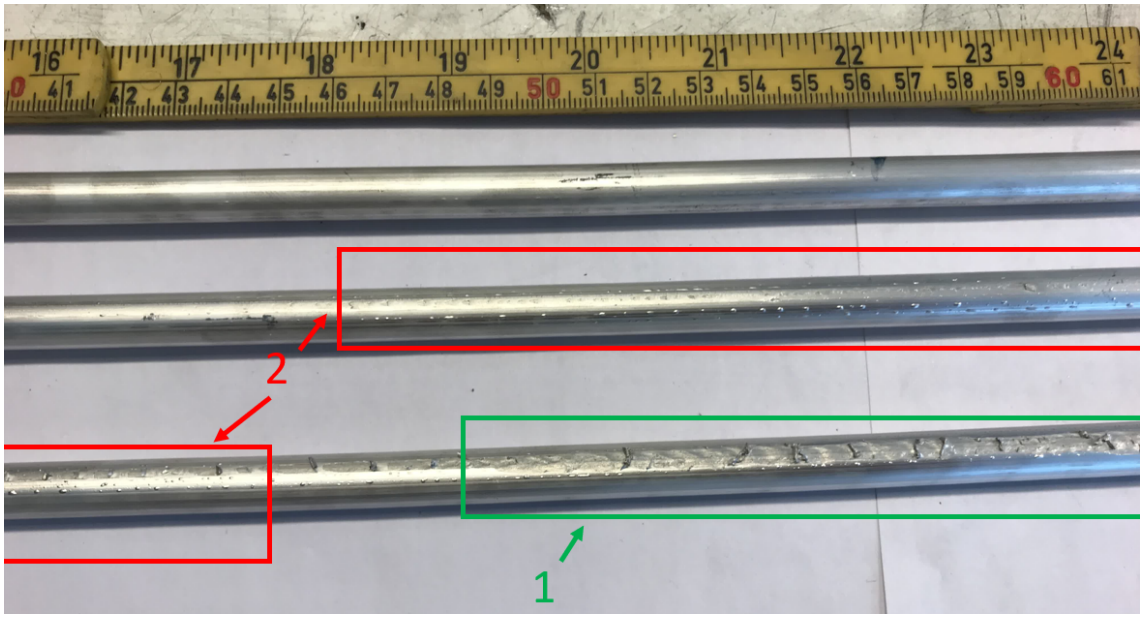

(a) Air cooled.

(b) Water quenched.

Figure 4.26: Screw extruded 6005.40 profiles. (a) blistering (1) and tearing (2) on the air cooled profiles. The water quenched profiles have a smooth surface.

The extrusion speed were split into air cooled sections and the last water quenched section, see Table 4.5. AC1 represents the extrusion speed for the first length af-

ter breakthrough. AC2 represents the start of unstable temperature control, and an increase in extrusion speed. AC1 were steady state extruded with good control over temperatures in the screw. AC2 were mostly steady state extruded, but ocassionally with some pushes. WQ were extruded with instability of the torque, and subtle changes in temperature. The resulting extrusion speed were on average approximately the same for AC and WQ at $\sim 0.144\,\mathrm{m\,min^{-1}}$. In comparison, the ram extrusion had an extrusion speed ∼254 times faster than the screw extrusion.

Table 4.5: Average extrusion speed for screw extruded 6005.40 profiles. Calculated from input mass difference and the given time intervals. 1 m corresponds to 212g of input material with a Ø10mm die orifice. Last column is the extrusion speed during the ram extrusion for comparison, from experiment nr. 14 in Appendix C.

	AC1	AC2	WQ	RE
Time interval [m/min]	34-52	52-65	65-87	N/A
Δ Mass [g]	530	390	660	N/A
Speed [m/min]	0.141	0.144	0.144	36.6

4.3.1 Mechanical properties & electrical conductivity

The hardness evolution of the extruded profiles were determined for as-extruded and solution heat treated samples. WQ samples from both screw and ram extrusion is shown to have better hardness than for AC. SE6005.40WQ resembles RE6005.40AC in terms of electrical conductivity. Temper T1 values in Figure 4.27 and 4.28 representing the properties as extruded without artificial aging, were shown at point 0.1 on the log time-axis.

SHT samples shows the hardness of all four parallels (i.e. SE-AC, RE-WQ etc.) to be similar and with less deviation than for directly aged. This is also seen in the conductivity. Temper T4 values in Figure 4.29 and 4.30 representing the properties as solution heat treated, without artificial aging, are shown at point 0.1 on the log time-axis.

To check if the differences in hardness at temper T1, T5 and T6 translates to the strength, nominal stress-strain curves are shown in Figure 4.31-4.34. As seen in these stress-strain curves, the fracture strain appeared outside of the extensometer for some tensile tests giving invalid results. These fracture strains (Figure 4.38) were therefore calculated from the actuator movement, assuming all samples had a length of 30 mm between the shoulders as per the dimensional drawing in Figure 3.7, Section 3.6.2. However, even though RE6005.40AC-T5 (red lines) looks as if fracture happened outside of the extensometer, the actuator movement suggested that these strains were correct. Visual inspection of these tensile specimen will be discussed in Section 5.2.6.

In general for all parallels, the T1 specimens experiences extensive work hardening. Work hardening of temper T5 and T6 were considerable less. Black lines represent the as extruded temper T1 after natural aging of approximately 4 weeks (through machining). Red lines represent the aged to maximum hardness temper T5. Green lines represent the solution heat treated and aged to maximum hardness temper T6.

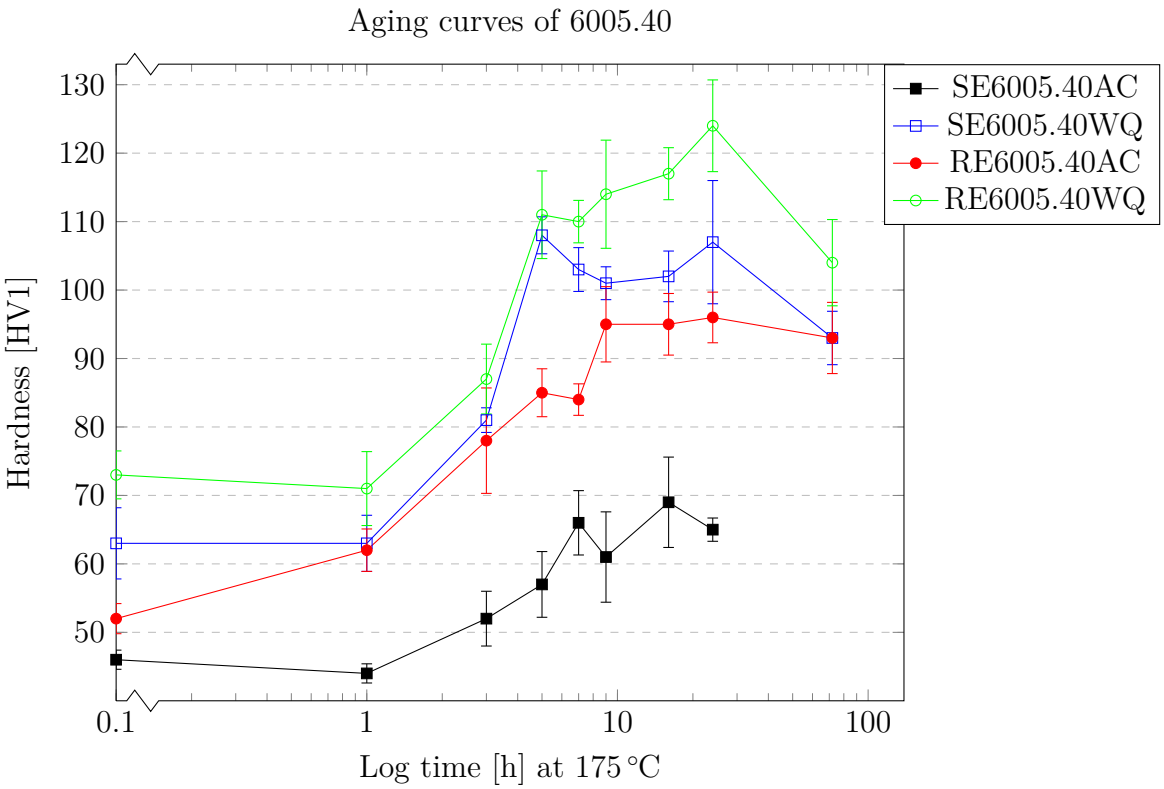

Figure 4.27: Hardness evolution with aging time at 175 °C for 6005.40 from ram and screw extruded profiles, both air cooled and water quenched.

The main findings from the tensile tests, such as UTS, YS, uniform elongation and elongation at fracture, were collected from each stress-strain curve and presented in Figure 4.35-4.38.

Yield strength of all parallels at each tempers seem to be relatively similar, except for SE6005.40AC with considerable lower values at temper T1 and T5. UTS values appear with a similar pattern. The ductility of these parallels show that at temper T1 and T6 screw extruded specimens exhibit lower values than ram extruded, but slightly higher for temper T5. SE6005.40WQ exhibit relatively large deviation in all values, excluding YS and UTS at temper T6.

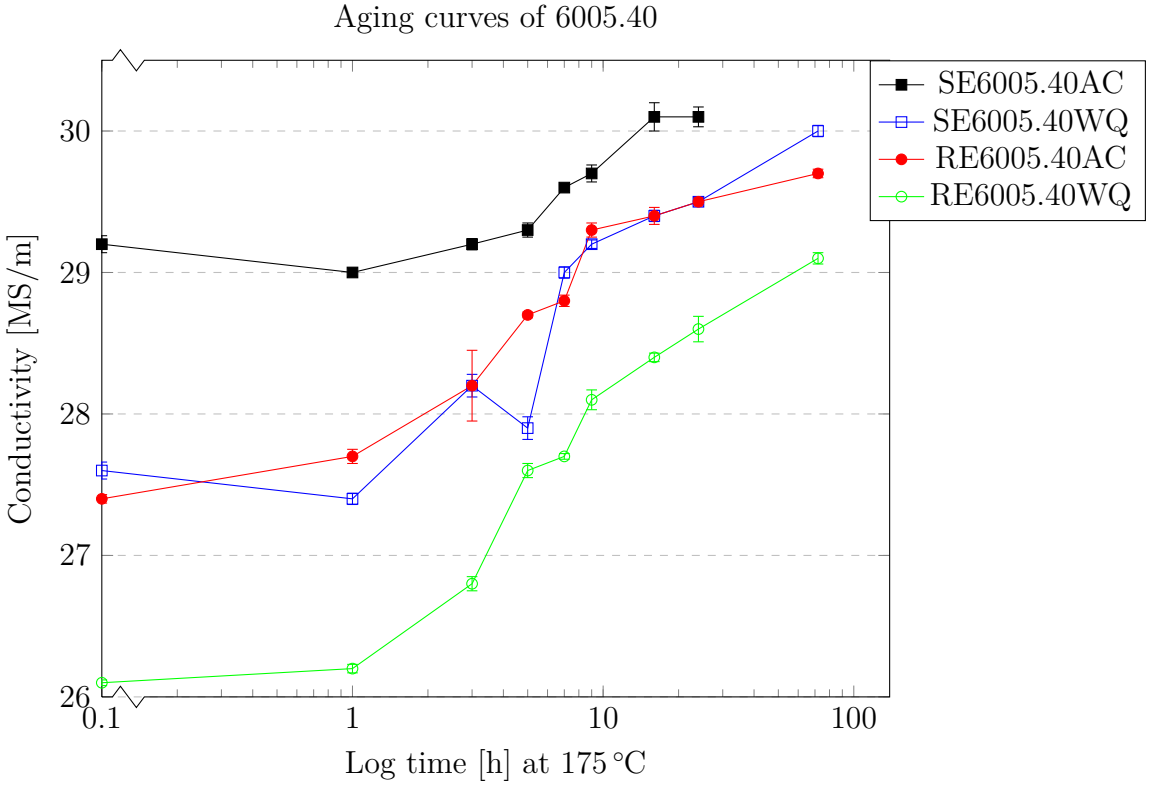

Figure 4.28: Electrical conductivity evolution with aging time at 175 °C for 6005.40 from ram and screw extruded profiles, both air cooled and water quenched.

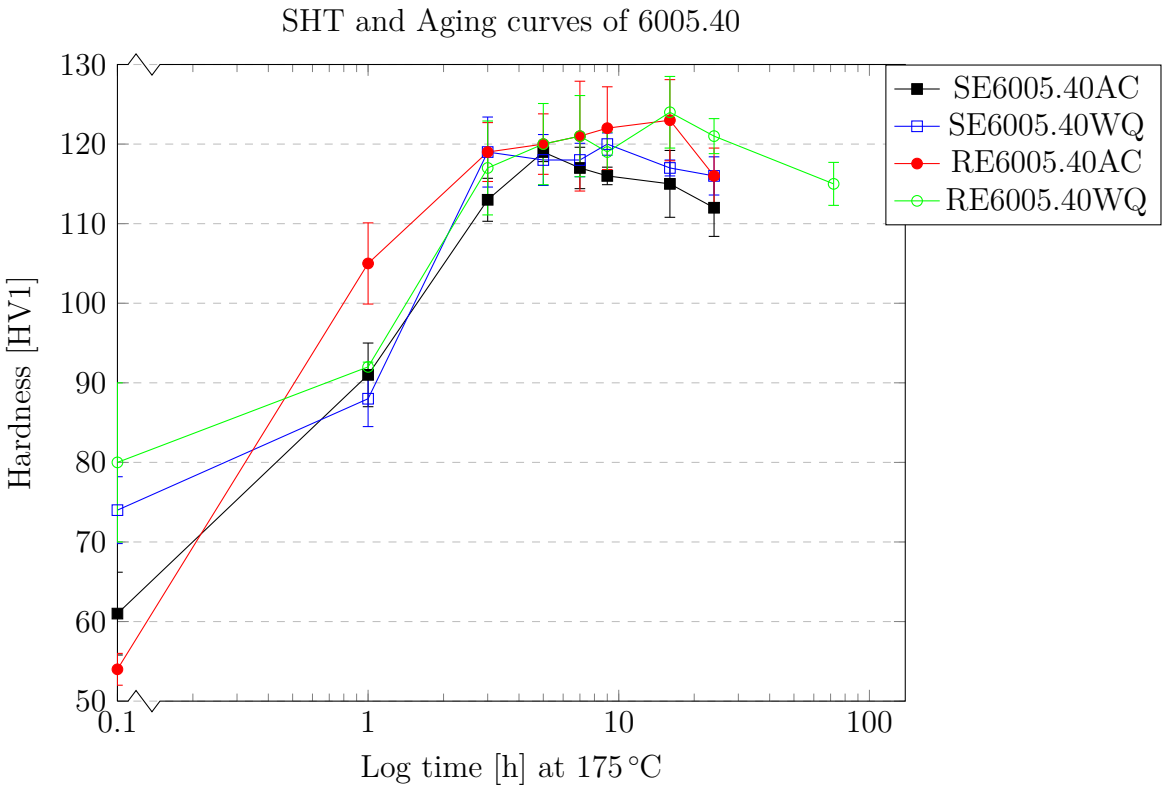

Figure 4.29: Hardness evolution with aging time at 175 °C in SHT 6005.40 for ram and screw extruded profiles, both air cooled and water quenched.

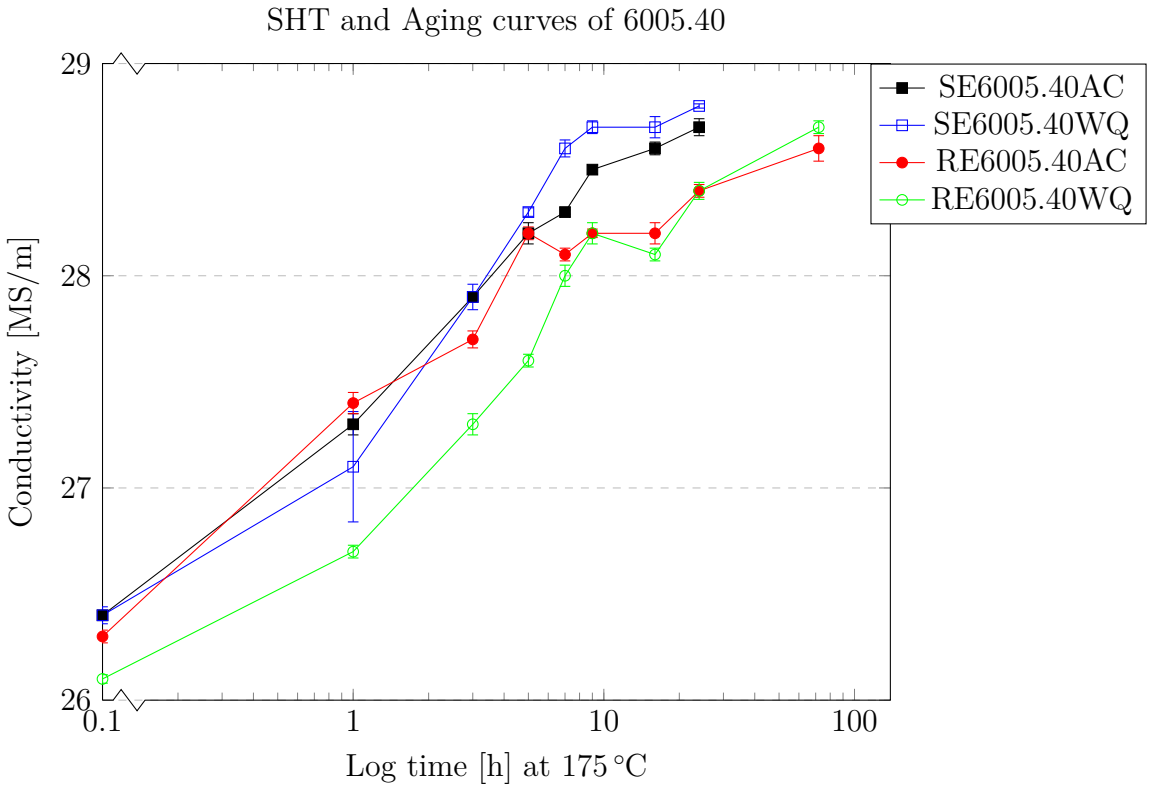

Figure 4.30: Electrical conductivity evolution with aging time at 175 °C in SHT 6005.40 for ram and screw extruded profiles, both air cooled and water quenched.

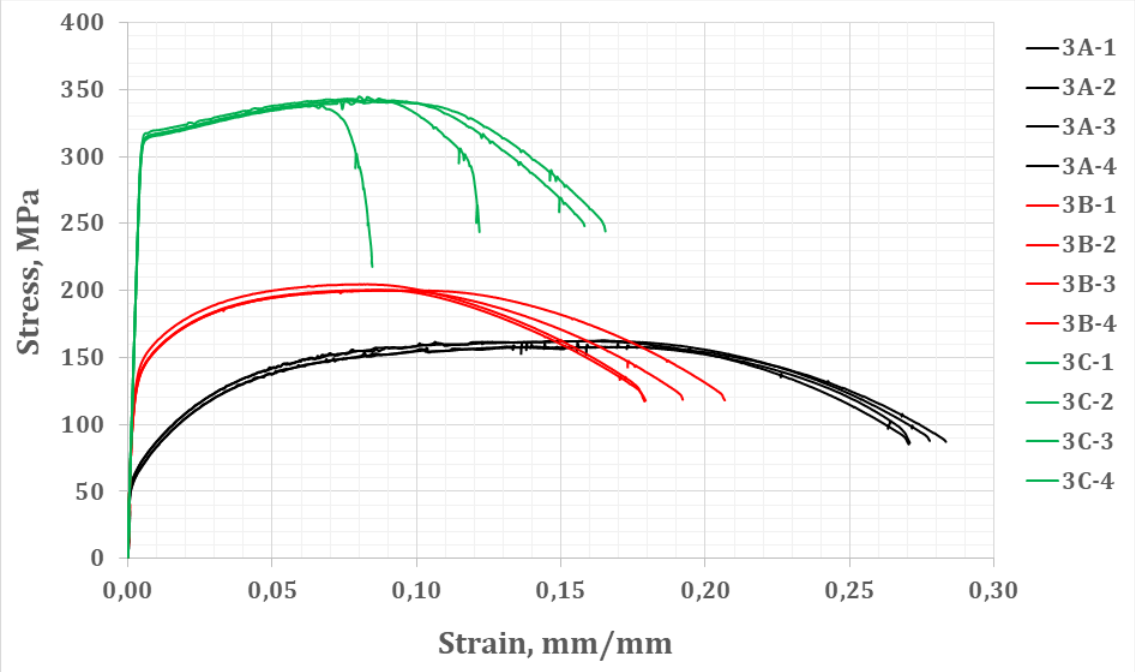

Figure 4.31: Stress-strain curve for SE6005.40AC. Black lines represent the as extruded profiles, temper T1. Red lines represent aged to maximum strength, temper T5. Green lines represent the solution heat treated and aged to maximum strength.

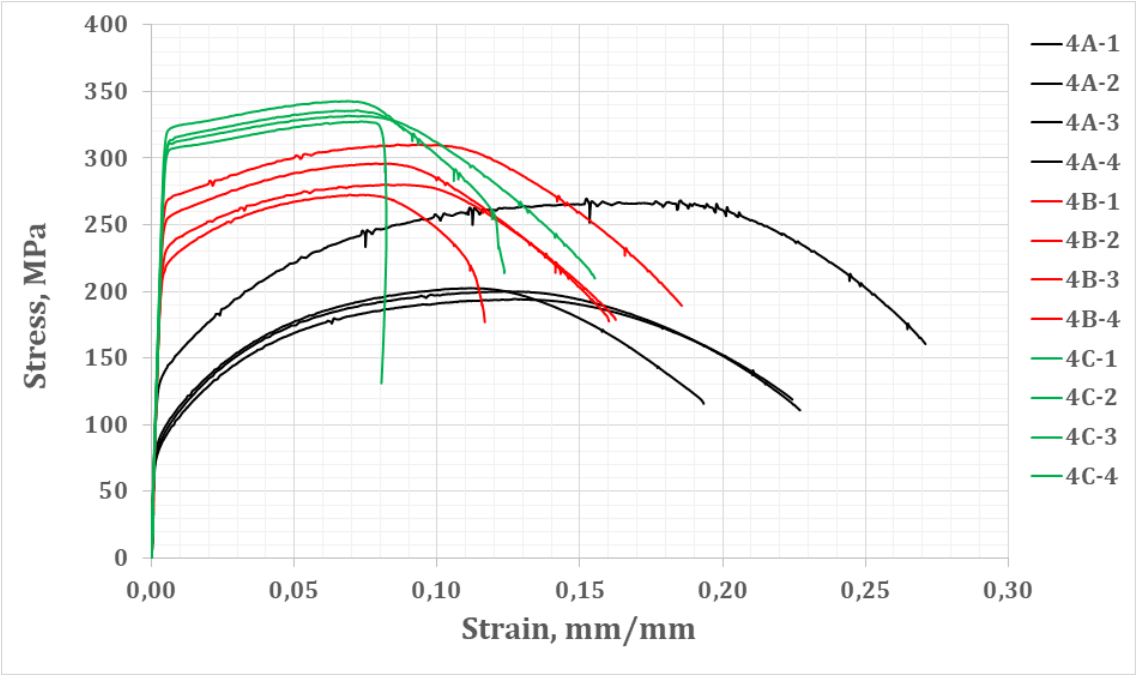

Figure 4.32: Stress-strain curve for SE6005.40WQ. Black lines represent the as extruded profiles, temper T1. Red lines represent aged to maximum strength, temper T5. Green lines represent the solution heat treated and aged to maximum strength.

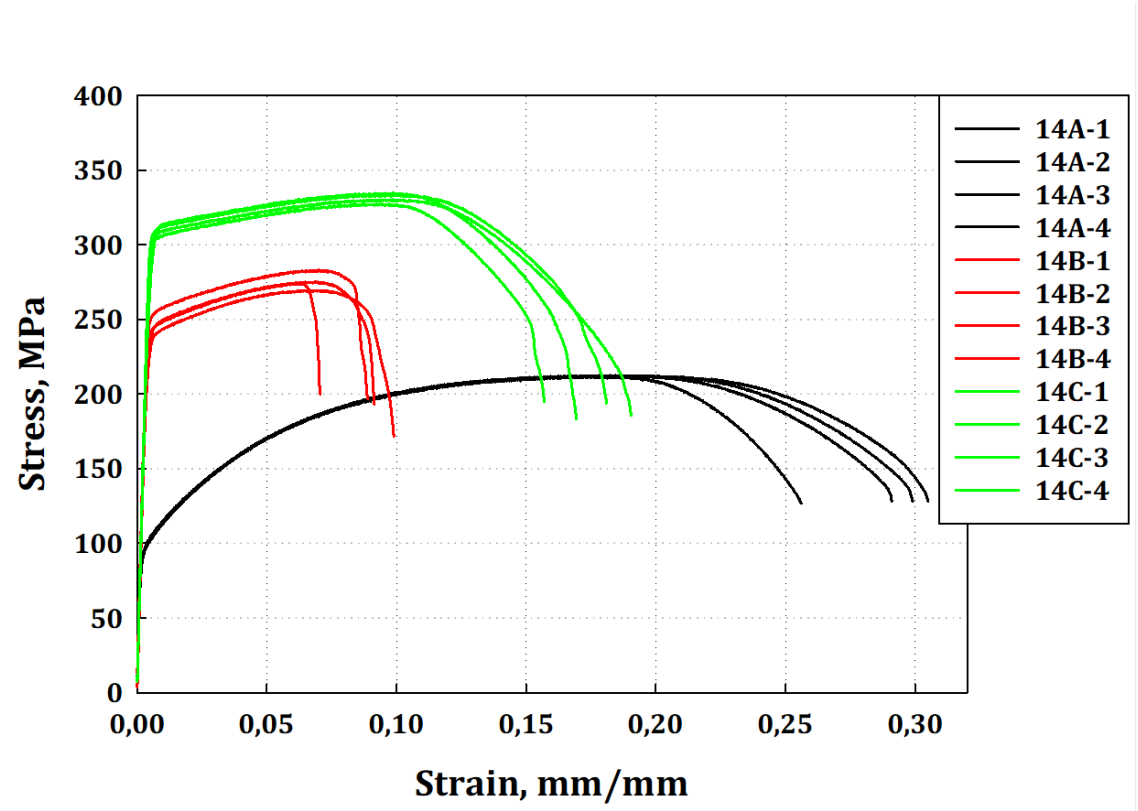

Figure 4.33: Stress-strain curve for RE6005.40AC. Black lines represent the as extruded profiles, temper T1. Red lines represent aged to maximum strength, temper T5. Green lines represent the solution heat treated and aged to maximum strength.

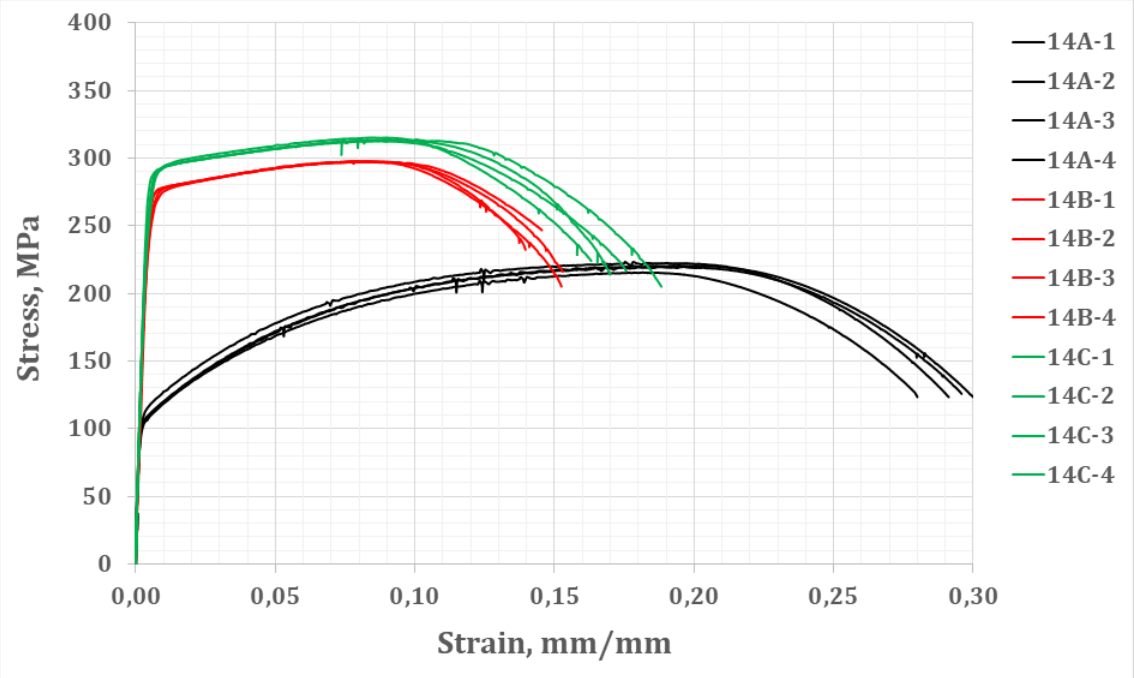

Figure 4.34: Stress-strain curve for RE6005.40WQ. Black lines represent the as extruded profiles, temper T1. Red lines represent aged to maximum strength, temper T5. Green lines represent the solution heat treated and aged to maximum strength.

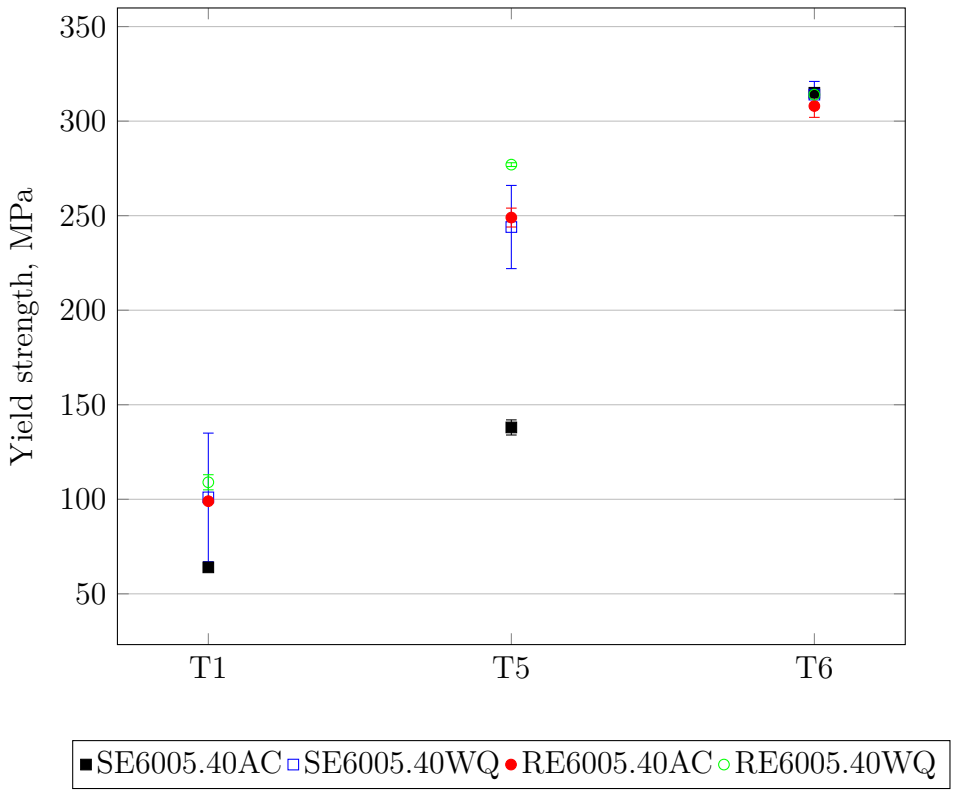

Figure 4.35: Plot of yield strength versus thermal states for 6005.40 from ram and screw extruded profiles, both air cooled and water quenched.

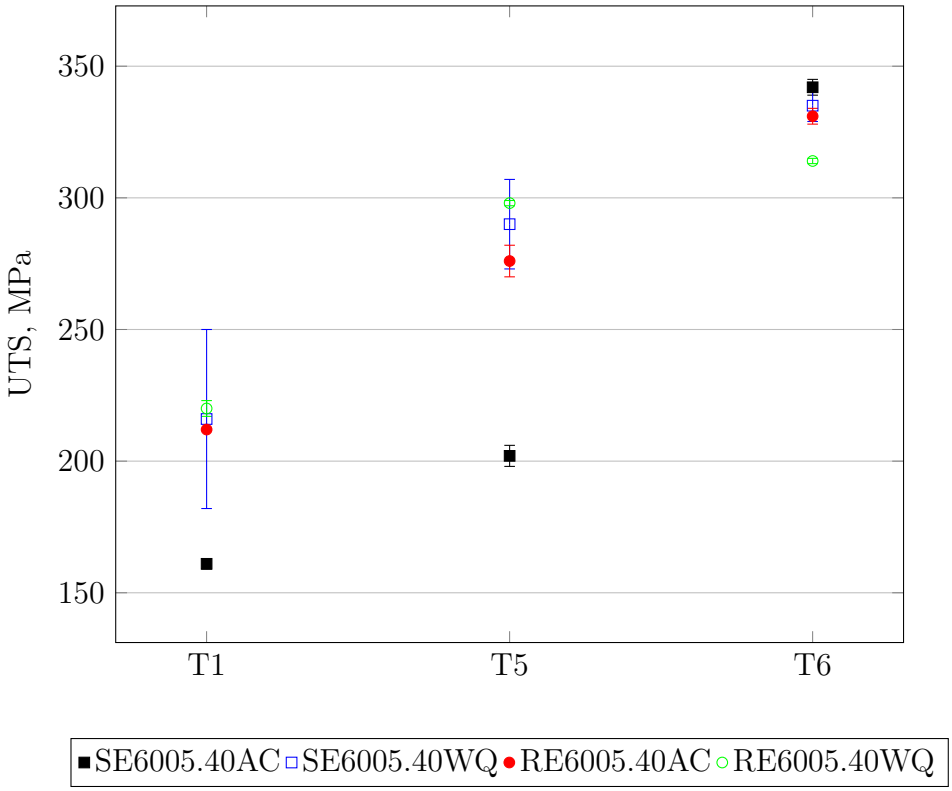

Figure 4.36: Plot of tensile strength (UTS) versus thermal states for 6005.40 from ram and screw extruded profiles, both air cooled and water quenched.

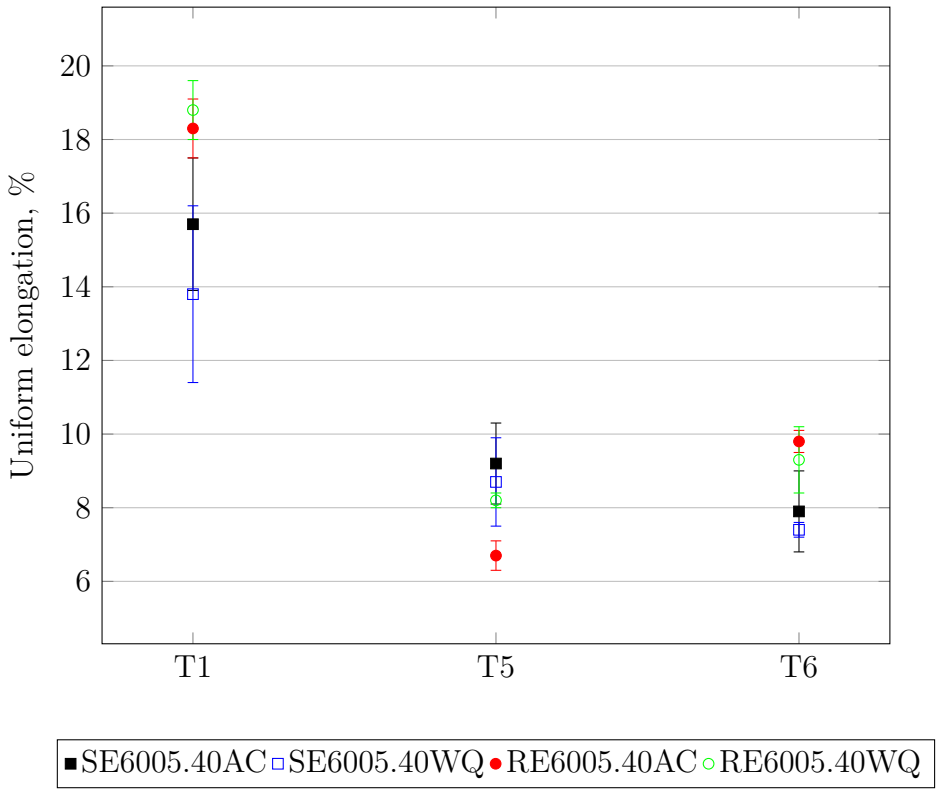

Figure 4.37: Uniform elongation versus thermal states for 6005.40 from ram and screw extruded profiles, both air cooled and water quenched.

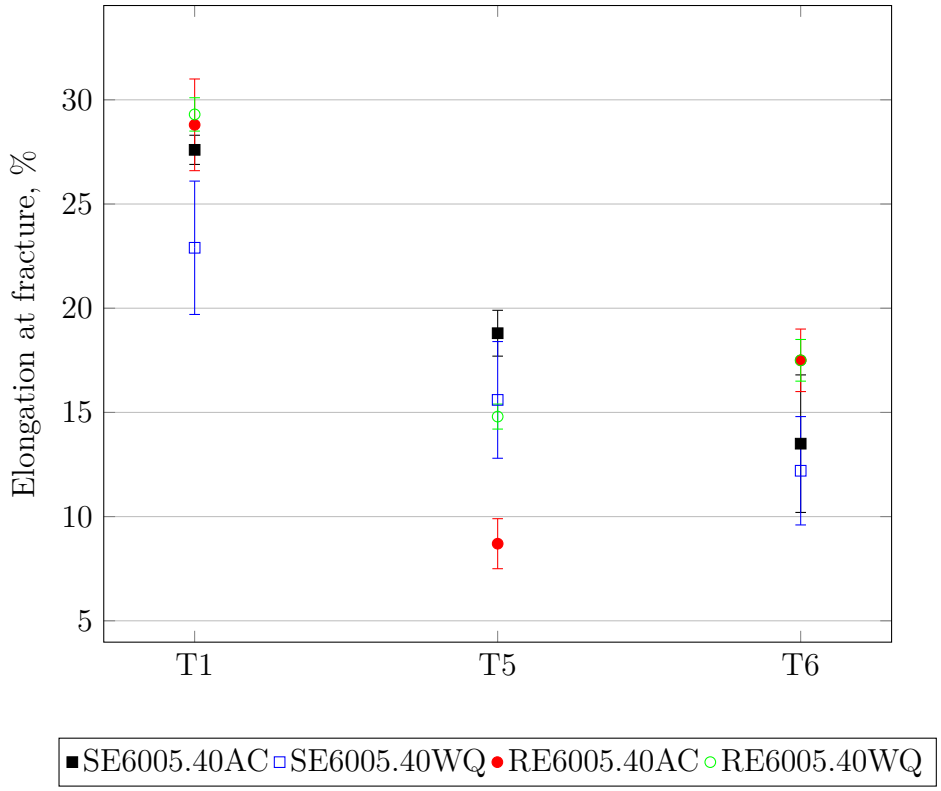

Figure 4.38: Elongation at fracture versus thermal states for 6005.40 from ram and screw extruded profiles, both air cooled and water quenched.

4.3.2 As extruded microstructure

A fibre structure can be seen in the longitudinal section for both as screw extruded profiles (see Figure 4.39). Ram extruded samples show recrystallized grains through its longitudinal section. The recrystallized grains were considerably larger in the intermediate radius and center of the section. Possible crack appeared near the surface of SE6005.40AC. Note that each panorama micrograph of the longitudinal section consists of 3-5 micrographs. Thus, the 500 µm scale bar on each micrograph might not be 1:1 ratio in comparison to each other.

The grain structure in the cross section can be seen in Figure 4.40. As in the longitudinal section, there were smaller recrystallized grains at the surface. The curve in RE6005.40AC is a result of the thermocouple used during extrusion. Both screw extruded samples have vague contrast differences, possibly due to low misorientation angles.

In the micrographs of polished microstructure in Figure 4.41, particles appear randomly in the Al-matrix. The ram extruded samples showed a tendency of particle formation in along the extrusion direction (ED).

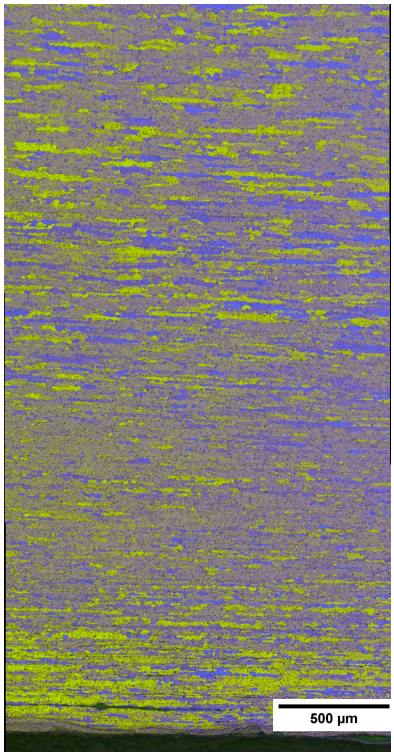

(a) Air cooled

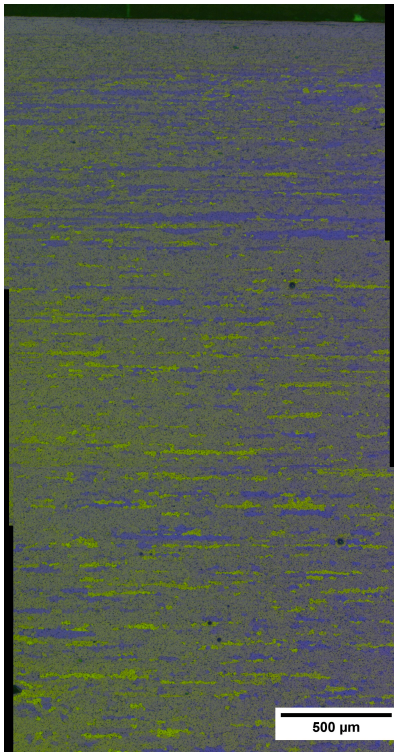

(b) Water quenched

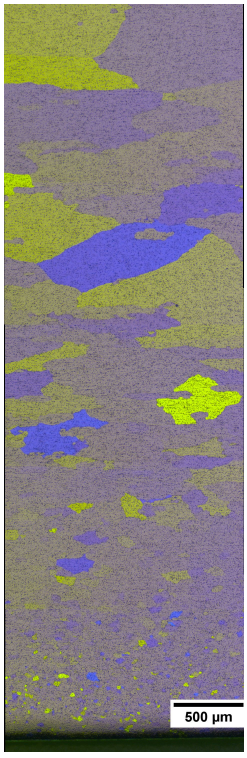

(c) Air cooled

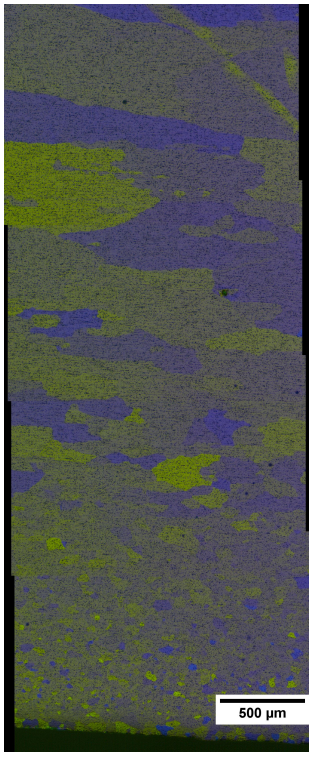

(d) Water quenched

Figure 4.39: Grain structure in the longitudinal section of screw (a and b) and ram (c and d) extruded 6005.40. ED is left.

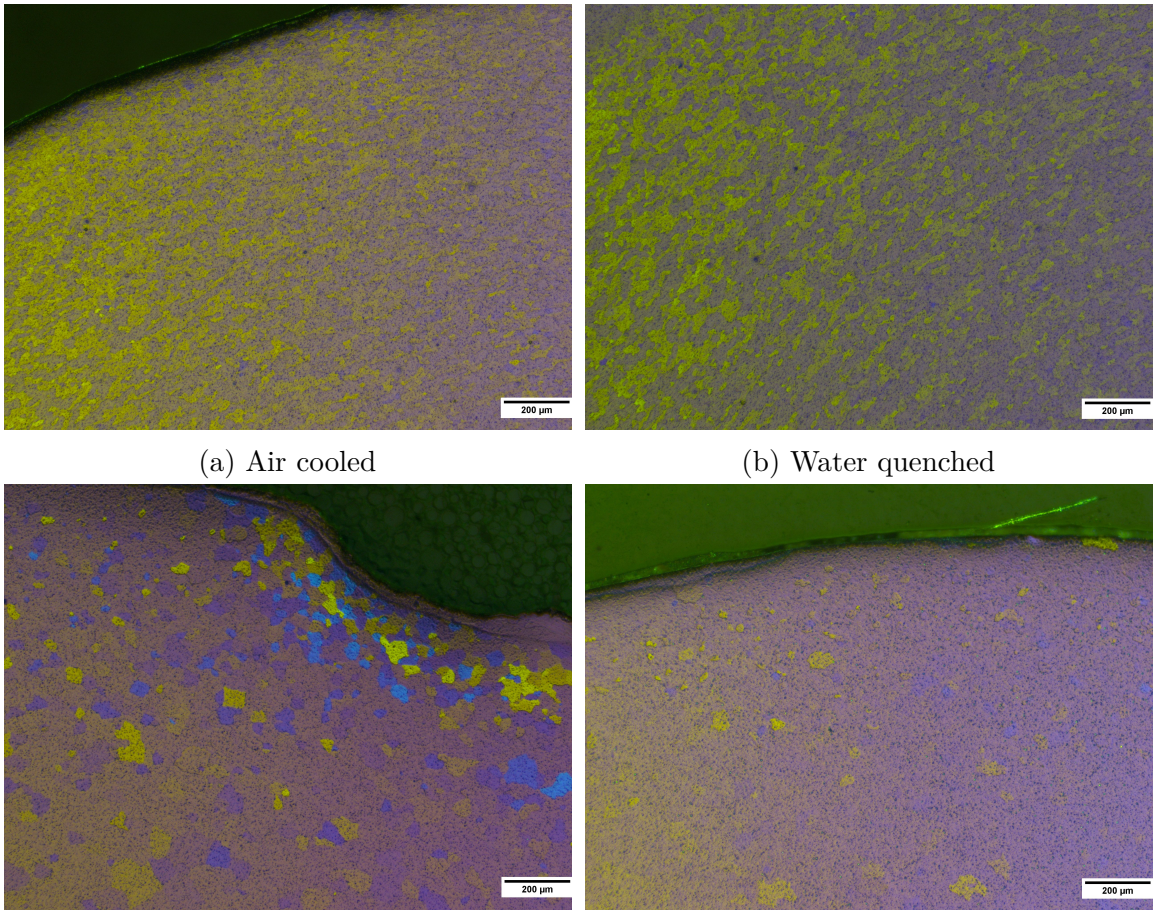

(a) Air cooled

(b) Water quenched

(c) Air cooled

(d) Water quenched

Figure 4.40: Grain structure in the cross section towards the surface of screw (a and b) and ram (c and d) extruded 6005.40. ED is out of micrograph.

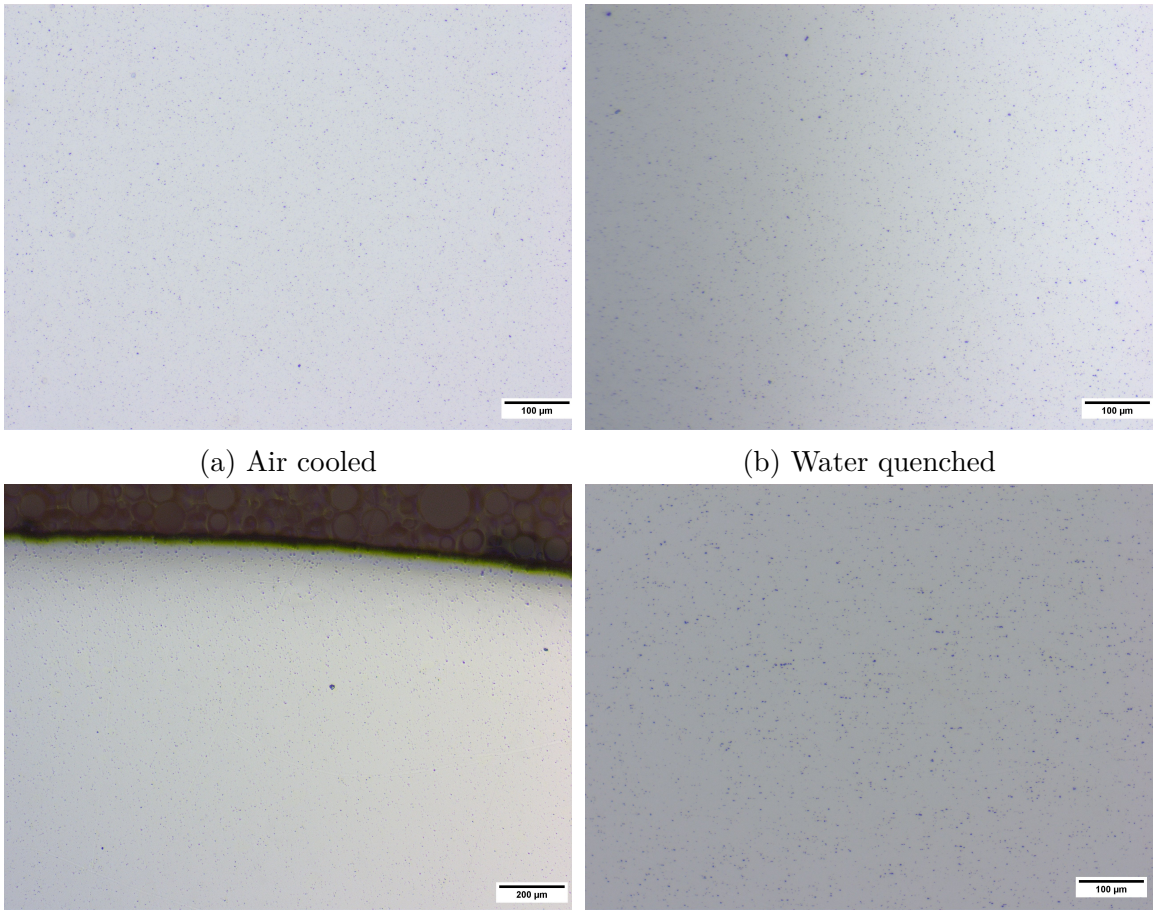

(a) Air cooled

(b) Water quenched

(c) Air cooled

(d) Water quenched

Figure 4.41: Particle structure in the longitudinal section of screw (a and b) and ram (c and d) extruded 6005.40. ED is left. (c) ED is out of micrograph.

4.3.3 Solution heat treated microstructure

A fibre structure were still present in screw extruded profiles (see Figure 4.42). Ram extruded SHT 6005.40 samples were completely recrystallized through its longitudinal section. Grain growth have occured in the center of the RE6005.40WQ sample. Note that each panorama consists of 3 or 4 micrographs, thus the scale bar might not be 1:1 ratio compared to each other.

Oxides, particles and crack effects can be seen in the cross section of SHT SE6005.40AC (see Figure 4.43). These seem to follow a circular flow. For SE6005.40WQ a zone of singular recrystallized grains can be seen towards the surface with thickness of 88 µm. Further, a zone of fibre structure distinctly separated from the center due to orientation differences have a thickness of ∼870 µm. Slight contrast differences might suggest low misorientation angles between the fibre grains. Otherwise, these cross sections supports the findings from the panorama micrographs.

The particle structure of screw extruded SHT 6005.40 samples in Figure 4.44 show randomly dispersed particles. Both ram extruded samples still show a vague tendency of particle formation aligned in the extrusion direction.

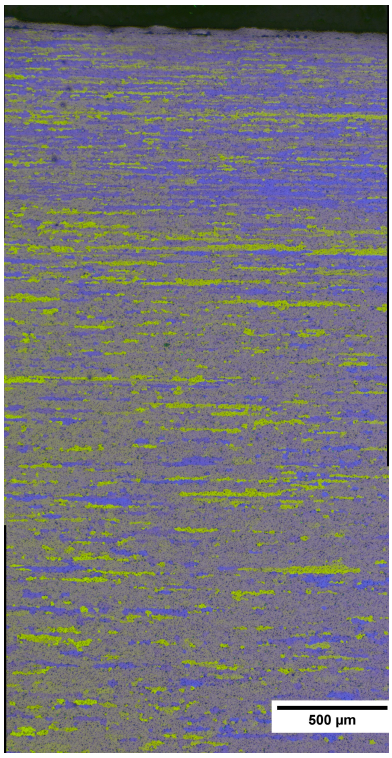

(a) Air cooled.

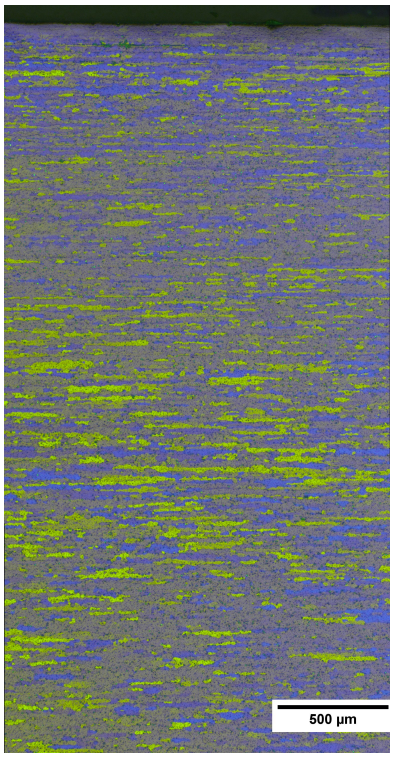

(b) Water quenched.

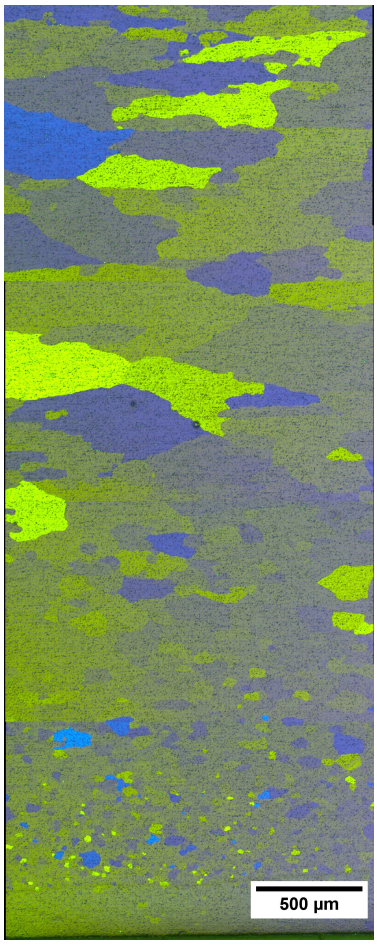

(c) Air cooled.

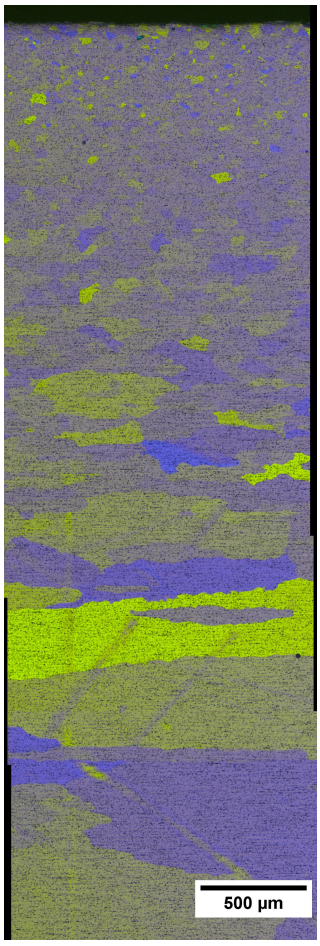

(d) Water quenched.

Figure 4.42: Grain structure in the longitudinal section of SHT 6005.40 from screw (a and b) and ram (c and d) extrusion. ED is left.

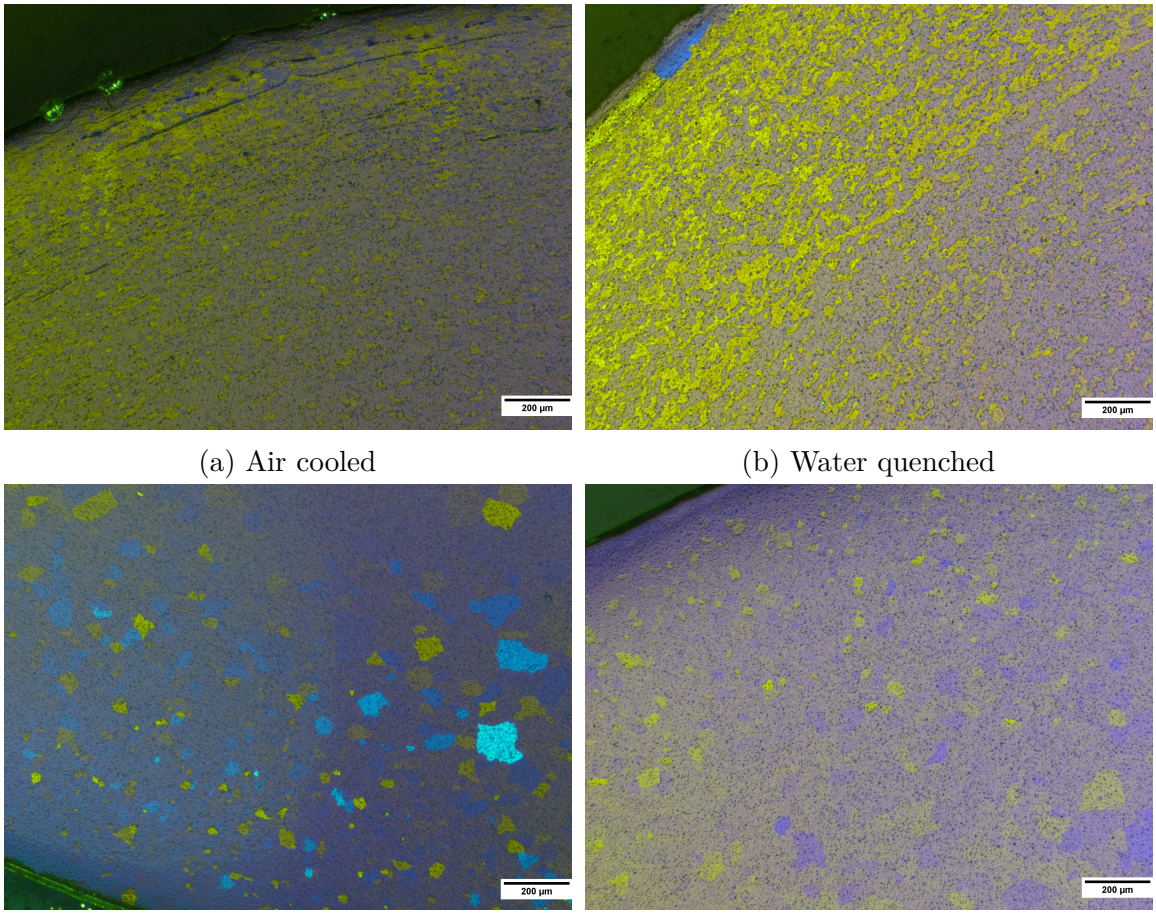

(a) Air cooled

(b) Water quenched

(c) Air cooled

(d) Water quenched

Figure 4.43: Grain structure in the cross section towards the surface of screw (a and b) and ram (c and d) extruded 6005.40. ED is out of micrograph.

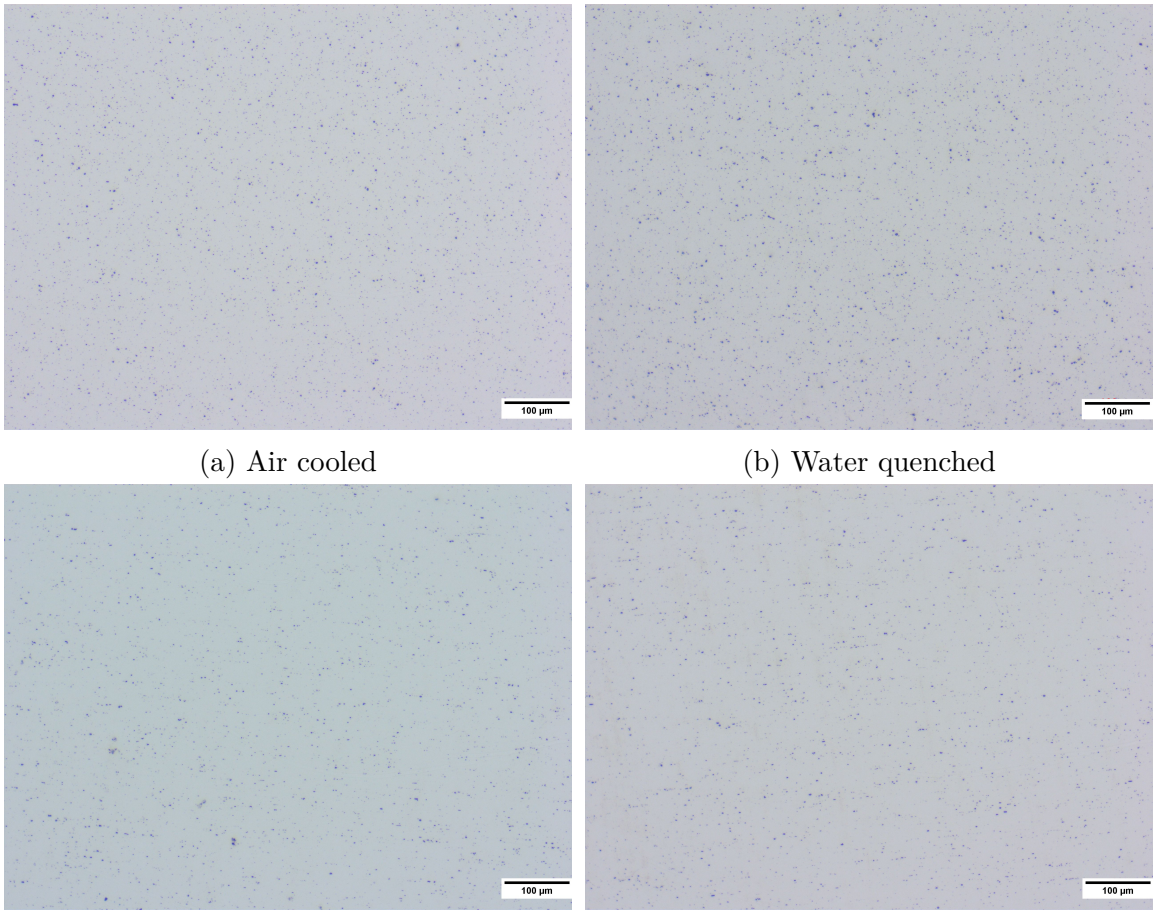

(a) Air cooled

(b) Water quenched

(c) Air cooled

(d) Water quenched

Figure 4.44: Particle structure in the longitudinal section of screw (a and b) and ram (c and d) extruded 6005.40. ED is left.

4.4 Extruded 6060.35 profiles

In Figure 4.45, a section of the surface quality on screw extruded 6060.35 can be seen. This alloy was extruded without any presence of tearing or blisters. Though, as seen in the aforementioned figure, rough marks were made when the screw extrusion stopped.

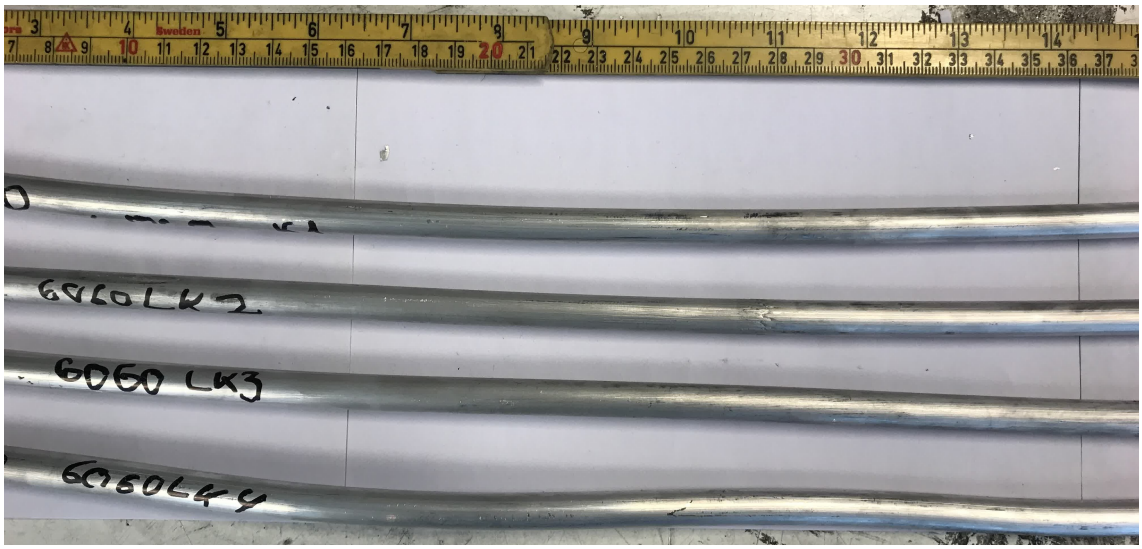

(a) Air cooled.

(b) Water quenched.

Figure 4.45: Screw extruded 6060.35 profiles. Both WQ and AC lengths have smooth surface.

The extrusion speed were split into air cooled sections with different RPM and the last water quenched section. AC1 represents the extrusion speed at 6 RPM for the first length after breakthrough. AC2 and AC3 represents extrusion speed with 9 and 10 RPM, respectively. WQ is the extrusion speed from the water quenching started. Generally the extrusion advanced with pushes of ∼5-80 cm, giving high extrusion speeds for a certain length, before stopping. Ram extrusion had an extrusion speed 632-1664 and 763 times faster than the screw extrusion for AC and WQ, respectively (see Table 4.6).

Table 4.6: Average extrusion speed for screw extruded 6060.35 profiles. Calculated from input mass difference and the given time intervals. 1 m corresponds to 212g of input material with a Ø10mm die orifice. Last column is the extrusion speed during the ram extrusion for comparison, from experiment nr. 15 in Appendix C.

	AC1	AC2	AC3	WQ	RE
Time interval [m/min]	115-176	176-196	196-268	283-304	N/A
Δ Mass [g]	360	100	870	215	N/A
Speed [m/min]	0.028	0.022	0.057	0.048	36.6

4.4.1 Mechanical properties & electrical conductivity

The hardness evolution of the extruded profiles were determined for as extruded and solution heat treated samples. Aged samples from screw extrusion clearly show that the hardness evolution were significantly worse than for ram extrusion (see Figure 4.46. As expected, this is reflected with a significantly better electrical conductivity (see Figure 4.47). Water quenching showed to have a considerable effect on both hardness and conductivity after ram extrusion, while little effect was seen for screw extrusion. Temper T1 values in Figure 4.46 and 4.47 representing the properties as extruded, without artificial aging, are shown at point 0.1 on the log time-axis.

Solution heat treatment to temper T4 shows that WQ samples increases in hardness along with SE6060.35AC. Temper T6 is seen to be similar for SE6060.35AC, SE6060.35WQ and RE6060.35AC with the peak of RE6060.35WQ at 10HV and 7HV higher than for the former three. A similar effect is seen in the conductivity. Temper T4 values in Figure 4.48 and 4.49 representing the properties as solution heat treated, without artificial aging, are shown at point 0.1 on the log time-axis.

To check if the differences in hardness at temper T1, T5 and T6 translates to the strength, nominal stress-strain curves are shown in Figure 4.50-4.53. A few of the tensile specimens fractured outside the extensometer giving invalid results. These fracture strains (see Figure 4.57) for these samples were therefore calculated from the actuator movement, assuming all samples had a length of 30 mm between the shoulders as per the dimensional drawing in Figure 3.7, Section 3.6.2.

In general for all parallels, the T1 specimens experiences extensive work hardening. Work hardening of temper T5 and T6 were considerable less. Black lines represent the as extruded temper T1 after natural aging of approximately 4 weeks (through machining). Red lines represent the aged to maximum hardness temper T5. Green lines represent the solution heat treated and aged to maximum hardness temper T6.

The main findings from the tensile tests such as UTS, YS, uniform elongation and elongation at fracture, were collected from each stress-strain curve and presented in Figure 4.54-4.57.

All four parallels show similar values for all properties at temper T6. SE6060.35AC experiences the greatest increase in YS and UTS from temper T1 and T5 to T6. On the other hand, it also changes the least between temper T1 and T5 in strength.

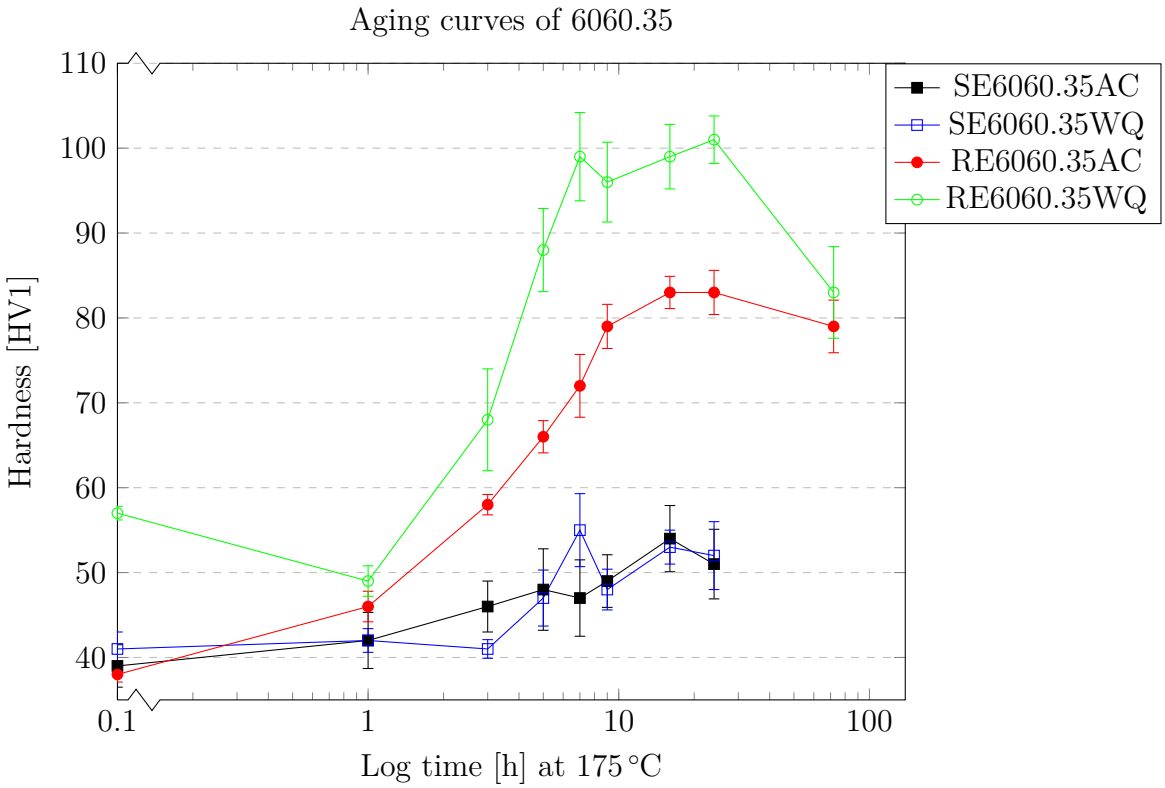

Figure 4.46: Hardness evolution with aging time at 175 °C for 6060.35 from ram and screw extruded profiles, both air cooled and water quenched.

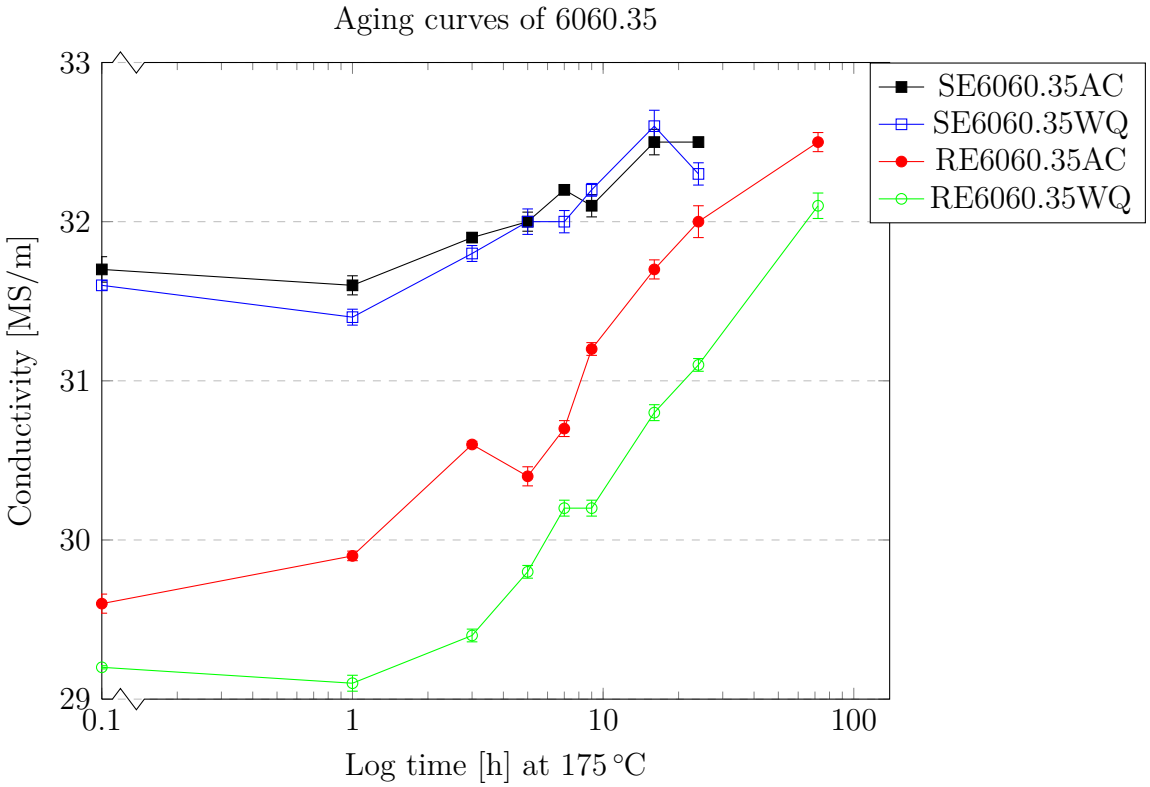

Figure 4.47: Electrical conductivity evolution with aging time at 175 °C for 6060.35 from ram and screw extruded profiles, both air cooled and water quenched.

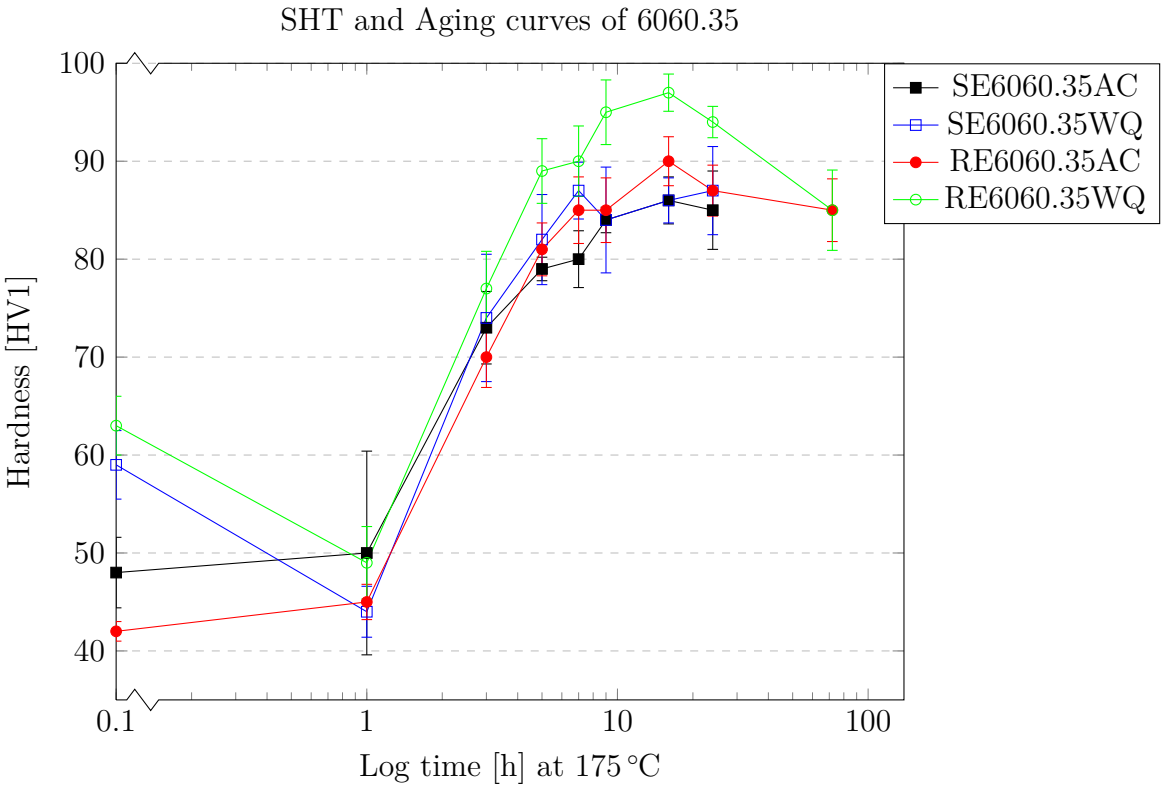

Figure 4.48: Hardness evolution with aging time at 175 °C in SHT 6060.35 for ram and screw extruded profiles, both air cooled and water quenched.

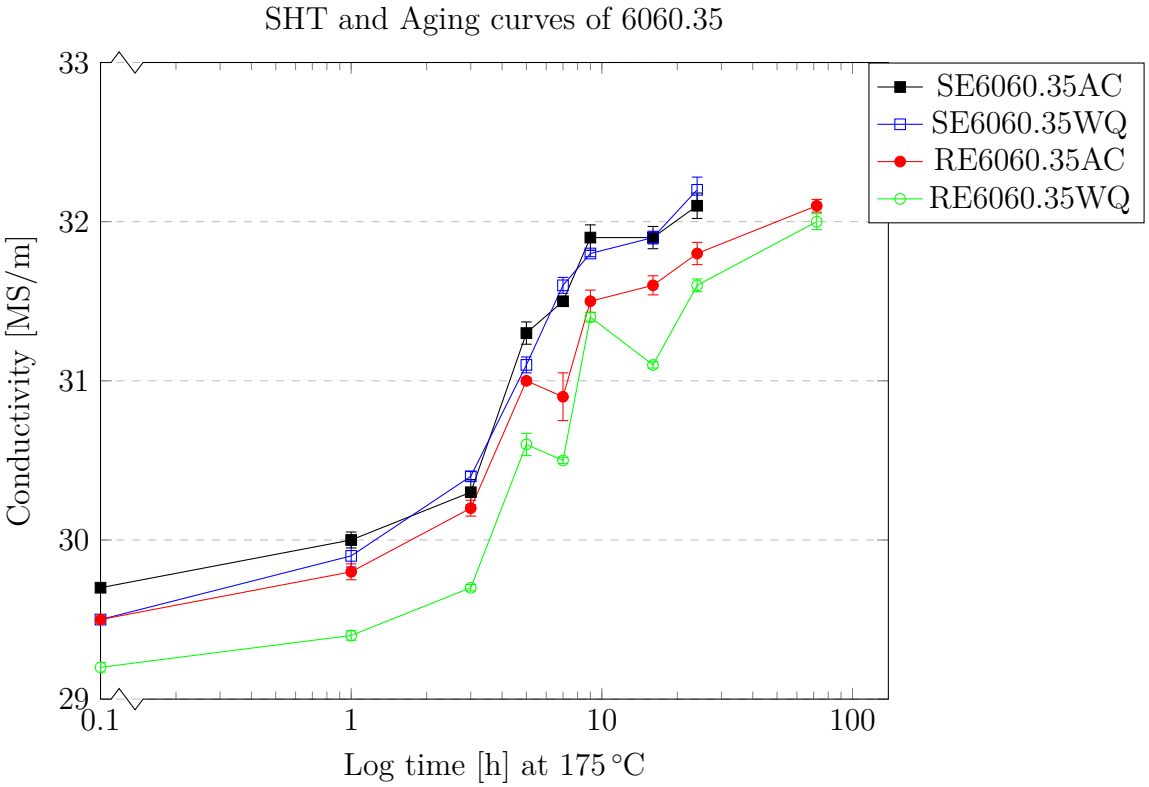

Figure 4.49: Electrical conductivity evolution with aging time at 175 °C in SHT 6060.35 for ram and screw extruded profiles, both air cooled and water quenched.

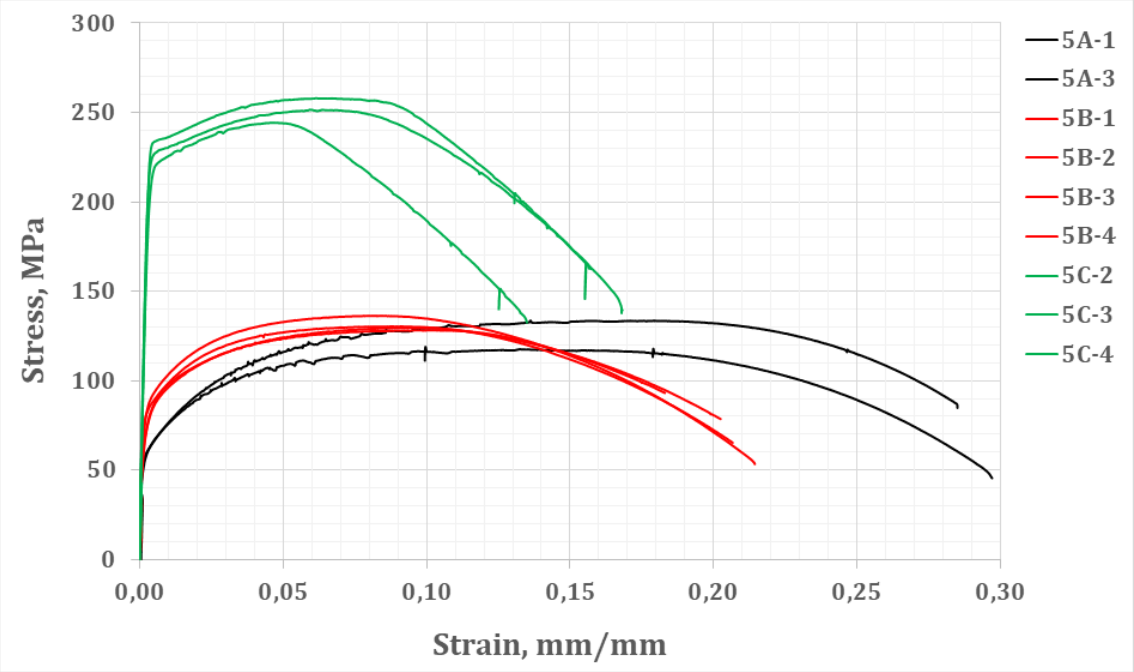

Figure 4.50: Stress-strain curve for SE6060.35AC. Black lines represent the as extruded profiles, temper T1. Red lines represent aged to maximum strength, temper T5. Green lines represent the solution heat treated and aged to maximum strength.

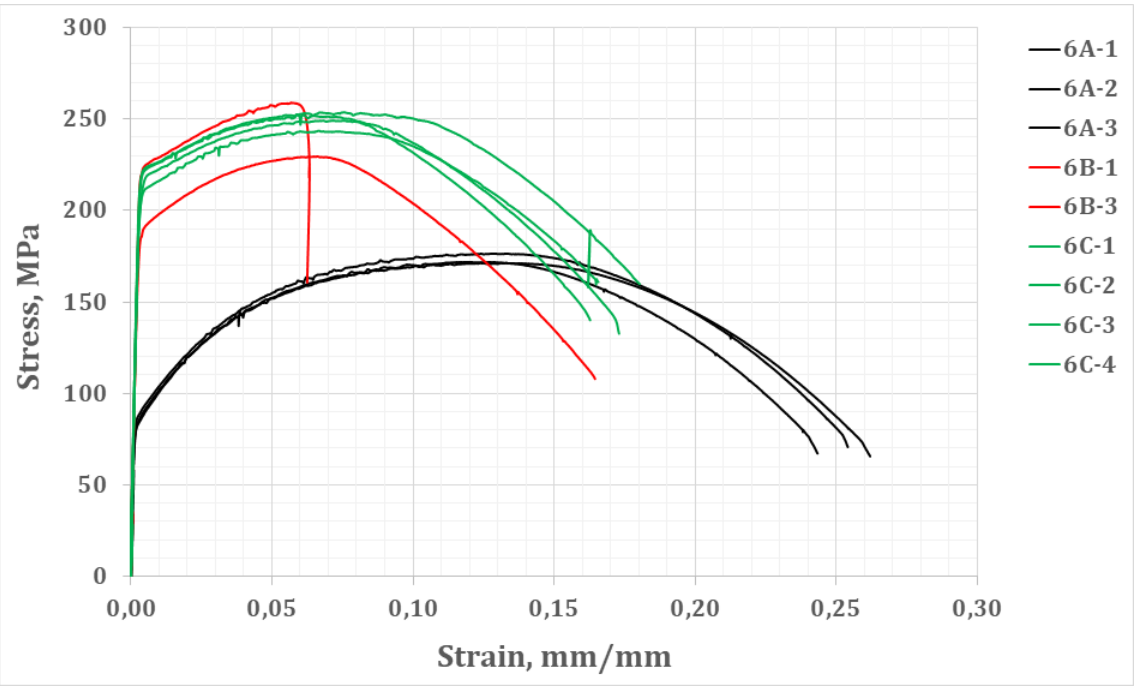

Figure 4.51: Stress-strain curve for SE6060.35WQ. Black lines represent the as extruded profiles, temper T1. Red lines represent aged to maximum strength, temper T5. Green lines represent the solution heat treated and aged to maximum strength.

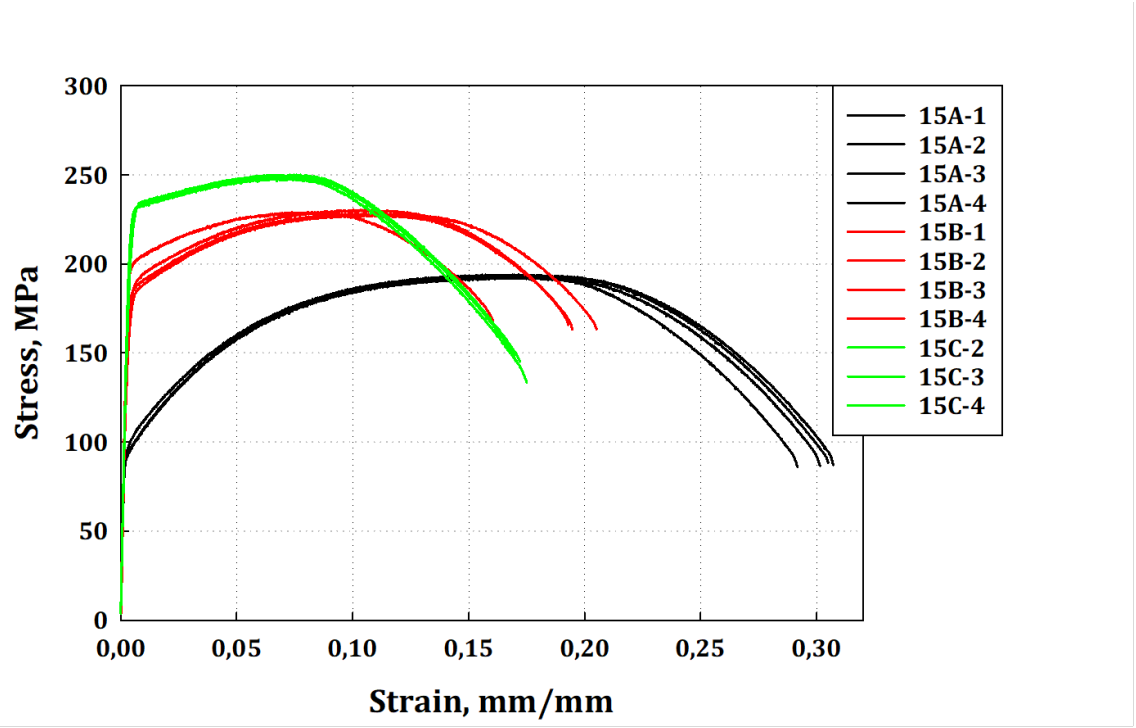

Figure 4.52: Stress-strain curve for RE6060.35AC. Black lines represent the as extruded profiles, temper T1. Red lines represent aged to maximum strength, temper T5. Green lines represent the solution heat treated and aged to maximum strength.

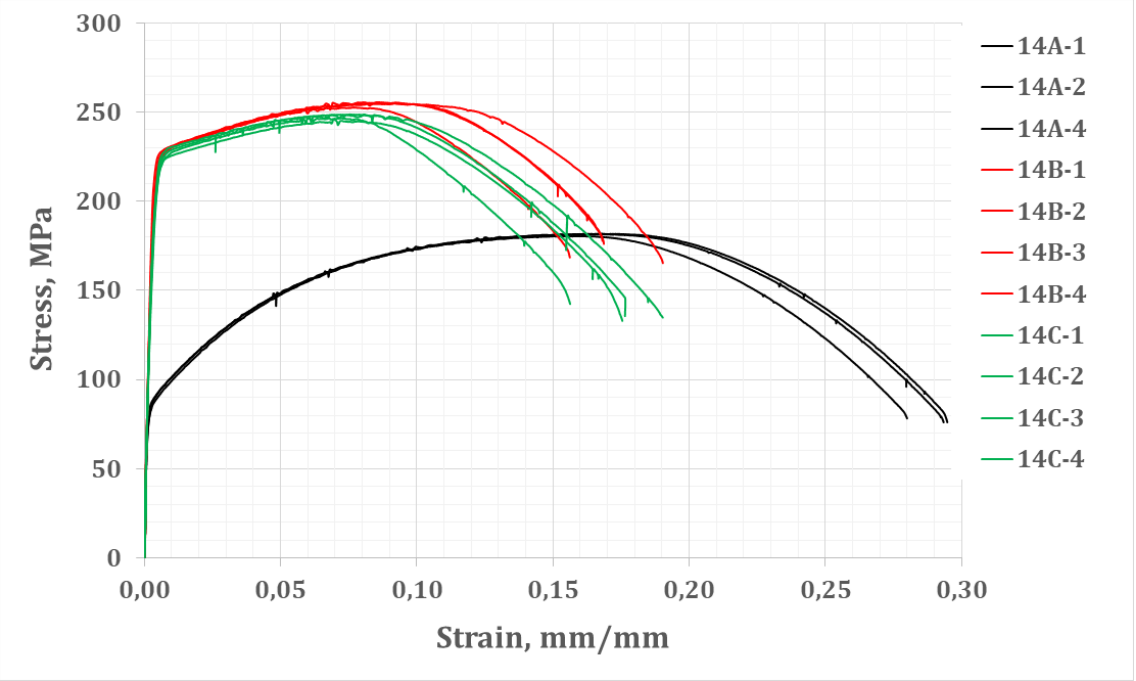

Figure 4.53: Stress-strain curve for RE6060.35WQ. Black lines represent the as extruded profiles, temper T1. Red lines represent aged to maximum strength, temper T5. Green lines represent the solution heat treated and aged to maximum strength.

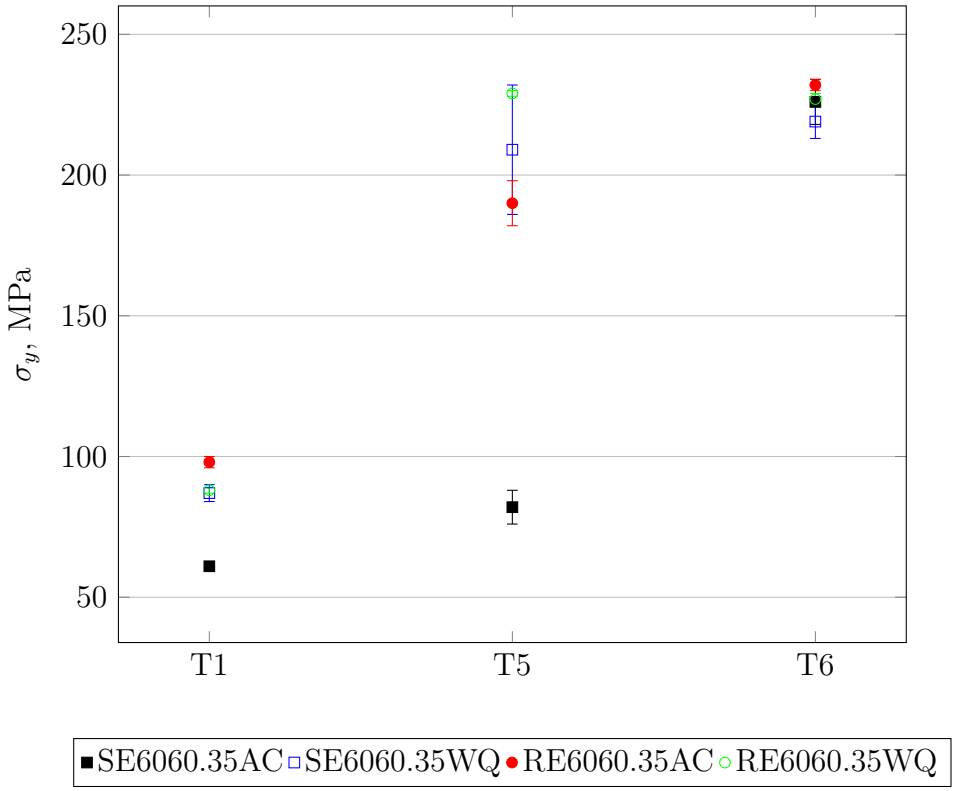

Figure 4.54: Plot of yield strength (σ_y) versus thermal states for 6060.35 from ram and screw extruded profiles, both air cooled and water quenched.

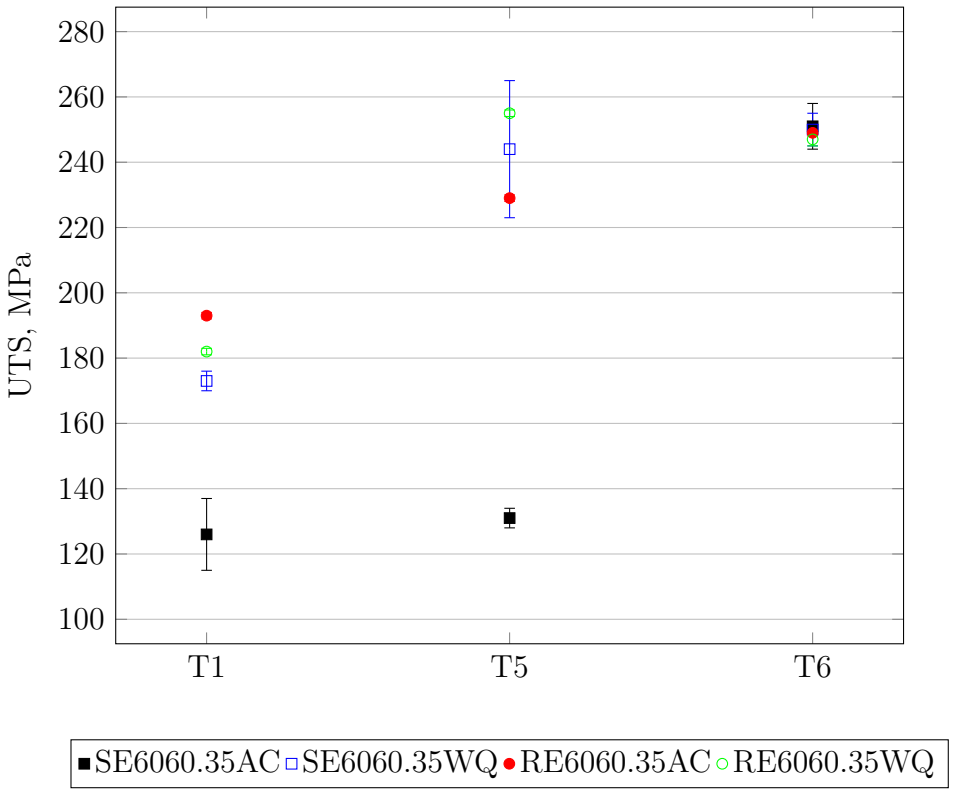

Figure 4.55: Plot of tensile strength (UTS) versus thermal states for 6060.35 from ram and screw extruded profiles, both air cooled and water quenched.

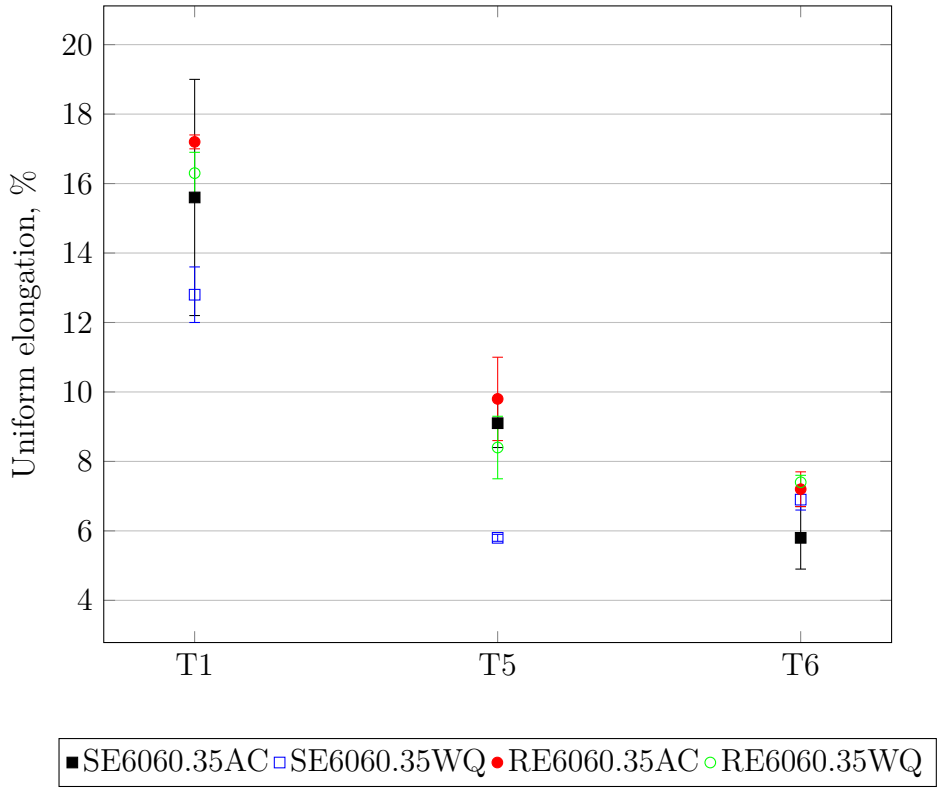

Figure 4.56: Uniform elongation versus thermal states for 6060.35 from ram and screw extruded profiles, both air cooled and water quenched.

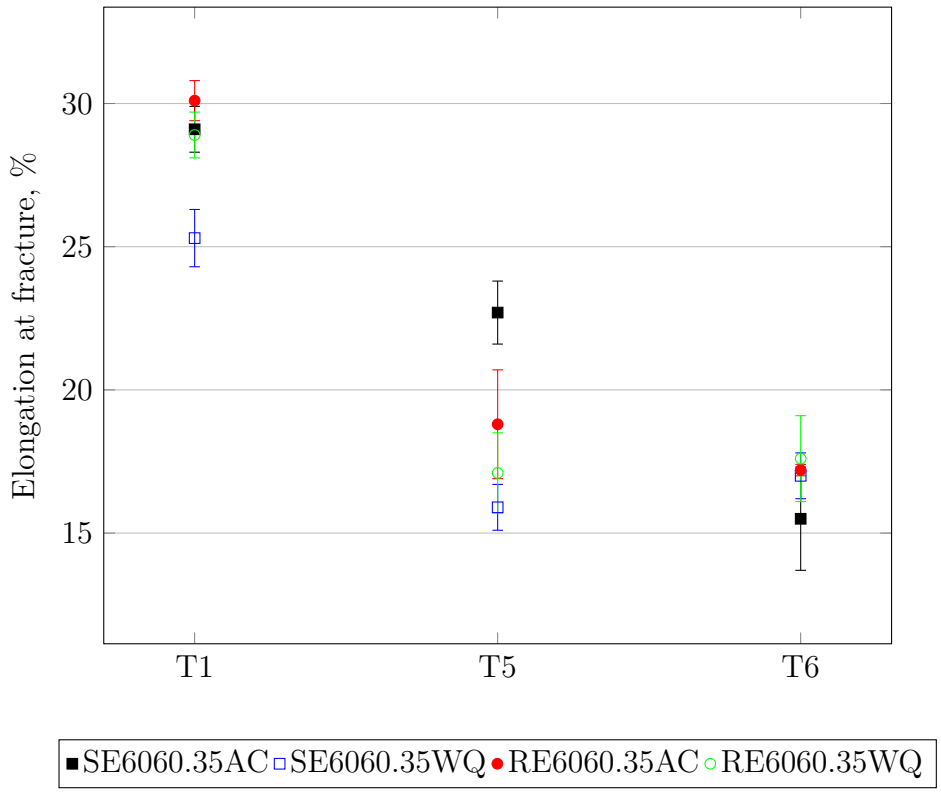

Figure 4.57: Elongation at fracture versus thermal states for 6060.35 from ram and screw extruded profiles, both air cooled and water quenched.

4.4.2 As extruded microstructure

A fibre structure can be seen in the longitudinal section for both as screw extruded profiles (see Figure 4.58). Ram extruded samples show recrystallized grains through its longitudinal section. The recrystallized grains were slightly larger in the intermediate radius and center of the section. Oxide-bands appear numerous places through the intermediate radius of SE6060.35WQ. Note that each panorama micrograph of the longitudinal section consists of 3-5 micrographs. Thus, the 500 µm scale bar on each micrograph might not be 1:1 ratio in comparison to each other.

The grain structure in the cross section can be seen in Figure 4.59. Both screw extruded samples have vague contrast differences, possibly due to low misorientation angles in the fibres.

In the micrographs of polished microstructure in Figure 4.60, particles appear randomly in the Al-matrix. The ram extruded samples showed a tendency of particle formation along the extrusion direction (ED).

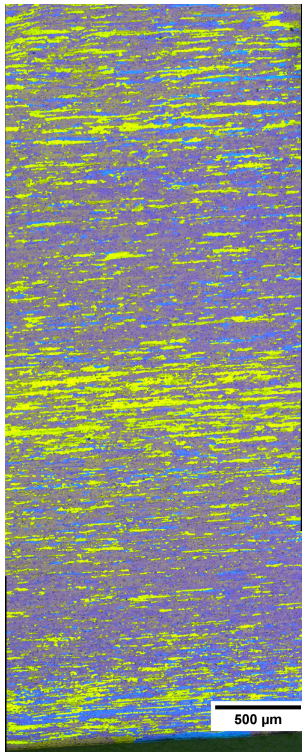

(a) Air cooled

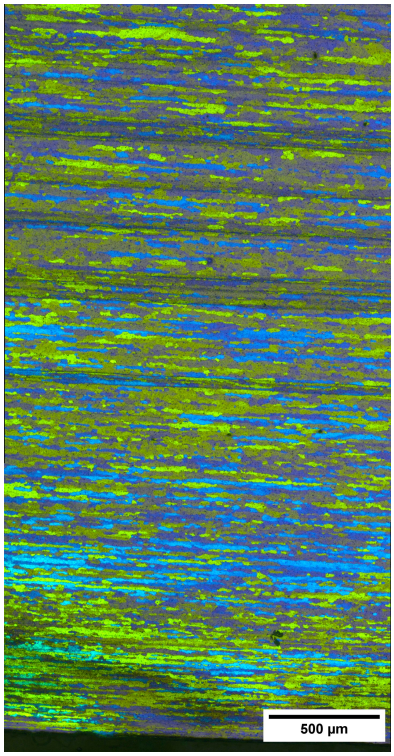

(b) Water quenched

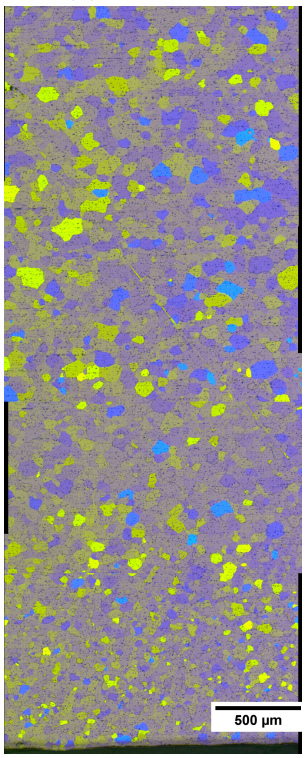

(c) Air cooled

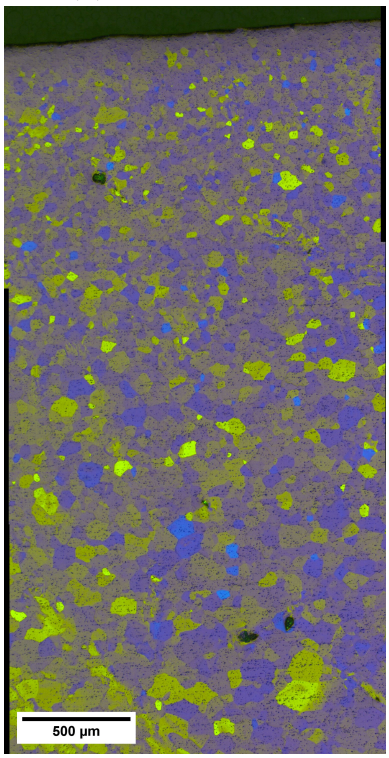

(d) Water quenched

Figure 4.58: Grain structure of screw (a and b) and ram (c and d) extruded 6060. ED is left.

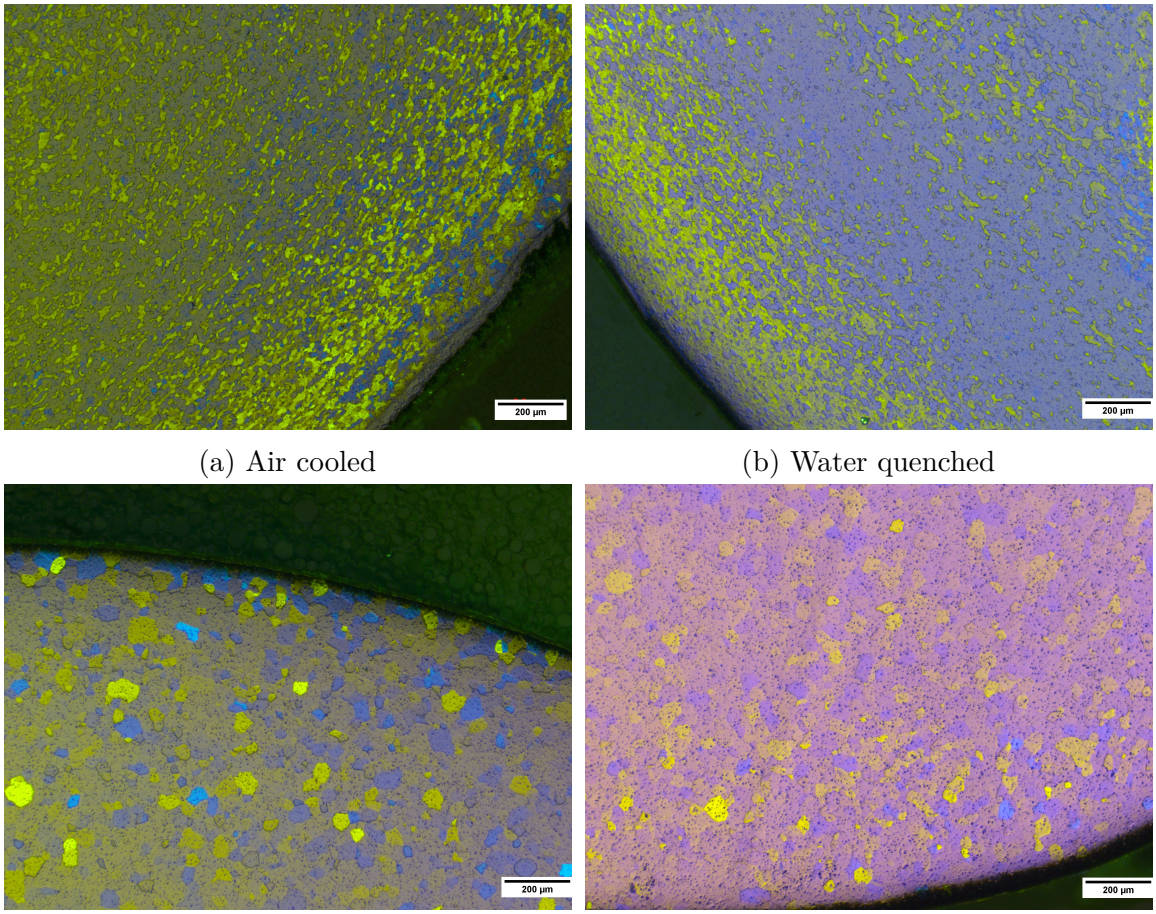

(a) Air cooled

(b) Water quenched

(c) Air cooled

(d) Water quenched

Figure 4.59: Grain structure in the cross section towards the surface of screw (a and b) and ram (c and d) extruded 6060. ED is out of micrograph.

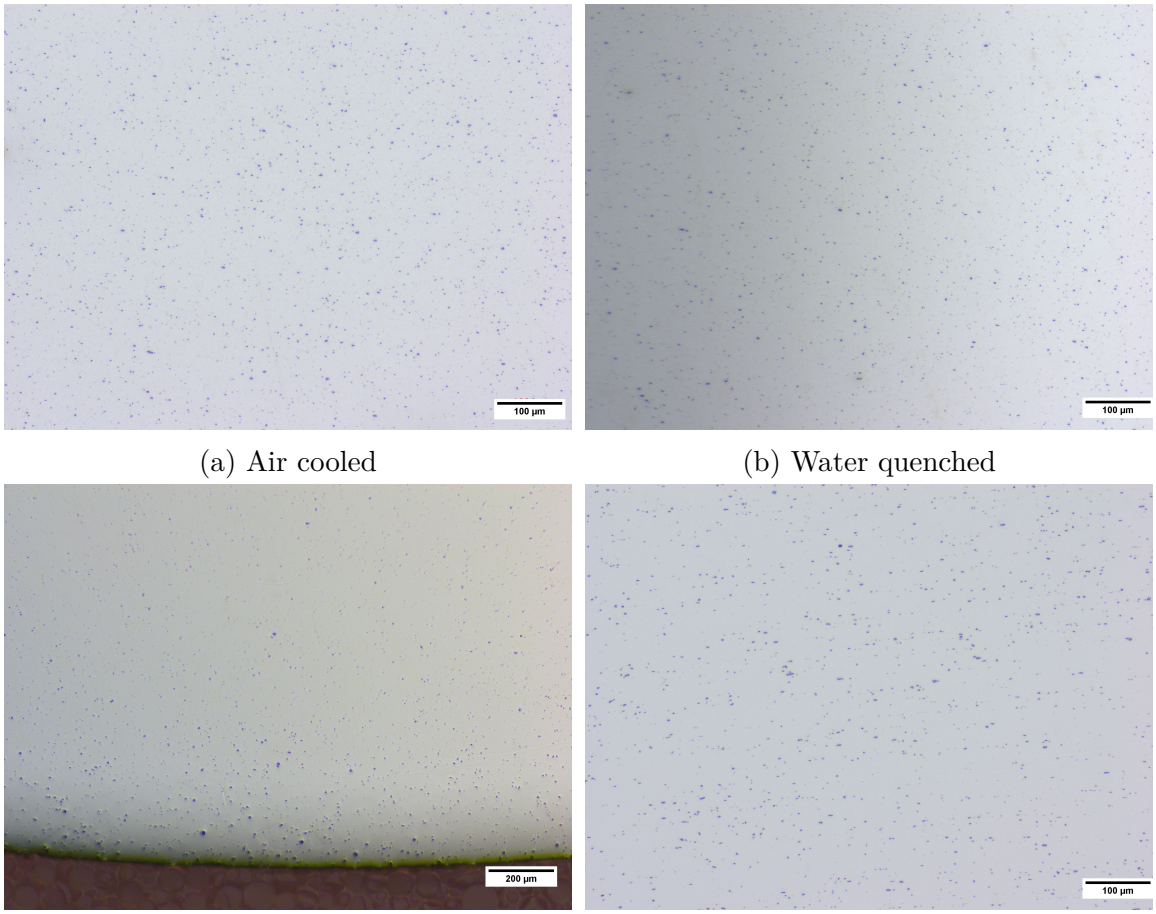

(a) Air cooled

(b) Water quenched

(c) Air cooled

(d) Water quenched

Figure 4.60: Particle structure in the longitudinal section of screw (a and b) and ram (c and d) extruded 6060. ED is left. (c) ED is out of micrograph.

4.4.3 Solution heat treated microstructure

A fibre structure were still present in screw extruded profiles (see Figure 4.61). Ram extruded SHT 6060.35 samples were completely recrystallized through its longitudinal section. Grain growth have occured at the surface for both SHT ram extruded samples. These layers of grain growth have thickness of ∼600-900 µm and 1900-2150 µm for RE6060.35AC and RE6060.35WQ, respectively. Oxide-bands appear numerous places through the intermediate radius of SE6060.35WQ. Note that each panorama consists of 3 or 4 micrographs, thus the scale bar might not be 1:1 ratio compared to each other.

Recrystallization zones can be seen in the cross section of SHT SE6060.35AC and SE6060.35WQ (see Figure 4.62). For the AC sample, two recrystallization zone can be seen with fibre structure in between these zones. The outer zone, fibre structure both have a thickness of ∼190 µm, while the inner recrystallized zone have a thickness of ∼100 µm. SE6060.35WQ were seen to have a recrystallized zone with thickness of 250-300 µm. These recrystallized zones emerged and disappeared sporadically at the surface. As with the longitudinal section, grain growth can be seen at the surface in the cross section in ram extruded samples.

The particle structure of screw extruded SHT 6060.35 samples in Figure 4.63 show randomly dispersed particles. Both ram extruded samples still show a vague tendency of particle formation aligned in the extrusion direction.

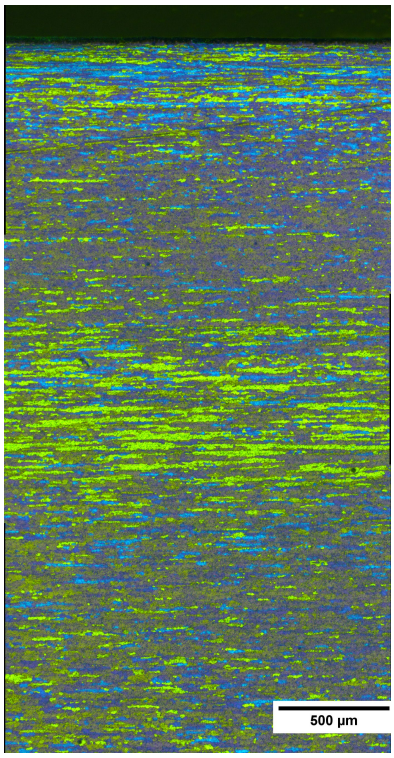

(a) Air cooled.

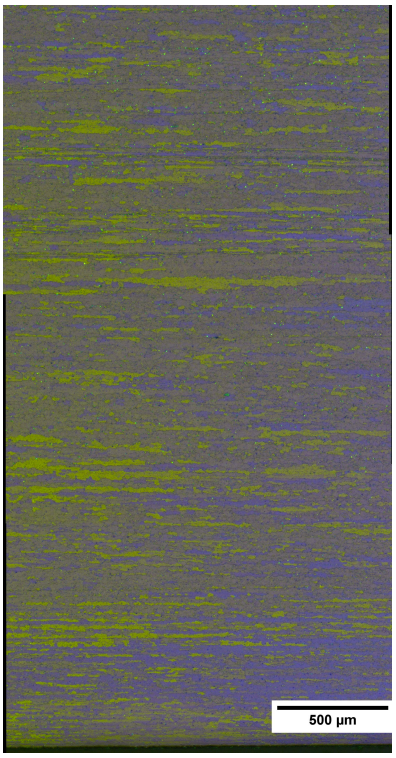

(b) Water quenched.

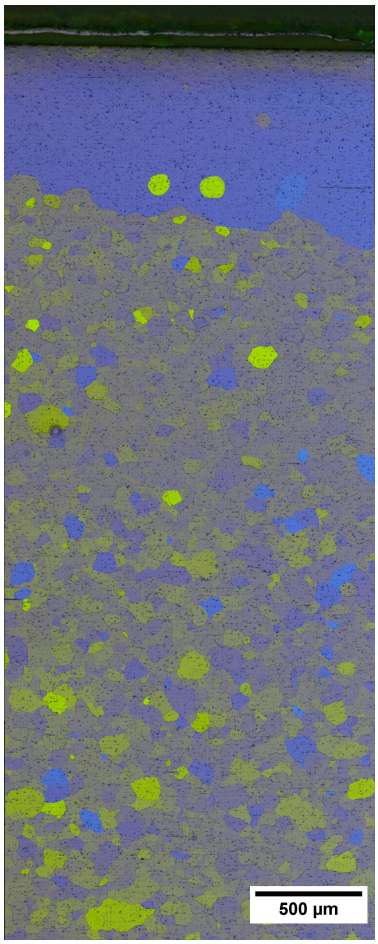

(c) Air cooled.

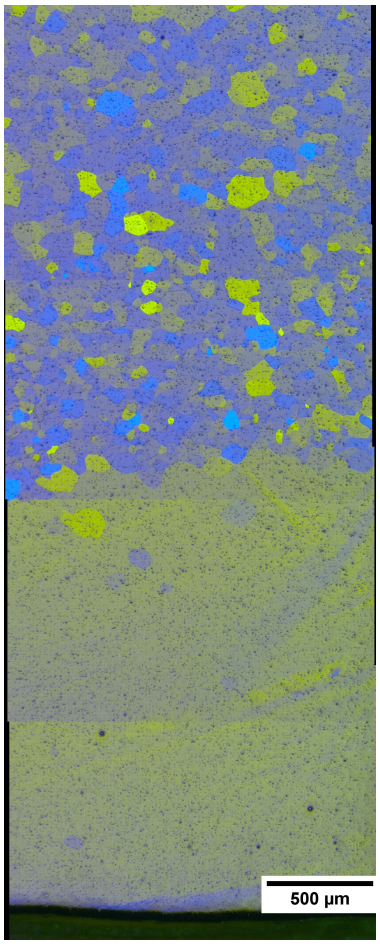

(d) Water quenched.

Figure 4.61: Grain structure in the longitudinal section of SHT 6060.35 from screw (a and b) and ram (c and d) extrusion. ED is left.

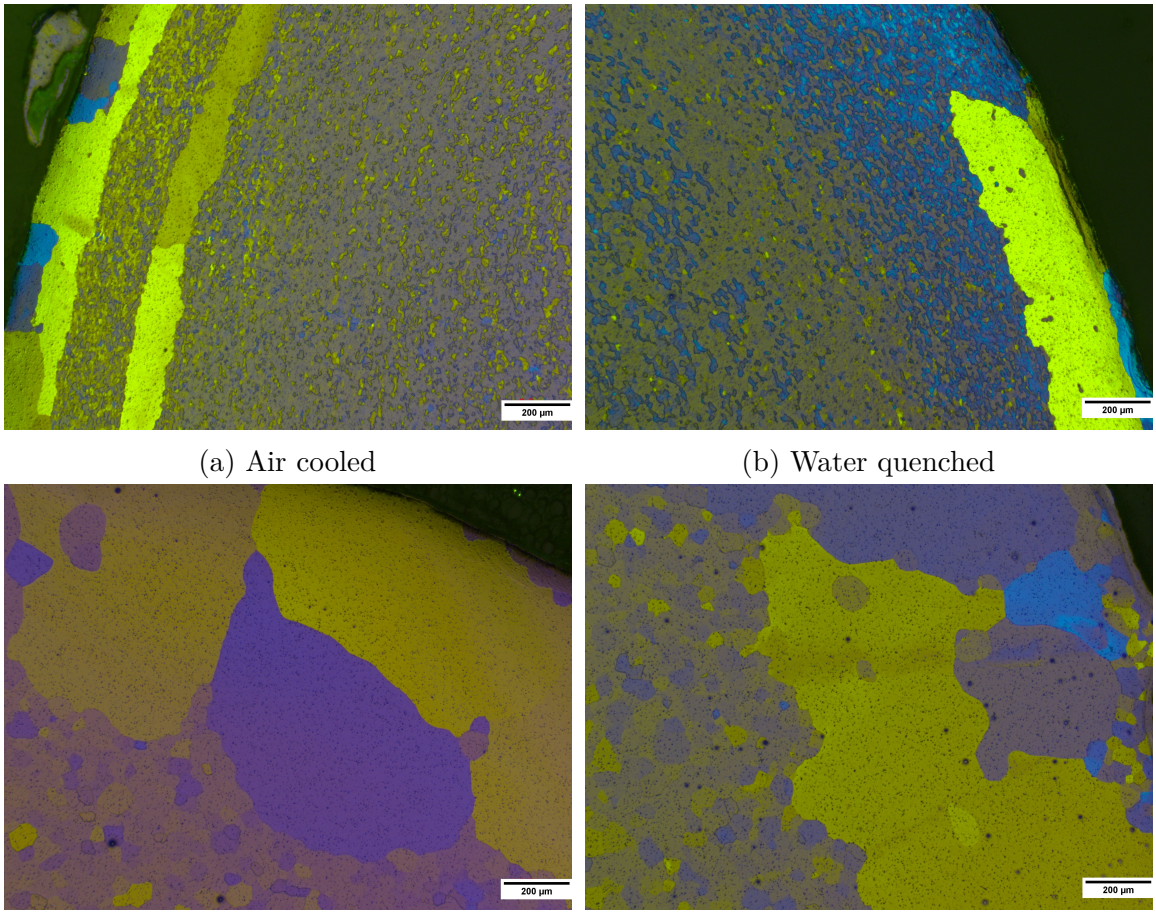

(a) Air cooled

(b) Water quenched

(c) Air cooled

(d) Water quenched

Figure 4.62: Grain structure in cross section towards the surface of screw (a and b) and ram (c and d) extruded 6060.35. ED is out of micrograph.

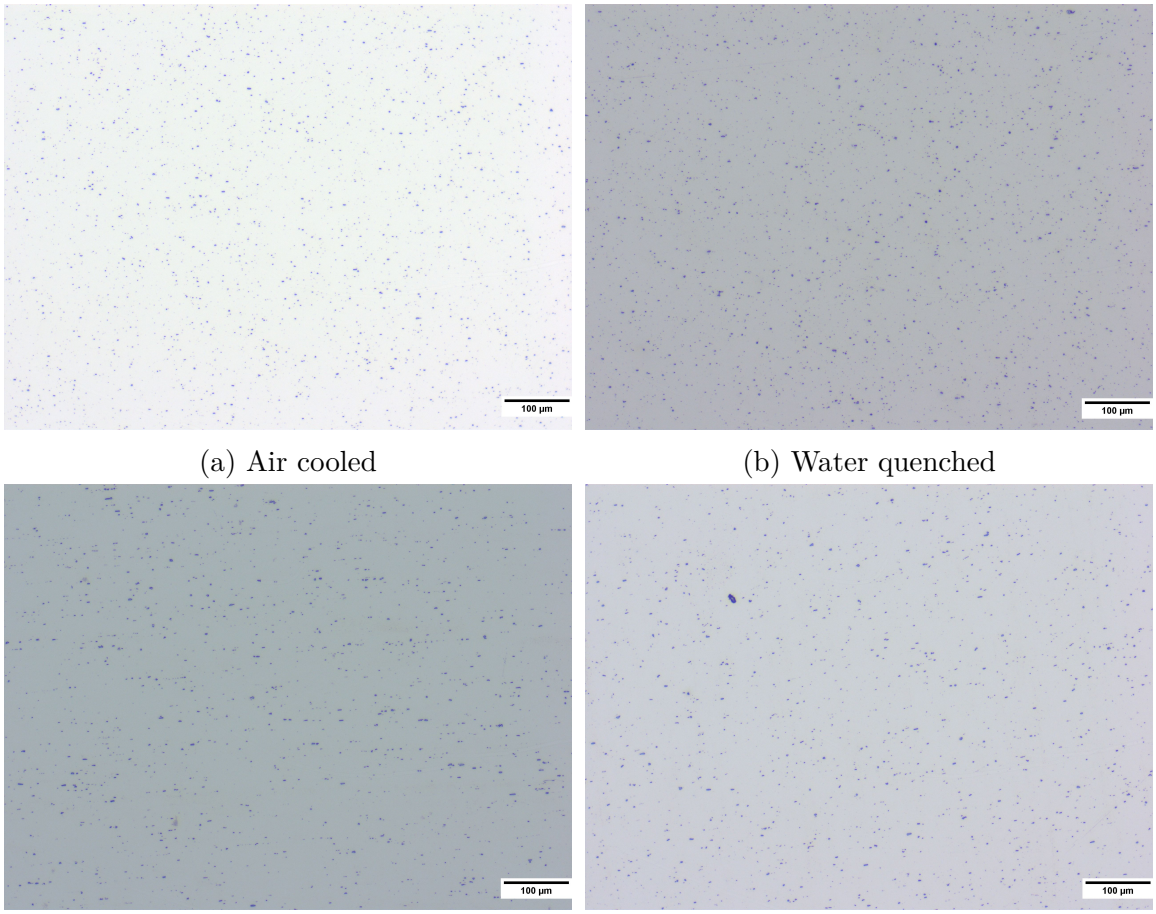

(a) Air cooled

(b) Water quenched

(c) Air cooled

(d) Water quenched

Figure 4.63: Particle structure in the longitudinal section of screw (a and b) and ram (c and d) extruded 6060.35. ED is left.

Chapter 5

Discussion

This chapter will discuss the results in greater detail. Firstly, a discussion of the microstructure and mechanical properties for material prior to extrusion will be presented, i.e. homogenized billets, and shredded and thermally cleaned granules. Secondly, observations during screw extrusion will be discussed to add context to the microstructure and properties. Thirdly, the mechanical properties and microstructural evolution of each alloy and processing condition will then be assessed. Lastly, trends observed across alloys and alloy conditions will be summarized.

5.1 Shredded & thermally cleaned granules

To assess the microstructure and mechanical properties in the screw extruded material, it is of utmost importance to understand its evolution through all the processing steps. This includes machining and shredding of billet material, thermal cleaning and the complex thermomechanical shearing occurring during screw extrusion. There are mainly two factors influencing the microstructure of the shredded granules. These are the machining including all parameters, and the thermal cleaning step. Firstly, the 6082 and 6060.35 billets were machined with some cooling lubricant, while 6005.40 were machined without any cooling lubricant. Secondly, by comparing the grain structure of the billet materials in Figure 4.1a-4.3a with the thermally cleaned granules from Figure 4.4a-4.6a, it can be seen that 6005.40 and 6060.35 granules have recrystallized grains. Average grain size was reduced from initial size by approximately a factor of 2 and 4, respectively.

6082 granules showed deformation bands in its grain structure, indicating that deformation from machining and thermal cleaning did not reach high enough temperature for recrystallization to occur. This is due to the Mn and Cr dispersoids increasing the recrystallization resistance. Considering this, it is possible that the machining deformation was a strong enough driving force directly resulting in recrystallization. If not, the stored deformation energy may have acted as a driving force for recrystallization during thermal cleaning of 6005.40 and 6060.35 [37].

5.2 Extrusion & extruded profiles

The microstructure and mechanical properties are sensitive to processing temperatures and degree of deformation inflicted on the material. Therefore, an overview of observations from each screw extrusion experiment will be covered to relate to findings in the microstructure and mechanical properties.

5.2.1 Observations during screw extrusion of 6082

As seen in the screw extrusion log of 6082 in Figure B.1 (Appendix B), the die temperature die temperature (Thermocouple, T1) were seen to be unstable throughout the experiment. The aiming point of 540 °C at the die temperature were thus not achieved. The drop from each peak to a low point can be seen to range from ∼10-30 °C for a single push of extruded material. Note that during assembly, the die tooling were to tight for thermocouple T1 to be reading the true temperature of the material. Therefore, the die temperature might be higher. Heat generation from the high degree of deformation might also have led to local melting. After disassembly, the plug formed backwards in the screw channel during extrusion showed a hole in the in the material. This support the possible local melting. Increased sticking friction to the liner have occured, restricting the screw from pushing this bulk plug forwards to the chamber plug, while generating more heat.

Neither the ram extruded nor the screw extruded 6082 profiles had visible signs of defects on the surface, i.e. tearing or blisters. The smooth surface indicated successful extrusion despite instability of the die temperature.

As stated in section 4.2, the extrusion speed of screw extrusion was negligible in comparison to ram extrusion. This difference in extrusion speeds for screw and ram extrusion probably had an influence on the amount of nucleation point for recrystallization throughout the extruded profiles.

As the screw extrusion speeds were estimated from input instead of output of material, the exact estimated value is irrelevant due to the uncertainty of the values. However, it does show differences in speed throughout the screw extrusion experiment which might influence its properties.

5.2.2 Observations during screw extrusion of 6005.40

As seen in the screw extrusion logs in Figure B.2 (Appendix B), the die temperature and torque were stable at ∼535-540 °C and 6 kNm, respectively. Steady parameters were observed from breakthrough after 29 min till approximately 58 min. During this period steady state extrusion was happening and should result in homogeneous properties along its length. After 58 min, however, unstable torque and temperature control were irregular. This instability of parameters were mostly present during water quenching. Thus, this section were more prone to have unstable extrusion and thus inhomogeneous properties. The effect of this difference in process stability is indicated in the tensile data (see Section 4.3.1). SE6005.40WQ is seen to have a much larger standard deviance than the air cooled part. This effect will be discussed further in Section 5.2.6.

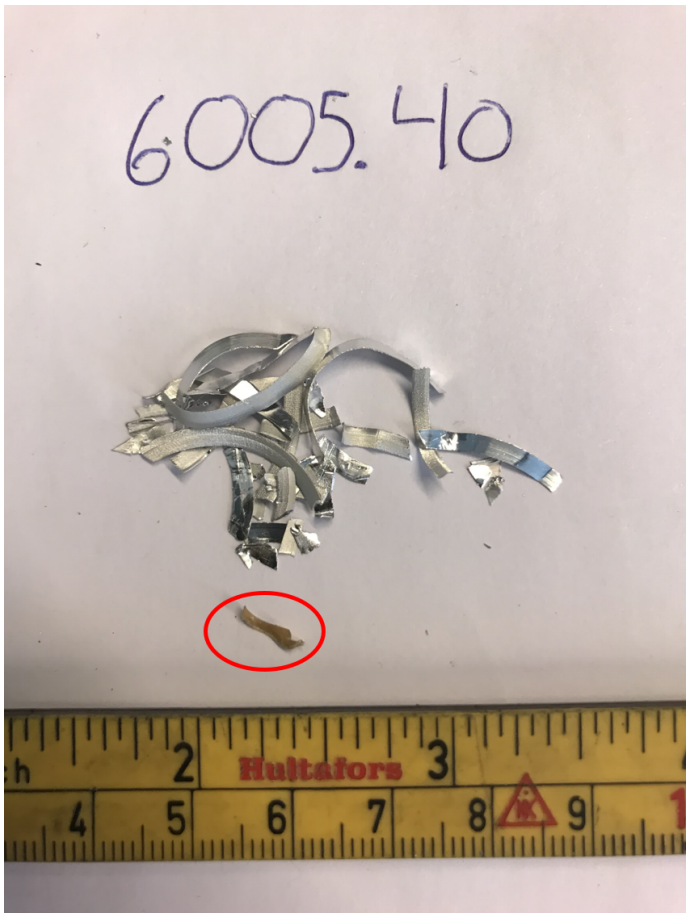

Figure 5.1: An assumed organic piece found with 6005.40 granules during feeding of the screw extruder.

During the extrusion experiment of 6005.40, pieces of an assumed organic compound were found along with the granules (Figure 5.1). These pieces were not observed during the acetone or thermal cleaning, but is likely to have been present. It is probable that these originated during machining. due to the granule shape type. Only 4 pieces were observed and removed during the screw extrusion experiment, but it is probable that several granules like these were fed into the screw extruder causing the blisters seen in Figure 4.26. The slight tearing effect seen on the surface of the last air cooled length occured during the increase and start of the instability in temperature and torque.

Due to the lack of steady state extrusion for the WQ part, the material have most likely experienced different cooling rates. The material extruded in sudden pushing motion will have gotten a full shower, quenching the material with a high rate. However, material extruded slowly in between pushes will experience a different cooling gradient. Hence, the continuous quenching will give a cooling gradient from the shower to the extrusion die. This part will likely have coarse Mg_2Si particles giving different properties throughout the WQ length. The effect of this is seen in the tensile tests of SE6005.40WQ.

5.2.3 Observations during screw extrusion of 6060.35

The screw extrusion log of 6060.35 (Appendix B) show similar instability of the die temperature as for the 6082 experiment. As the log shows, the temperature increased drastically during each "build up phase" where bulk material were seen building up back to the feed inlet. This temperature dropped significantly during extrusion pushes. This suggest that each length of profile have experienced different temperature gradients, and will subsequently exhibit different properties. In contrast to the 6082 experiment the extrusion pushes were more frequently for 6060.35, following the temperature peaks in the log.

5.2.4 Microstructural evolution of extruded profiles

As discussed in Section 5.1, the granules were seen to have deformation bands (6082) and recrystallized grains (6005.40 and 6060.35) after machining and thermal cleaning at 350 °C for 4 h.

The granules were transported in the screw channel, and started compacting. During the compression to a plug, the granules were exposed to shearing strains causing high degree of deformation and rupturing of surface oxides. All of the screw extruded profiles showed fibrous grain structure. In ram extrusion it was seen that recrystallization occured at the surface for 6082 and through the sections for 6060.35 and 6005.40 at temperatures lower than for screw extrusion (see Appendix B and C). It is therefore likely that the speed in ram extrusion generates more nucleation points for recrystallization to occur. This suggest that the larger strain that the granule material experiences in the screw, together with Mn and Cr dispersoids for 6082, have a larger resistance for recrystallization. The degree of deformation and the dispersion of oxides are two likely reason for why this happened for all three alloys and not just the dispersoid containing 6082. The solution heat treatment of screw extruded profiles support this as the additional heating up to 550 °C for 10 min did not initiate recrystallization as seen in the longitudinal section.

The cross section of SE6082AC, however, shows sporadically appearing recrystallized grains both at the surface and inwards in the radial position. Subtle signs of flow related lines were seen along or near some of these grains. There may be stored energy at these lines acting as a driving force for recrystallization. However, it is possible that the increased amount of oxides present in the material increases the resistance for recrystallization to grow. The hardness ratio of the oxide layer compared to the Al-matrix is 1800:20 at room temperature, but even higher at higher processing temperatures due to the soft aluminium matrix [23, 38]. Thus, the harder oxides may be an efficient way of pinning recrystallization.

As extruded profiles showed alignment of particles from ram extrusion. This feature was not present after screw extrusion, excluding SE6060.35WQ prior to and after SHT and SE6082AC after SHT. This effect in the SHT sample is unlikely due to the heat treatment, but rather a local phenomenon as a result of material flow during screw extrusion. Samples where this feature was not present showed a homogeneous distribution of particles. In ram extruded profiles the particle formation is aligned with the extrusion direction, and consequently with the deformation structure. After SHT, the aligned particle feature in ram extrusion was clearly still present in the

WQ sample, but with a partly aligned, partly random distribution in the AC sample. SHT SE6082AC showing the aligned oxides and precipitates, also show random distribution of particles. It is possible that an accumulation of lattice defects have occured along these flow related alignments, suggesting a higher density of Mg_2Si particles precipitated on these lines. Visual inspection of both screw extruded samples suggest there are more precipitates in the AC compared to the WQ sample. Signs of cracks are visible near the surface in SHT 6082WQ, suggesting oxide-oxide interaction and thus, poor adhesion.

The randomly dispersed particle formation seen in screw extruded 6082 resembles what is seen in both screw extruded 6060.35 and 6005.40. Polished samples showed no signs of flow related particle formation, but the anodized structure of SE6060.35WQ show extensive amounts of these lines both as extruded and after SHT. Visual inspection of the particle structure indicated that approximately the same number of particles were seen in WQ and AC samples for both 6005.40 and 6060.35. The equivalent samples from ram extrusion partly show particles aligned in the extrusion direction, but also partly random. Possible incipient polygonization sub grains can be seen at the fibre structures of these alloys, especially for 6060.35, from screw extrusion.

5.2.5 Mechanical & electrical properties of extruded 6082 profiles

Aging curves, i.e. hardness and electrical conductivity evolution over time, were performed to find the relevant tempers T5 and T6. Starting at temper T1, both screw extruded profiles exhibited an initial hardness value similar to RE6082AC, with only 2-3HV difference. RE6082WQ were as expected significantly harder than RE6082AC with an initial hardness of 85HV compared to 49HV, respectively. This is the effect of restricting SSSS from precipitating the equilibrium β-Mg_2Si phase. The water quenching were shown to have sufficiently high enough cooling rate to get on the left of the C nose in the TTT diagram (see Figure 2.7a). SE6082WQ on the other hand, were shown to have a similar curve as for RE6082WQ, but with consistently 30-40HV lower values. This can be explained by the inadequate water quenching performed during screw extrusion. Since the screw extrusion were advancing with lengths of 5-80 cm spewing out, rather than steady state extrusion, all of these lengths experienced two modes of cooling. First, since there at times were no extrusion, still air allowed for air cooling long enough for the formation of coarse, non-strengthening β-Mg_2Si particles. Second, the parts that were continuously quenched, transfered the heat from the die away. This combined have caused some strengthening solute atoms to be retained, but also precipitated β-Mg_2Si that are detrimental to the precipitation hardening potential of this alloy. This resulted in lengths of varying properties as supported in the tensile tests for this condition. The effect of this is seen in the tensile tests.

Both air cooled samples exhibit a similar effect after the air cooling, each only rising with $\sim$10HV from temper T1 to T5. This is the effect of the quench sensitivity to full degree, precipitating coarse Mg_2Si particles. Tensile strength show this effect, with T5 values slightly better than T1. Comparing the YS and UTS of RE6082AC with SE6082 and RE6082WQ with SE6082WQ, the values from ram extrusion were

consistently better than for screw extrusion. A look at SE6082WQ reveal that there have been extensive variations in the cooling of this alloy condition. With UTS values for T1 ranging from 184-315 MPa, the specimen achieving 315 MPa had equal UTS as RE6082WQ T1 sample. All of the RE6082WQ specimens reaching the strength values above the minimum value for the T5 temper (see Table 2.1), while only the two best tensile tests of SE6082WQ T1 achieving this level of strength. At the same time, SE6082WQ T5 have significantly lower UTS than T1, ranging from 154-224 MPa. This is an indication of instability in the different processing temperatures experienced by the material, as the die temperature sharply rises and falls with a difference of $\sim$30 °C during extrusion of the WQ length. Together with the pushing motion resulting in different cooling gradients after extrusion, this material show the sensitivity of temperature control and for the lack of steady state extrusion.

The difference in strength of WQ and AC ram extruded specimens at temper T6 show a stronger and less ductile RE6082AC. This may be an effect of more substructure recovery in RE6082WQ. It is worth noting that RE6082WQ were naturally aged for approximately 3 months prior to SHT. Also, solution heat treating of RE6082AC were performed without other alloy conditions present, possibly resulting in a better heat treatment. This alloy condition was also seen to be more heavily recrystallized, as discussed in Section 5.2.4.

Hardness values of T6 screw extruded samples suggest the SHT were successful, suggesting the precipitates from and after extrusion were dissolved, equalizing the age hardening potential of screw extruded samples and RE6082WQ. This is reflected in tensile tests were only slight differences were seen between the three conditions.

5.2.6 Mechanical & electrical properties of 6005.40 profiles

The hardness evolution of extruded 6005.40 showed a substantial age hardening effect for each condition. The aging response were almost identical for the WQ samples and for the AC samples, though the overall hardness for ram extrusion were higher than for screw extrusion. Higher hardness are in theory obtained for samples with more alloying elements are in solid solution prior to aging. Mg_2Si precipitate easier in alloys that are higher alloyed. Even though 6005.40 is not as high alloyed as 6082, it is still prone to precipitate coarse particles during slow cooling rates. Thus, AC samples retains less of the age hardening potential compared to WQ samples. RE6005.40AC exhibit better age hardening potential than SE6005.40AC. This is likely due to the slower extrusion speed during screw extrusion as it transfers more heat from the die at slower speeds, precipitating more particles in the process. The electrical conductivity seems to have reached a plateau for this sample. Theory on electrical conductivity states that elements in solid solution are more detrimental to the electrical conductivity than precipitates. Hence, the plateau indicates that there were little to none elements left in solid solution for the peak aged SE6005.40AC sample supporting the suggestion of more precipitation during extrusion. This effect is also seen in tensile tests as the strength of SE6005.40AC were significantly lower at T1 and T5. Even though this condition is weaker than ram extruded profiles, it still exhibits slightly worse elongation at fracture.

SHT of extruded 6005.40 increased the strength of all conditions, converging the

values of peak hardness, electrical conductivity, YS and UTS. Screw extruded profiles were seen to obtain slightly better UTS than ram extruded. The fibrous structure and oxides seen in the screw extruded samples have likely functioned as better dislocation pinning points compared to the recrystallized grain obtained in SHT samples from ram extrusion.

Tensile specimen for both screw and ram extrusion fractured differently. Cup and cone fracture were observed for the most part. However, several specimen fractured in a semi-brittle and brittle manner. RE6005.40AC at temper T5 fractured shortly after reaching UTS. AC and WQ specimens from screw extrusion at temper T6 showed a few of semi-brittle fractures, explaining the large deviance in Figure 4.38. The material conditions exhibiting these features is shown in Figure 5.2. Elongation at fracture for screw extruded specimen were seen to be lower compared to the equivalent ram extruded specimens. This may be an effect of the increased amount of brittle oxides particles in the microstructure and oxide-oxide interfaces without strong adhesion and bonding.

5.2.7 Mechanical & electrical properties of extruded 6060.35 profiles

From Figures 4.46 and 4.47, both screw extruded profiles are seen to have poor age hardening evolution compared to the equivalent from ram extrusion. While the hardness of SE6060.35AC and SE6060.35WQ increase with 15HV and 14HV, respectively, the age hardening effect on ram extruded samples were an increase of 45HV and 44HV for AC and WQ. Considering the similar hardness and conductivity of screw extruded AC and WQ samples, it was surprising to see that temper T5 differed with 127 MPa and 113 MPa for YS and UTS, respectively. A possible explanation is that the T5 WQ tensile specimens were taken from an area of 50 cm that were spewed out within a minute. Even though 6060.35 are low alloyed, it is clearly still somewhat quench sensitive.

SHT was shown to have a significant effect on the screw extruded samples, increasing the age hardening potential from initial T4 to T6 hardness with 38HV for SE6060.35AC, and from T4 to T6 with 27HV for SE6060.35WQ. Due to this, the hardness and conductivity is seen to get more equal for the all the 6060.35 parallels after SHT.

WQ samples from both processes showed that YS and UTS can be slightly better at temper T5 than at T6 [17]. Starting polygonization of substructure and recrystallized surface grains (SE6060.35WQ) and growth of recrystallized surface grains (RE6060.35WQ) of T6 samples, together with retained solute atoms in T5 samples is the reason T5 strength can be slightly higher than T6.

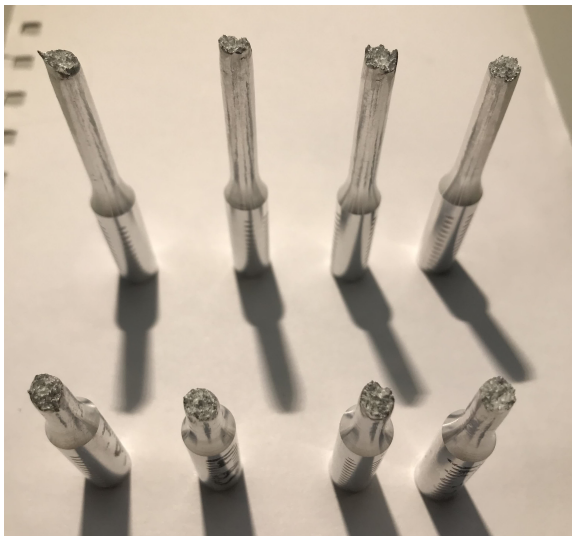

(a) RE6005.40AC-T5

(b) SE6005.40AC-T6

(c) SE6005.40WQ-T5

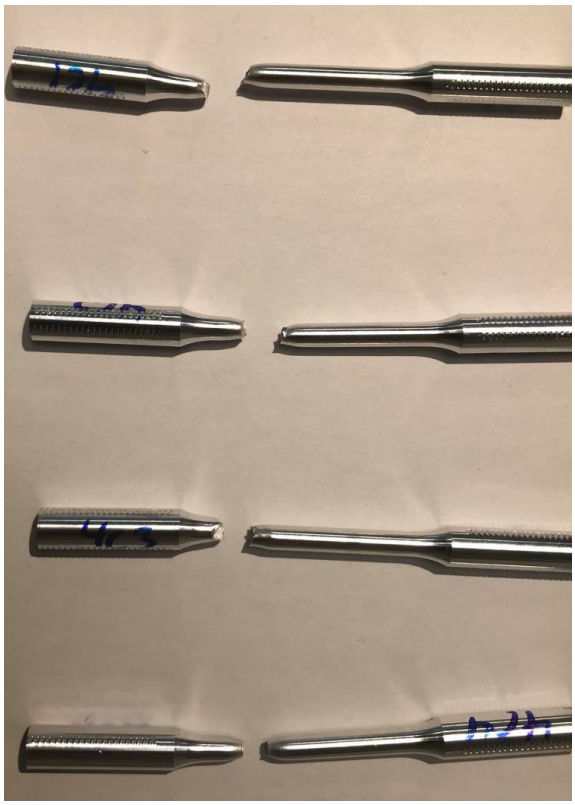

(d) SE6005.40WQ-T6

Figure 5.2: Fracture of semi-brittle 6005.40 from (a) ram extrusion, and (b)-(d) screw extrusion.

5.3 Summary

Overall trends observed over the course of the thermo-mechanical history of each alloy will be summarized in the following section. A summary of the discussion on microstructures and mechanical properties are presented.

5.3.1 Trends in microstructures

Machining of homogenized billets deformed the initial microstructure giving deformed structure of the initial grains in 6082 and stored energy in 6060.35 and 6005.40 giving more nuclei for recrystallization. The deformed grains and recrystallized grains were shown to be significantly smaller than initial grains. The machining were shown to give a slight alignment of particles along deformation bands.

Micrographs of as screw extruded profiles for all alloys showed fibrous microstructures without recrystallized zones. No indication of grain growth were seen at the surface during screw extrusion. Local cracks were observed close to the surface, but these were not prominent through its length. The particle structure of screw extruded profiles were homogeneous and without any preferential alignment as extruded. However, SE6060.35WQ plus SHT SE6060.35WQ and SHT SE6082AC show stripes of particles and possible oxides aligned as a function of the material flow in the screw extruder. This feature were seen as a local phenomenon as some samples had prominent signs of particle alignment, but others had few or none. No systematic were seen for when these stripes occured.

Screw extruded profiles were shown to have great resistance from recrystallization both for as extruded and SHT samples. This is likely due to the increase in shear strain that the material experiences through its four strain contributing steps, Section 2.2.3. The recrystallization seen in samples from screw extrusion occured at local positions. This was especially the case for both screw extruded SHT 6060.35 samples, and for SHT SE6082AC. The former showed recrystallization zones with 1-2 grains in thickness appearing and disappearing both at the surface, but also as a “belt” inside between the inner and outer fibre structure. Both of these exhibited no recrystallization in longitudinal section, while in the cross section such grains appeared sporadically. These cases may be a result of the material flow through the screw chamber and different strain contributions locally. It is probable that the the high pressure causing fast moving material centrally in the plug (see Figure 5.3), generates nuclei for recrystallization along particle and oxide bands.

Little to no difference was seen in the grain and particle structure of both as extruded and SHT from air cooled and water quenched samples after screw extrusion.

The ram extruded 6005.40 and 6060.35 exhibited fully recrystallized structure with an increase of grain size further into to center of the profiles. 6082 on the other hand, showed recrystallized zones at the surface that abruptly were stopped with fibre structure seen inside those recrystallized zones. Mn and Cr dispersoids located at the edge of the recrystallized zone are the main reason this zone stops in 6082, thus remaining with a fibre structure. The recrystallized zone at the surface of 6082 were seen to be thicker for AC samples. This is an effect of the air cooled section coming from the last part of the extruded billet, due to the heat generated by flow stress and pressure from compacting the butt.

For SHT samples from ram extrusion extensive grain growth were observed especially for 6060.35 and 6082. Recrystallized grains were swallowed by the growth of grains. The grain growth were greatest at the surface and in the center for 6060.35 and 6082, respectively.

Extrusion speed and strain gradients through the extruded profiles have an influ-

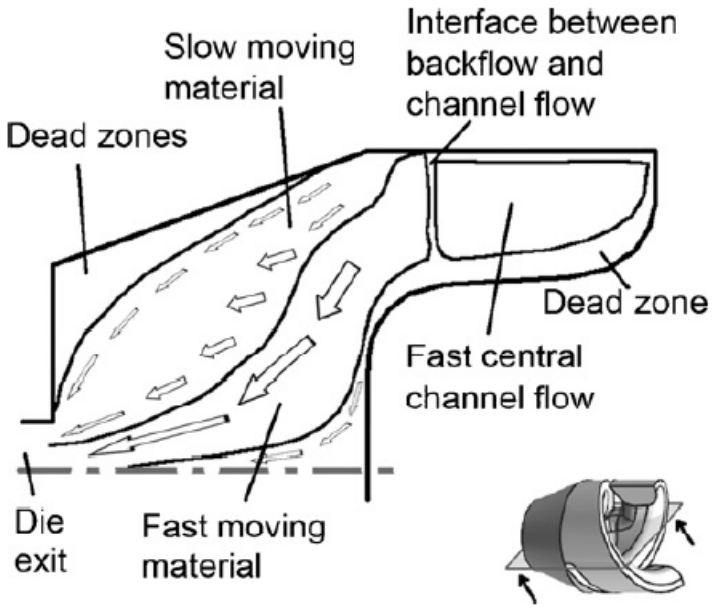

Figure 5.3: Schematic drawing from [6] illustrating typical flow pattern through the screw chamber.

ence on recrystallization and recrystallization resistance. The slower extruded profiles from screw extrusion result in fibre structure, even after SHT. It is probable that surface oxides of granules experience a high degree of puncturing and shearing, resulting in fine oxides particles homogeneously dispersed through the highly deformed profiles from screw extrusion. Thus, causing pinning effect similar to that of Mn and Cr dispersoids.

The faster extruded profiles from ram extrusion generate more nucleation points, thereby recrystallization zones were formed more easily. Due to the surface of ram extruded billets experiencing more higher degree of strain than more central parts of the profiles, fewer nucleation sites were generated. Fewer nucleation sites result in recrystallized grains growing larger as there is less grains causing a pinning effect. This explains why ram extruded 6060.35 and 6005.40 exhibit a larger grain size distribution.

The pinning effect of ram extruded 6082 are on the other hand mainly due to the homogeneously dispersed dispersoids. The grain structure of RE6082WQ shows this effect even after SHT, as the recrystallized zone has grown with the fibre structure is still present. The lack of nucleation points in the center of SHT RE6082AC may be the reason for the extensive grain growth seen.

5.3.2 Trends in mechanical properties & electrical conductivity

From the evolution of hardness and electrical conductivity, a trend showed samples with higher hardness values exhibited worse conductivity compared to those with lower hardness values. Precipitation of strengthening particles reduces the detrimental effect solute atoms have on electrical conductivity. In general, samples exhibiting the highest hardness had the lowest conductivity, and vice versa. From this combi-

nation of aging curve values it is reasonable that WQ samples have retained more precipitation hardening elements in solid solution. Air cooled samples from screw extrusion were shown to have higher conductivity, and had none or little increase in strength from T1 to T5. In other words, this showed the quench sensitivity of air cooled samples. While this effect is significantly larger for 6082, the other two alloys also show signs of β-Mg_2Si precipitation during extrusion as a function of poor water quenching due to lack of steady state extrusion. Screw extruded profiles showed more varying properties when the extrusion speed varied. Therefore, properties for some of the material can be seen to deviate significantly.

The three different thermal states, temper T1, T5 and T6 were used to evaluate the evolution of mechanical properties of extruded profiles. Age hardening showed that screw extruded material had a similar age hardening effect as for the ram extruded material. Generally though, with slightly worse values in terms of hardness and thus better conductivity. This was reflected in the properties obtained from tensile tests. Water quenched samples from ram extrusion showed the best hardness, YS and UTS. 6005.40 showed that with stable temperature control during the extrusion experiment, WQ samples from screw extrusion may achieve similar YS and UTS values as for ram extrusion. The difference in air cooled samples between the two processes were, however, significantly larger.

Temper T4 samples show dispersed hardness values for the different processes and alloys. However, from aging curves the evolution to temper T6 shows that the difference in hardness and conductivity is equalized between the conditions compared to evolution from T1 to T5. It is probable that the magnitude of precipitation hardening elements dissolving into solid solution were the same for all extruded samples, as the aging curve were similar. The tensile tests support this as the YS at T6 were approximately the same for a given alloy. It was seen that a slightly larger work hardening were experienced for temper T6 from screw extrusion. This was likely due to the recrystallization resistance seen in the screw extruded samples. Larger grains in SHT RE samples have less boundaries for dislocation pile up, thus less strengthening effect from the Hall-Petch relation.

T5 tensile specimen for 6082, 6005.40 at all extruded conditions (except for RE6082WQ) as well as SE6060.35AC, underachieved compared to the expected UTS seen in Table 2.1. The same goes for YS, excluding RE6005.40WQ. All T6 strength values were above the expected minimum values.

Chapter 6

Conclusion

In this work, 6xxx alloys were screw and ram extruded with a diameter of Ø10mm. The profiles were analysed prior to extrusion, as extruded, and at temper T5 and T6. Optical microscopy, tensile and hardness testing, and electrical conductivity measurements were used to characterize the material. Key findings from the work can be found below.

- Stable die temperature was crucial for obtaining steady-state extrusion. Screw extrusion of 6005.40WQ, with stable die temperature, was the most promising in terms of obtaining properties similar to those of ram extrusion.
- Screw extruded profiles for 6082, 6005.40 and 6060.35 have higher recrystallization resistance than for ram extrusion, all showing fibre structure as extruded and after solution heat treatment. This effect may be a result of the increased strain experienced through shearing compared to the strain from reduction in cross sectional area in ram extrusion. The extrusion speed in ram extrusion may also generate more nuclei for recrystallization.
- Air cooled temper T1 and T5 tensile specimen showed the quench sensitivity of the material. This effect was larger for screw extruded profiles. Samples from screw extrusion showed consistently lower YS and UTS than for ram extrusion.
- Properties at temper T6 were similar for all thermal conditions, i.e. air cooled and water quenched from both extrusion processes, for each alloy. At this temper, screw extruded profiles showed slightly lower elongation than ram extruded profiles.
- Screw extruded 6005.40 for both cooling methods together with SE6060.35WQ showed slightly better UTS at T6 than from ram extrusion.
- Productivity of screw extrusion is considerably lower than in ram extrusion of 6xxx alloys.
- In general, screw extrusion showed potential for obtaining mechanical properties similar to ram extrusion provided the die temperature is stable and steady state extrusion is maintained. This is crucial for the efficiency of the water quenching.

References

[1] "6xxx Aluminum Alloy Datasheets." In: *Properties and Selection of Aluminum Alloys*. Ed. by J. Weritz, J. G. Kaufman, and K. Anderson. ASM International, 2019. ISBN: 978-1-62708-210-5.

[2] O. Reiso. "Extrusion of AlMgSi Alloys." In: *Proceedings of the 9th International Conference on Aluminium Alloys* (2004).

[3] J. C. Werenskiold et al. "Screw extruder for continuous extrusion of materials with high viscosity." U.S. pat. 9616633B2. N. H. ASA. Apr. 11, 2017.

[4] J. R. Duflou et al. "Environmental assessment of solid state recycling routes for aluminium alloys: Can solid state processes significantly reduce the environmental impact of aluminium recycling?" In: *CIRP Annals* 64.1 (Jan. 1, 2015), 37–40. ISSN: 0007-8506. DOI: 10.1016/j.cirp.2015.04.051.

[5] F. Widerøe. "Material Flow in Screw Extrusion of Aluminium." PhD thesis. Trondheim: Norwegian University of Science et al., 2012.

[6] F. Widerøe and T. Welo. "Using contrast material techniques to determine metal flow in screw extrusion of aluminium." In: *Journal of Materials Processing Technology* 213.7 (July 1, 2013), 1007–1018. ISSN: 0924-0136. DOI: 10.1016/j.jmatprotec.2012.11.013.

[7] K. G. Skorpen. *Screw extrusion of light metals : development of materials, characterization and process analysis*. Vol. 2018:218. PhD thesis. Trondheim: Norwegian University of Science and Technology, 2018. ISBN: 978-82-326-3226-8.

[8] K. G. Skorpen, H. J. Roven, and O. Reiso. "A physical based empirical model for the accumulated strain in novel Metal Continuous Screw Extrusion (MCSE)." In: *Journal of Materials Processing Technology* 282 (Aug. 1, 2020). ISSN: 0924-0136. DOI: 10.1016/j.jmatprotec.2020.116670.

[9] K. G. Skorpen. "Comparison of binary AlMg alloys processed by continuous screw extrusion or conventional ram extrusion." In: *Screw extrusion of light metals : development of materials, characterization and process analysis*. PhD thesis 2018:218 (2018). Unpublished, 203–224.

[10] G. Langelandsvik. "Optimization of Electrical Conductivity in Screw Extruded Wires." Master thesis. 2017.

[11] K. H. Kristiansen. *Characterization of screw extruded 6xxx alloys*. Technical report. NTNU, Jan. 2020.

[12] M. N. Amado and F. Daroqui. "Revision of The Solvus Limit of Al-Mg2Si Pseudo Binary Phase Diagram." In: *International Congress of Science and Technology of Metallurgy and Materials, SAM - CONAMET 2013* 8 (Jan. 1, 2015), 1079–1088. ISSN: 2211-8128. DOI: 10.1016/j.mspro.2015.04.

171. URL: http://www.sciencedirect.com/science/article/pii/S2211812815001728.

[13] *International Alloy Designations and Chemical Composition Limits for Wrought Aluminum and Wrought Aluminum Alloys*. Teal Sheet. The Aluminum Association, Aug. 2018.

[14] S. Gulbrandsen-Dahl and K. Marthinsen. "Hardening of Al-Mg-Si Alloys and Effective Particle Size in Microstructural Models." In: *Materials Science Forum* (2014). DOI: 10.4028/www.scientific.net/MSF.783-786.252.

[15] J. K. Solberg. *Teknologiske metaller og legeringer*. Ed. by Norges teknisk-naturvitenskapelige universitet Institutt for materialteknologi. Trondheim, 2014.

[16] S. J. Andersen et al. "The crystal structure of the β" phase in Al–Mg–Si alloys." In: *Acta Materialia* 46.9 (May 22, 1998), 3283–3298. ISSN: 1359-6454. DOI: 10.1016/S1359-6454(97)00493-X.

[17] J. Røyset, U. Tundal, and O. Reiso. "Comparison of Properties of Extruded 6xxx Alloys in T5 Temper versus T6 Temper." In: *Proceedings of the 9th International Conference on Aluminium Alloys* (2004).

[18] H. S. Hasting et al. "Composition of β precipitates in Al–Mg–Si alloys by atom probe tomography and first principles calculations." In: *Journal of Applied Physics* 106.12 (Dec. 15, 2009). Publisher: American Institute of Physics, 123527. ISSN: 0021-8979. DOI: 10.1063/1.3269714. (Accessed 07/26/2020).

[19] *Aluminium and aluminium alloys - Extruded rod/bar, tube and profiles - Part 2: Mechanical properties (NS-EN 755-2:2016)*. In: ed. by T. C. C. 132. European Commitee for Standardization, 2016.

[20] "Properties and Applications of Wrought Aluminum Alloys." In: *Properties and Selection of Aluminum Alloys*. Ed. by J. G. Kaufman. ASM International, June 2019. ISBN: 978-1-62708-210-5.

[21] P. Saha. "Extrusion and Drawing of Aluminum Alloys." In: *Aluminum Science and Technology*. Vol. 2A. ASM Handbooks. ASM International, 2018. ISBN: 978-1-62708-207-5.

[22] P. K. Saha. *Aluminum Extrusion Technology*. Materials Park, OH: ASM International, 2000. 259 pp. ISBN: 978-0-87170-644-7.

[23] J. Cui. "Solid state recycling of aluminium scrap and dross characterization." PhD thesis. Norwegian University of Science and Technology, 2011.

[24] "Aluminum Alloy Nomenclature and Temper Designations." In: *Aluminum Science and Technology*. Ed. by J. Weritz. ASM International, 2018. ISBN: 978-1-62708-207-5.

[25] Y. Birol. "Precipitation during homogenization cooling in AlMgSi alloys." In: *Transactions of Nonferrous Metals Society of China* 23.7 (2013), 1875–1881. ISSN: 1003-6326. DOI: https://doi.org/10.1016/S1003-6326(13)62672-2.

[26] N. C. W. Kuijpers et al. "The dependence of the β-AlFeSi to α-Al(FeMn)Si transformation kinetics in Al–Mg–Si alloys on the alloying elements." In: *Materials Science and Engineering: A* 394.1 (2005), 9–19. ISSN: 0921-5093. DOI: https://doi.org/10.1016/j.msea.2004.09.073.

[27] A. Harriss et al. "The Effect of Homogenizing on the Quench Sensitivity of 6082." In: *Materials science forum* 396-402 (2002), 655–660. ISSN: 0255-5476.

[28] C. Vargel. "Chapter A.3 - The Metallurgy of Aluminium." In: *Corrosion of Aluminium*. Ed. by C. Vargel. Amsterdam: Elsevier, Jan. 1, 2004, 23–57. ISBN: 978-0-08-044495-6. DOI: 10.1016/B978-008044495-6/50008-2.

[29] I. Polmear. *Light Alloys: From Traditional Alloys to Nanocrystals*. Elsevier, Nov. 11, 2005. 437 pp. ISBN: 978-0-08-049610-8.

[30] B. C. Shang et al. "Investigation of quench sensitivity and transformation kinetics during isothermal treatment in 6082 aluminum alloy." In: *Materials & Design* 32.7 (Aug. 1, 2011), 3818–3822. ISSN: 0261-3069. DOI: 10.1016/j.matdes.2011.03.016.

[31] "Recovery, Recrystallization, and Grain-Growth Structures." In: *Metalworking: Bulk Forming*. Ed. by S. Semiatin. ASM International, 2005, 552–562. ISBN: 978-1-62708-185-6. DOI: 10.31399/asm.hb.v14a.a0004019.

[32] W. D. Callister. *Materials science and engineering*. 9th ed., SI Version. Hoboken, N.J: Wiley, 2015. ISBN: 978-1-118-31922-2.

[33] *Aluminum Science and Technology*. Red. by K. Anderson, J. Weritz, and J. G. Kaufman. ASM International, Nov. 2018. ISBN: 978-1-62708-207-5.

[34] R. E. Smallman and A. H. W. Ngan. "Chapter 13 - Precipitation Hardening." In: *Modern Physical Metallurgy (Eighth Edition)*. Ed. by R. E. Smallman and A. H. W. Ngan. Oxford: Butterworth-Heinemann, Jan. 1, 2014, 499–527. ISBN: 978-0-08-098204-5. DOI: 10.1016/B978-0-08-098204-5.00013-4.

[35] C. T. Rueden et al. "ImageJ2: ImageJ for the next generation of scientific image data." In: *BMC bioinformatics* 18.1 (2017), 529.

[36] J. Schindelin et al. "Fiji: an open-source platform for biological-image analysis." In: *Nature methods* 9.7 (2012), 676.

[37] K. K. Alaneme and E. A. Okotete. "Recrystallization mechanisms and microstructure development in emerging metallic materials: A review." In: *Journal of Science: Advanced Materials and Devices* 4.1 (Mar. 1, 2019), 19–33. ISSN: 2468-2179. DOI: 10.1016/j.jsamd.2018.12.007.

[38] G. Xie et al. "Effect of surface oxide films on the properties of pulse electric-current sintered metal powders." In: *Metallurgical and Materials Transactions A* 34.11 (Nov. 1, 2003), 2655–2661. ISSN: 1543-1940. DOI: 10.1007/s11661-003-0024-1.

Appendix A

Chemical analysis of billet material

Table A.1: Chemical analysis of the 6060.35, 6005.40 and 6082 alloys. The test were performed by Hydro prior to the start of this study.

Alloy Element	6060.35 wt%	6005.40 wt%	6082 wt%
Si	0,42	0,60	1,00
Fe	0,20	0,20	0,22
Cu	0,0022	0,15	0,033
Mn	0,026	0,19	0,57
Mg	0,46	0,55	0,67
Cr	0,0033	0,0015	0,0055
Ti	0,0094	0,014	0,013
B	0,0012	0,0017	0,0014
Al	98,83	98,26	97,44

Appendix B

Screw extrusion log

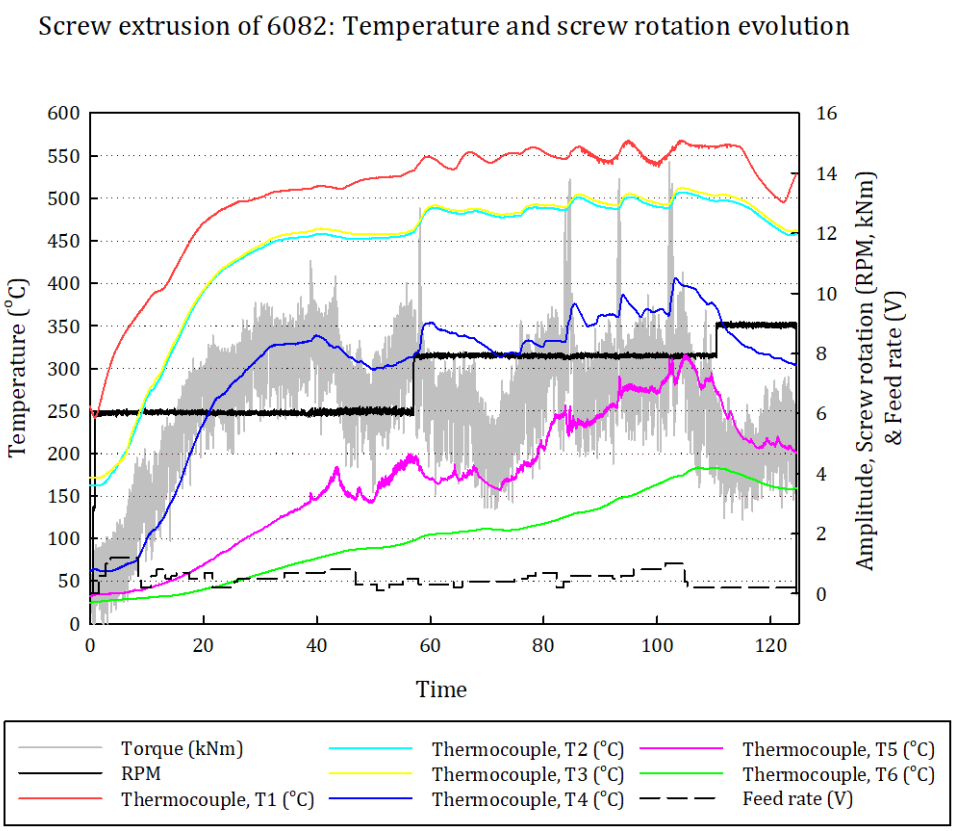

(a)

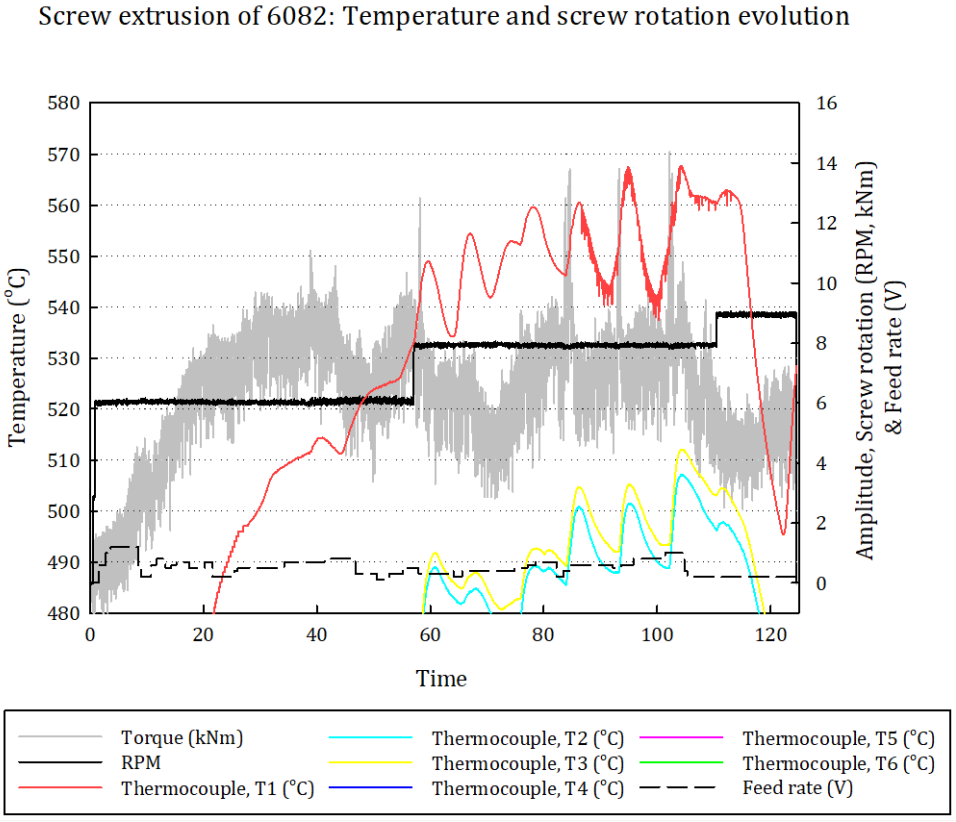

(b)

Figure B.1: Temperature and screw momentum evolution during the extrusion process of 6082. (b) focus on thermocouple T1.

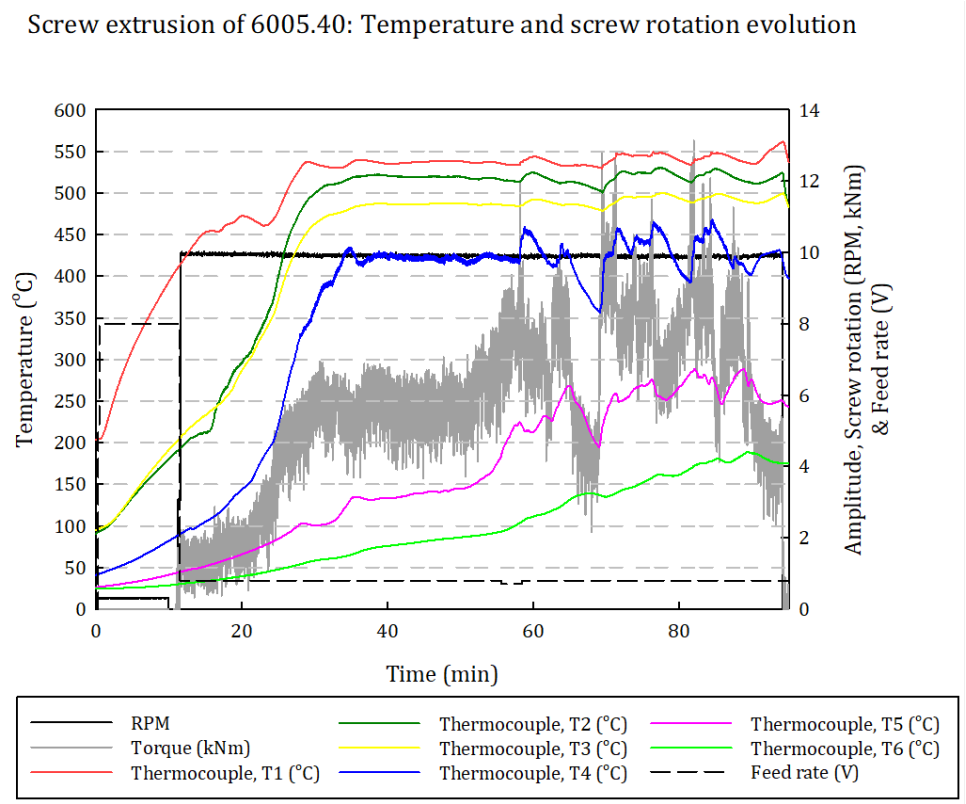

(a)

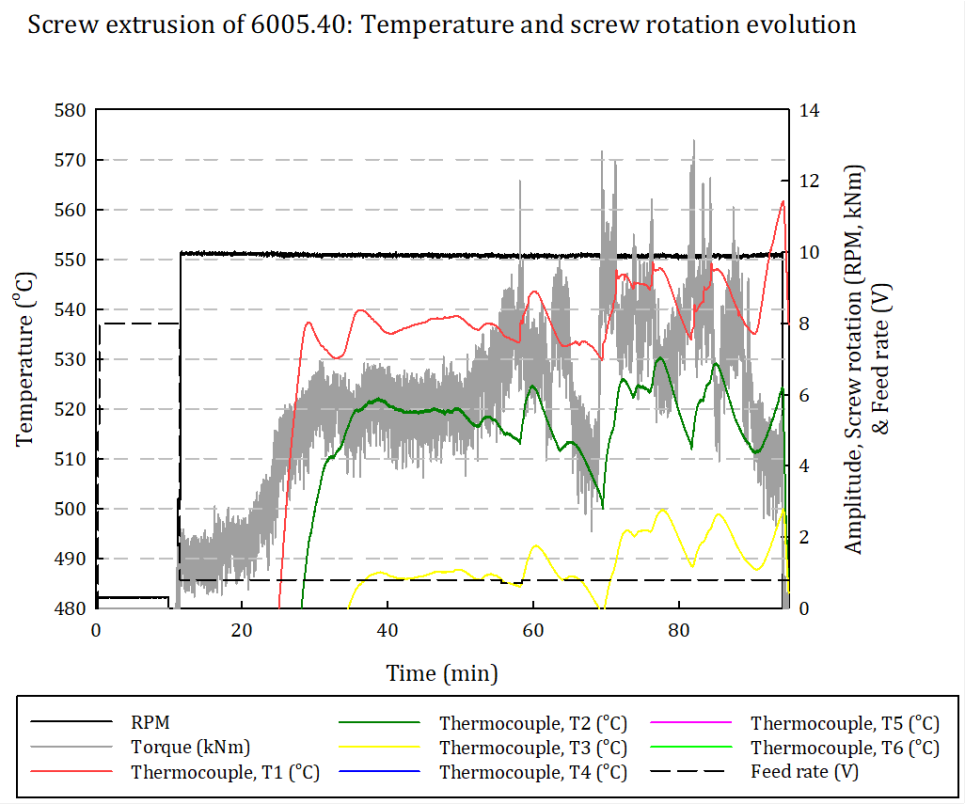

(b)

Figure B.2: Temperature and screw momentum evolution during the extrusion process of 6005.40. (b) focus on thermocouple T1.

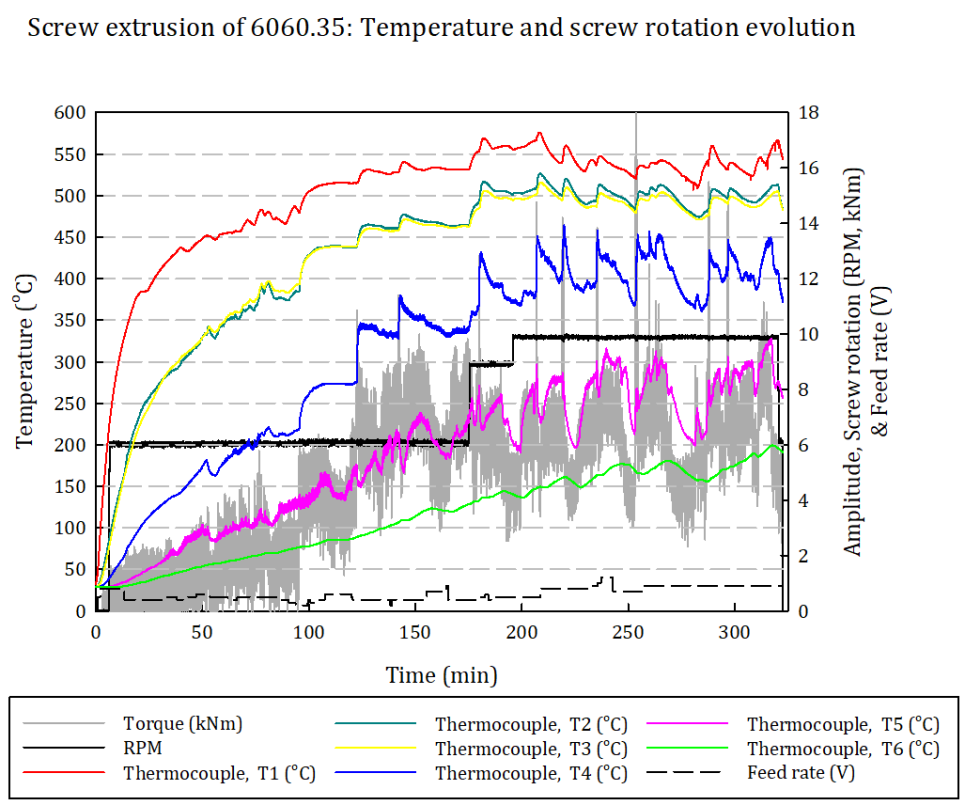

(a)

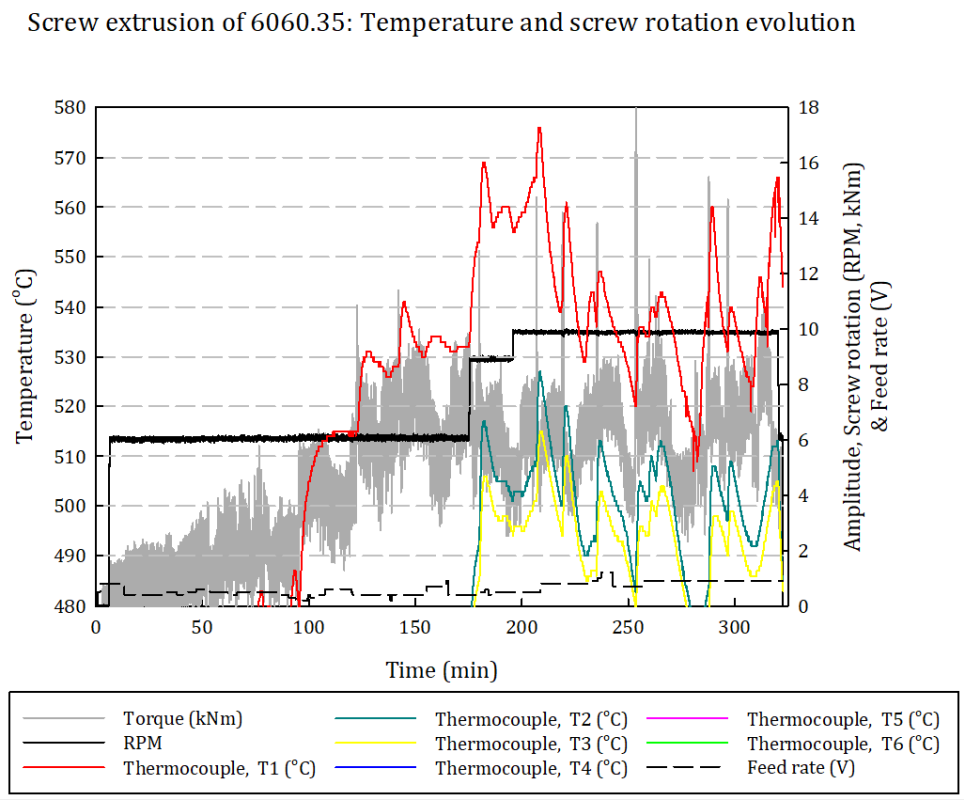

(b)

Figure B.3: Temperature and screw momentum evolution during the extrusion process of 6060.35. (b) focus on thermocouple T1.

Appendix C

Ram extrusion log

The ram extrusion log is presented with parameters from the extrusion of each alloy. Column 2, "Forsøk Nr", in the first sheet shows the experiment number, where no. 13, 14 and 15 represent alloys 6082, 6005.40 and 6060.35, respectively. In the following three sheets these alloys show the applied load through the length of the extrusion billet.

Prosjektnummer / navn :
Container / matrise / bolster: Ø100mm / 10mm stang D5 / vinge
Kommentarer:

Dato: 2020-02-14

Log	Forsøk Nr	Material e	Målte parametre												Kommentarer
			$v_{STEMPEL}$ (mm/s)		ut av T_{BOLT} (°C)			T_{CONT}	T_{STEM}	$T_{BÆREFLATE}$		Kraft (kN)		
			innstilt	ok	ovn	foran	Bak			$T1_{MAX}$	$T2_{MAX}$	Max	Min	
	1	6000	6	6.1	550	502	498	431	~50	-	-	4035	3053	
	2	~	~	6.0	550	503	495	431	~100			3996	2940	
	3	~	~	6.1	551	502	496	431	~180			3996	2897	
	4	5000	3	2.9	415	449	442	431	96	-	-	5708	3663	
	5	~	"	2.9	"	448	441	431	96			5672	3669	
	6	"	"	2.9	"	446	440	431	98			5821	3789	
	7	4000-2	3	2.9	440	466	462	431	124			3682	2780	
	8	"	"	2.9	"	470	463	431	184			3701	2696	
	9	"	2.8	2.7	"	468	461	431	192			3692	2658	
	10	4000-1	1.5	1.4	499	457	451	431	186			4582	3260	Overheat 500
	11	~	1.0	0,9	497	452	447	431	112			4621	3169	
	12	~	1.0	0,9	487	442	433	432	176			4829	3234	Ventet 2-4min for å redusere temp
	13	6000	6	6.1	482	500	496	431	128			3886	2836	
	14	6005-40	6	6.1	"	500	497	431	176			3543	2546	
	15	6060.35	6	6.1	"	497	490	431	136			3171	2479	

Luftsirk 60Hz til ~450
Ind. agg. 482°C

1→3: Ind. aggr. 525°C
Luftsirk ovn 500

4000-1 Overheat 500 med til 450 60Hz
4000-2 Overheat 500, med til ~450, 60 Hz, luftsirk. ovn 482

SINTEF

Date: 14.02.2002 22:49:19

Exp nr: 15 Ekstrud av 10 mm stang

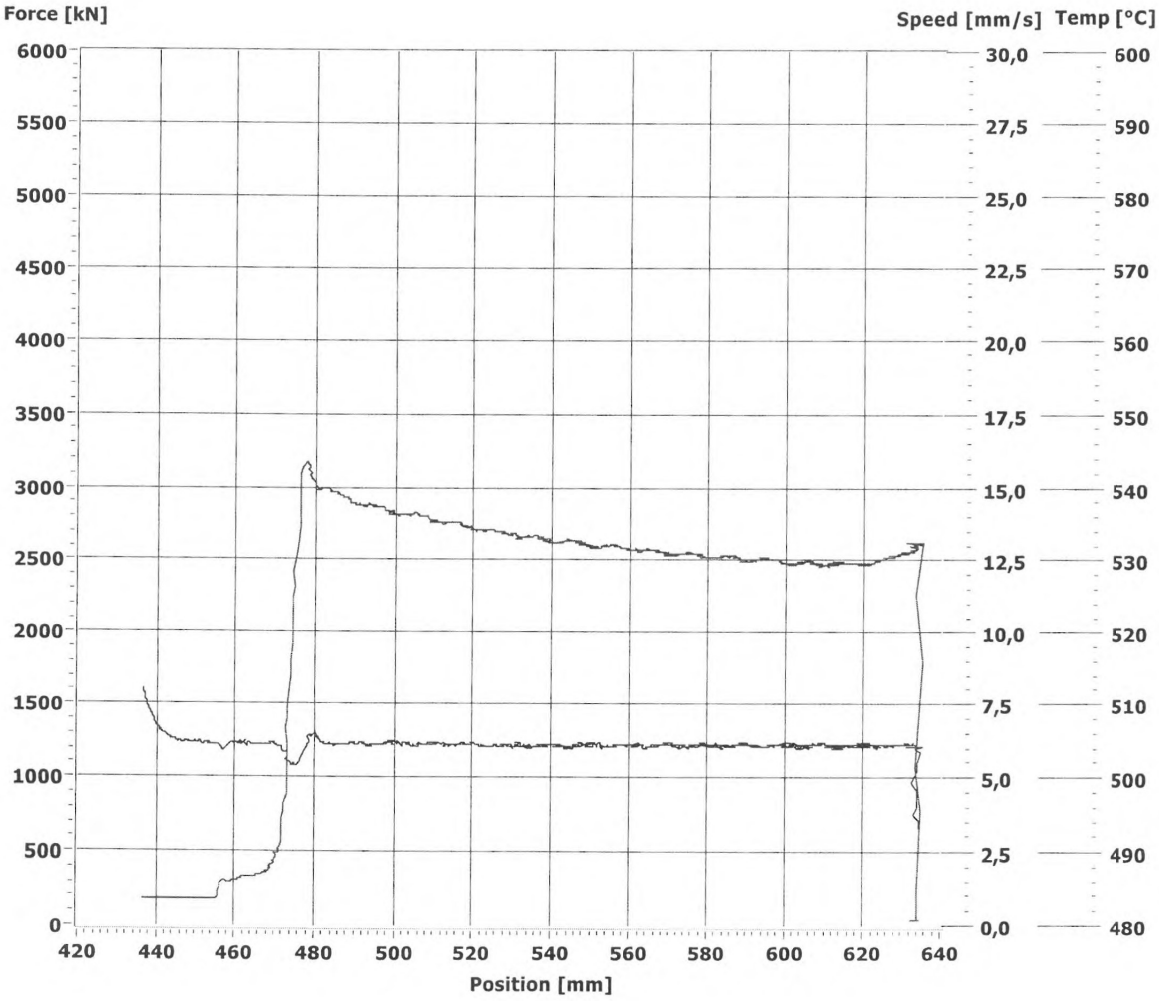

Position [mm]
Force [kN]
Speed [mm/s]
Temp Die [°C]
Temp Container [°C]
Temp 1 [°C]
Temp 2 [°C]
Temp 3 [°C]
Temp 4 [°C]
Temp 5 [°C]
Temp 6 [°C]
Voltage 1 [V]
Voltage 2 [V]
Voltage 3 [V]
Kraft smiverktøy [kN]

Matrix: A11, Ø9mm stang med 2 vinger

Max Force = 3171
Min Force = 2479
Avr Speed = 6,1
Max Temp Die = 472
Max Temp Cont = 432
Max Temp 1 = -90000

SINTEF

Date: 14.02.2002 22:38:24

Exp nr: 14 Ekstrud av 10 mm stang

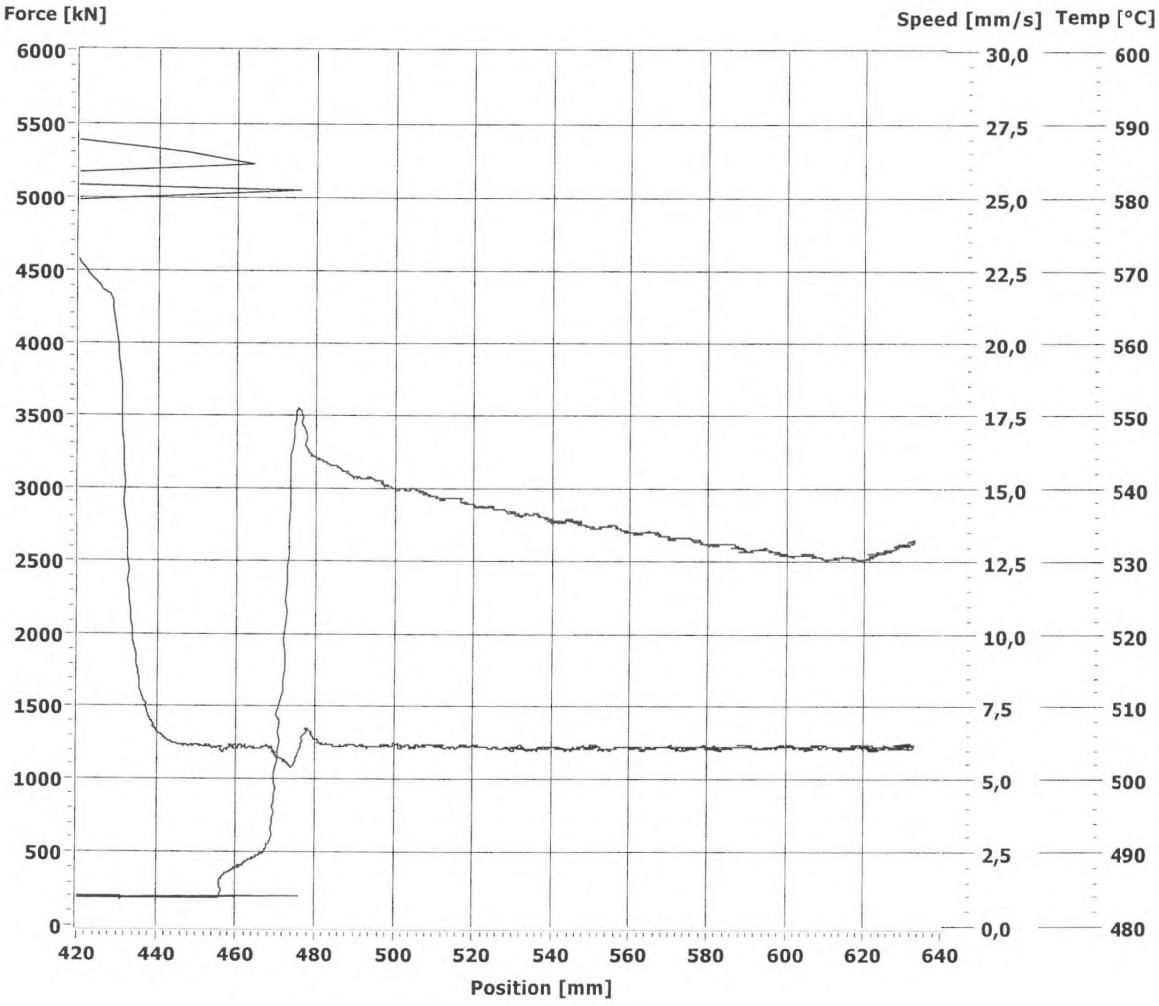

Position [mm]
Force [kN]
Speed [mm/s]
Temp Die [°C]
Temp Container [°C]
Temp 1 [°C]
Temp 2 [°C]
Temp 3 [°C]
Temp 4 [°C]
Temp 5 [°C]
Temp 6 [°C]
Voltage 1 [V]
Voltage 2 [V]
Voltage 3 [V]
Kraft smiverktøy [kN]

Matrix: A11, Ø9mm stang med 2 vinger

Max Force = 3543
Min Force = 2546
Avr Speed = 6,1
Max Temp Die = 470
Max Temp Cont = 432
Max Temp 1 = -90000

SINTEF

Date: 14.02.2002 22:28:48

Exp nr: 13 Ekstrud av 10 mm stang

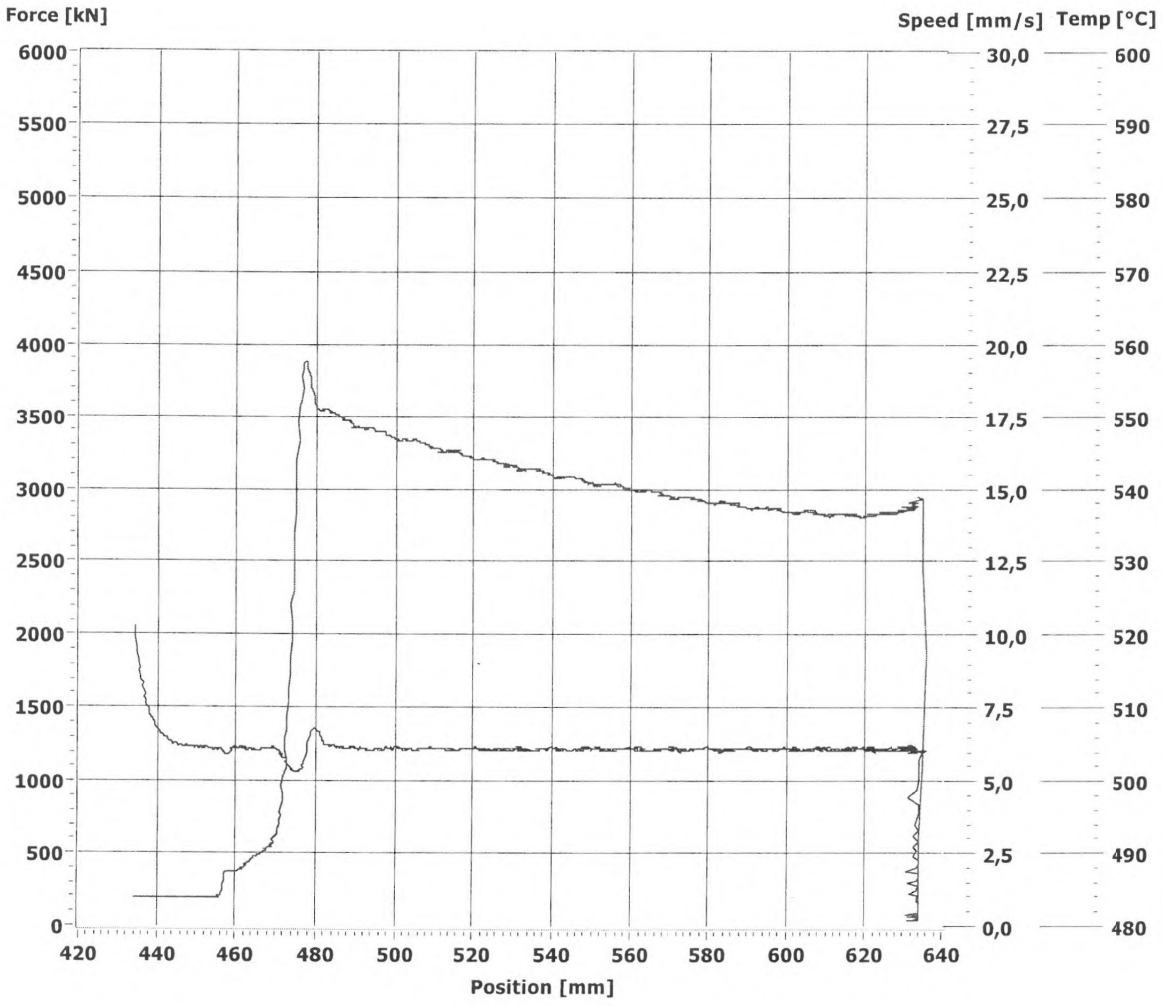

Position [mm]
Force [kN]
Speed [mm/s]
Temp Die [°C]
Temp Container [°C]
Temp 1 [°C]
Temp 2 [°C]
Temp 3 [°C]
Temp 4 [°C]
Temp 5 [°C]
Temp 6 [°C]
Voltage 1 [V]
Voltage 2 [V]
Voltage 3 [V]
Kraft smiverktøy [kN]

Matrix: A11, Ø9mm stang med 2 vinger

Max Force = 3880
Min Force = 2836
Avr Speed = 6,1
Max Temp Die = 470
Max Temp Cont = 432
Max Temp 1 = -90000

Appendix D

Additional microstructures by OM

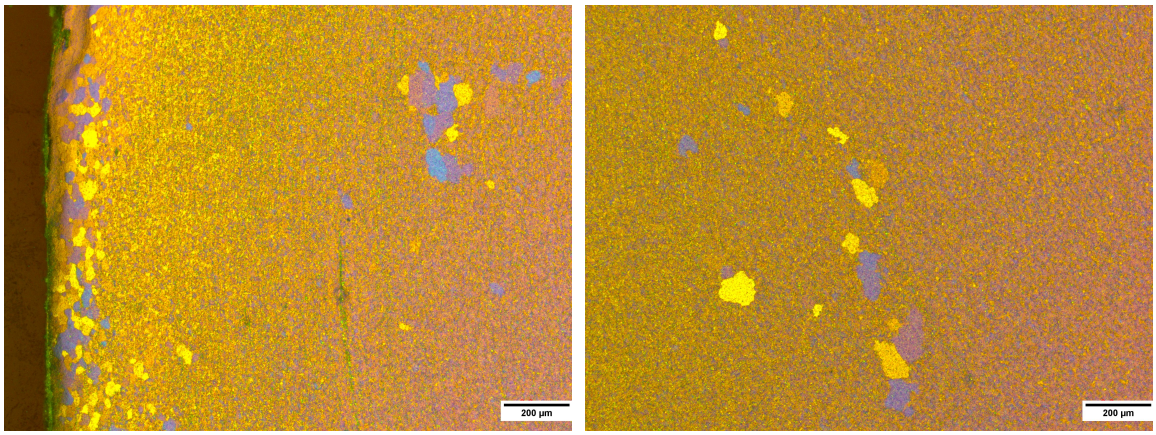

(a) (b)

Figure D.1: Microstructure of SHT SE6082AC showing sporadic recrystallization in the cross section.

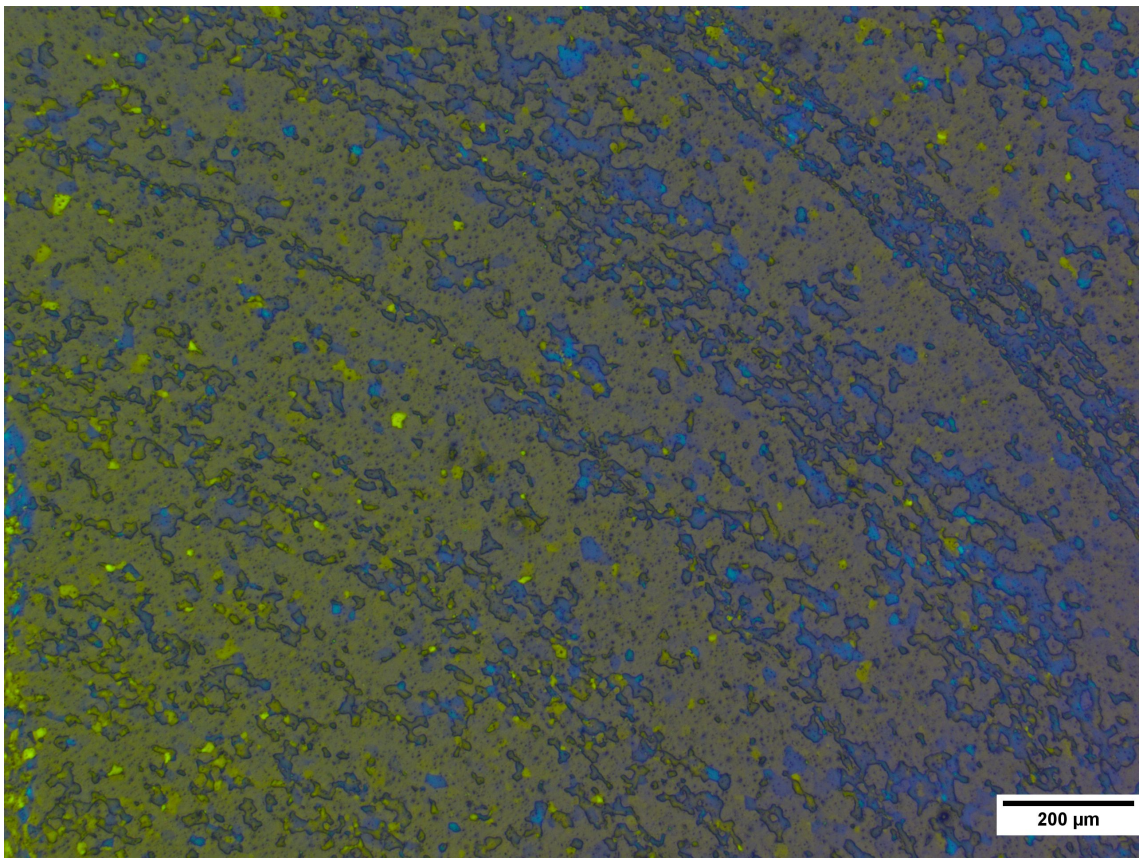

Figure D.2: Microstructure of SHT SE6060.35WQ showing flow pattern in the cross section.

Appendix E

Effective Si content

$$EffectiveSi = Si - \frac{Fe + Mn + Cr}{3} \tag{E.1}$$

The equation above bases its element content on the values obtained in the chemical analysis in Appendix A. The effective Si content is represented for each alloy in Table E.1.

Table E.1: Effective Si content for each alloy.

Alloy	Si	Fe	Mn	Cr	Eff. Si
6082	1.00	0.22	0.57	0.0055	0.74
6005.40	0.60	0.20	0.19	0.0015	0.47
6060.35	0.42	0.20	0.026	0.0033	0.34

Kjetil Houmb Kristiansen

Characterization of Extruded Aluminium Alloys from Ram Extrusion and Screw Extrusion

NTNU
Norwegian University of
Science and Technology